

ENGINEERING POROUS SILICON PHOTONIC STRUCTURES
TOWARDS FAST AND RELIABLE OPTICAL BIOSENSING

By

Yiliang Zhao

Dissertation

Submitted to the Faculty of the
Graduate School of Vanderbilt University
in partial fulfillment of the requirements
for the degree of

DOCTOR OF PHILOSOPHY

in

Interdisciplinary Materials Science

May, 2017

Nashville, Tennessee

Approved:

Sharon M. Weiss, Ph.D.

Paul E. Laibinis, Ph.D.

Yaqiong Xu, Ph.D.

Deyu Li, Ph.D.

Dmitry S. Koktysh, Ph.D.

To my beloved family,

Copyright © 2017 by Yiliang Zhao
All Rights Reserved

ACKNOWLEDGMENTS

First and foremost, I express my gratitude to Prof. Sharon Weiss, for her excellent guidance and mentoring. I am deeply thankful to her for letting me join her research group and instilling confidence in me. Since February 2011 when Dr. Weiss interviewed me via Skype for graduate school admission, her guidance, patience, and encouragement have helped me to overcome all the challenges encountered during my Ph.D. study. Struggles when writing my first journal paper and anxiety before giving my first conference presentation were soothed by her supportive training. Her scientific insights and expertise always helped me find the right directions when exploring highly interdisciplinary research areas. The theoretical knowledge, technical skills, and critical thinking I learned from Dr. Weiss will benefit me in every future research endeavor.

I would like to acknowledge my Ph.D. committee, whose advice and critiques have been extremely helpful in discovering brilliant ideas. I am especially grateful to Prof. Paul Laibinis who provided significant guidance to all of my research work. Without his expertise, talents, and insights, this research would not be possible. I would like to thank Prof. Dmitry Koktysh for his kindly help and valuable advice on quantum dots. I am thankful to Prof. Raymond Mernaugh for his suggestions on immunoassays and collaborations in protein sensing experiments.

I am truly honored to have been a part of the Weiss group. I thank all the past and present members of the Weiss group for maintaining an innovative research atmosphere in FGH 331 and a dynamic work environment in FGH 323. Thanks to Dr. Jenifer Lawrie, Dr. Yang Jiao, and Dr. Xing Wei for introducing me to porous silicon research and teaching me the numerous tools and techniques fundamental for my work. Thanks to Dr. Shuren Hu, Kun Qin, Dr. Girija Gaur, Dr. Kelsey Beavers, and Tengfei Cao for great work in our collaborations. Thanks to Dr. Gilbert

Rodriguez, Dr. Jeremy Mares, Dr. Shweta Bhandara, Kevin Miller, Joshua Fain, Francis Afzal, and Vijayashree Parsi Sreenivas (VJ) for all the help and useful technical discussions. Thanks to Yasmin Graham and all the undergraduate researchers who contributed to this research.

My collaborators at the Oak Ridge National Laboratory (ORNL), Dr. Scott Retterer, Dayrl Briggs, and Kevin Lester have provided extremely useful guidance, facility training, and fabrication expertise that enabled the successful demonstrations of the devices used in this thesis. I thank all the staff at the Vanderbilt Institute for Nanoscale Science and Engineering (VINSE) and Vanderbilt Institute for Integrative Biosystems Research and Education (VIIBRE) for teaching me the instruments and techniques related to fabrication and analysis. The research presented in this thesis was funded in part by the Army Research Office (W911NF-09-1-0101 and W911NF-15-1-0176).

Finally, I acknowledge Kun Qin for being my science buddy, my sports mentor, and my cheerleader. I cannot express my gratitude enough for the endless love and support from my family. Their trust and encouragement have allowed me to overleap obstacles when chasing my dreams.

TABLE OF CONTENTS

	Page
DEDICATION	ii
ACKNOWLEDGMENTS	iv
LIST OF FIGURES	ix
LIST OF TABLES	xvi
Chapter	
1. INTRODUCTION	1
1.1 Optical Biosensors	1
1.2 Porous Silicon (PSi)	6
1.2.1 Formation and Fabrication	6
1.2.2 Refractive Index of PSi	7
1.2.3 PSi in Label-Free Optical Biosensing	8
1.3 PSi Photonic Structures	10
1.3.1 Single Layer Interferometer	10
1.3.2 Waveguide	12
1.3.3 Microcavity	15
1.4 Current Challenges in PSi Biosensing	16
1.4.1 Surface Passivation	16
1.4.2 Mass Transport Efficiency	20
1.5 Overview of the Dissertation	23
2. DNA INDUCED CORROSION IN POROUS SILICON BIOSENSORS.....	25
2.1 Introduction.....	25
2.2 Fabrication of PSi Waveguides.....	26
2.3 Surface Functionalization.....	27
2.3.1 In Situ DNA Synthesis	27
2.3.2 In Situ PNA Synthesis.....	28
2.3.3 Nucleic Acid Sensing.....	29
2.4 Prism Coupling Measurements	29

2.5	Characterization of PSi Passivation	30
2.6	Influence of Probe DNA on PSi Corrosion.....	32
2.7	Influence of DNA Hybridization on PSi Corrosion.....	35
2.8	Mitigating DNA Induced Corrosion in PSi.....	40
2.8.1	DNA Hybridization with Synthesized PNA Probes.....	40
2.8.2	Compensating DNA Charge with Magnesium.....	44
2.9	Mechanism of Corrosion on Passivated PSi	46
2.10	Summary	52
3.	COMPUTATIONAL ANALYSIS OF CLOSED-ENDED AND OPEN-ENDED POROUS SENSORS	53
3.1	Introduction.....	53
3.2	Analytical Calculation of Analyte Transport Efficiency	54
3.3	Numerical Model and Simulation	59
3.4	Simulated Transport and Reaction Kinetics.....	64
3.4.1	Velocity Distribution and Analyte Concentration Distribution	64
3.4.2	Influence of Flow Velocity	68
3.4.3	Influence of Analyte Concentration	71
3.4.4	Influence of Analyte Diffusivity and Adsorption Rate	72
3.5	Summary	75
4.	FLOW-THROUGH POROUS SILICON MEMBRANES FOR LABEL-FREE BIOSENSING.....	76
4.1	Introduction.....	76
4.2	Device Fabrication and Measurement.....	78
4.2.1	Electrochemical Etching of PSi Microcavities.....	78
4.2.2	Photolithography Process for PSi Membrane Fabrication	79
4.2.3	Microfluidics Integration.....	81
4.2.4	Optical Reflectivity Measurement	83
4.3	Effect of Analyte Size on Sensor Response.....	84
4.4	Surface Sensing.....	88
4.5	Quantum Dot Based Fluorescence Measurement	92
4.6	Pressure Test	95
4.7	Summary	98

5. CONCLUSIONS.....	100
5.1 Summary	100
5.2 Future Research Opportunities.....	102
5.2.1 P <i>Si</i> Microarrays for Multiplexed Biosensing.....	102
5.2.2 Quantum Dot Coupled P <i>Si</i> for Colorimetric Sensing	105
REFERENCES	107

LIST OF FIGURES

- Figure 1.1.** Experimental set-up for an SPR biosensor. Prism coupling configuration is used for exciting a surface plasmon wave at the surface of the sensor chip. When light couples into the surface plasmon wave, the SPR angle is observed as a sharp drop in the reflectivity of incident light. The SPR angle shifts (from I to II in the lower left plot) when molecules bind to the surface. Binding affinities and kinetics can be determined by monitoring the change of resonance signal versus time (lower right plot). Reprinted with permission from Ref. [7]. Copyright 2002 Nature Publishing Group. 3
- Figure 1.2.** Schematic of a two-electrode etch cell used to make PSi. The main oxidation and reduction half-reactions that occur during PSi formation are shown. Note the lower case h^+ represents a valence band hole and the upper case H^+ is a proton in these equations. Reprinted with permission from Ref. [57]. Copyright 2012 Wiley-VCH. 7
- Figure 1.3.** (a) Top view and (b) cross-sectional SEM images of a PSi single-layer film. The brighter regions indicate silicon and the darker regions indicate air. (c) The Fabry-Perot fringes in the reflectance spectrum of PSi interferometer before (grey line) and after (black line) infiltration of molecules into the pores. (d) The EOT, obtained via FFT analysis of the reflectance spectrum, shows an increase upon molecule infiltration. 12
- Figure 1.4.** (a) Cross-sectional SEM image of a double-layer PSi waveguide. (b) Reflectance spectra of a PSi waveguide. The resonance angle shifts in response to the change of the effective refractive index of the PSi waveguide layer. (c-e) Common coupling configurations for PSi waveguide: (c) prism coupling in the Otto configuration, (d) prism coupling in the Kretschmann configuration, and (e) grating coupling. 14
- Figure 1.5.** (a) Cross-sectional SEM image of a PSi microcavity. The brighter layers indicate low porosity films and the darker layers indicate high porosity films. (b) Reflectance spectra of a microcavity with a resonance dip due to light being trapped in the defect of the microcavity. The resonance wavelength red-shifts after species are added to the PSi matrix. 16
- Figure 1.6.** Top: oxidation and corrosion process of freshly etched PSi illustrating surface regions of the porous structure. Bottom: modification of PSi by oxidation and silanization provides surface passivation. Left: the grey region indicates the porous matrix; the black represent oxide layers, the red represents network of silane molecules. 18

Figure 1.7. Schematic illustrations of (a) flow-over and (b) flow-through PSi sensors. Improved infiltration and mass transport can be achieved using open-ended pores in the flow-through configuration. 22

Figure 2.1. (a) Stabilization of silanized PSi waveguides. Reflectance spectra are given for a PSi waveguide after oxidation (black, solid line), TEOS-HBA silanization (red, solid line), and soaking in DI water for 2, 4, 6, or 8 hours (blue, green, gray, orange dashed lines, respectively). Hydrolysis is indicated by shifts of the resonance to lower angles after soaking in DI water. (b) Resonance angle shift as a function of time during DI water soak. Reprinted with permission from Ref. [122]. Copyright 2014 American Chemical Society. 31

Figure 2.2. Optical characterization of *in situ* DNA probe synthesis and subsequent degradation of an activated PSi waveguide biosensor in DI water. (a) Probe DNA was synthesized from a stabilized PSi waveguide functionalized with TEOS-HBA silane (black, solid line). Reflectance spectra following *in situ* synthesis of 16-mer DNA probe and deprotection of charge-masking groups from the sugar-phosphate backbone are indicated by red and blue solid lines, respectively. Incubation of the deprotected probe DNA molecules with negatively charged backbones in DI water results in a blueshift to lower resonant angles (dashed lines). (b) Resonance angle shift as a function of time during DI water soak after probe DNA deprotection. (c) Reflectance spectra of a PSi waveguide stably functionalized with TEOS-HBA silane (black solid line), after *in situ* synthesis of probe DNA molecules that have not been deprotected (red solid line), and after soaking the waveguide in DI water (dashed lines). Reprinted with permission from Ref. [122]. Copyright 2014 American Chemical Society. 33

Figure 2.3. Resonance angle blueshift upon hybridization of a 100% complementary DNA target (10 μ M) with DNA probes synthesized on a PSi waveguide. Reprinted with permission from Ref. [122]. Copyright 2014 American Chemical Society. 36

Figure 2.4. Fluorescence spectra of porous silicon waveguides functionalized with probe DNA complementary (red solid line) and not complementary (black dotted line) to 6-FAM labeled DNA target that was exposed to both waveguides. A distinct fluorescence signature indicating DNA hybridization is only present for the complimentary probe-target system. 37

Figure 2.5. No waveguide resonance shift is observed upon exposure of an *in situ* probe DNA functionalized PSi waveguide to a 100% mismatch DNA sequence. 38

Figure 2.6. Resonance angle shift of PSi waveguide as a function of incubation time with 100% complementary DNA sequence. Reprinted with permission from Ref. [122]. Copyright 2014 American Chemical Society. 39

Figure 2.7. Dependence of PSi biosensor corrosion on target DNA concentration. Waveguide resonance blueshift upon one hour incubation with 100% complementary DNA sequence at different concentrations. The line is shown as a guide to the eye. Reprinted with permission from Ref. [122]. Copyright 2014 American Chemical Society. 40

Figure 2.8. Response of PSi waveguide functionalized with 3-APTES silane (black, solid line) and *in situ* synthesized probe PNA (as-synthesized: red, solid line; deprotected: blue, solid line) upon exposure to DI water. Following a slight initial blueshift (dashed lines) no additional shift is observed, suggesting that neutrally-charged PNA probes do not cause PSi corrosion. 41

Figure 2.9. Functionalization of PSi waveguide surface with neutrally-charged PNA probes mitigates waveguide corrosion during hybridization with DNA targets. Resonance shifts are shown for a PNA probe-functionalized PSi waveguide upon incubation with (a) 100% complementary DNA sequence and (b) 100% mismatch DNA sequence. Reprinted with permission from Ref. [122]. Copyright 2014 American Chemical Society. 42

Figure 2.10. Resonance shift for a PNA probe-functionalized PSi waveguide upon incubation with 100% complementary PNA oligo target. 44

Figure 2.11. Addition of Mg^{2+} ions mitigates PSi waveguide corrosion during hybridization of DNA targets to PNA probes. Resonance shifts are shown upon incubation with (a) 100% complementary DNA and (b) 100% mismatch DNA in the presence of 2 M $MgCl_2$. Reprinted with permission from Ref. [122]. Copyright 2014 American Chemical Society. 45

Figure 2.12. Resonance redshift of PSi waveguide functionalized with *in situ* synthesized PNA probes upon one hour hybridization with 100% complementary DNA at various concentrations in the presence of 2 M $MgCl_2$. The line is shown as a guide to the eye. 46

Figure 2.13. FTIR spectra of PSi waveguide freshly etched, oxidized at 800 °C for 30 min, functionalized with TEOS-HBA silane, and with deprotected 16-mer DNA probes. Reprinted with permission from Ref. [122]. Copyright 2014 American Chemical Society. 49

Figure 2.14. Schematic of the DNA induced corrosion process in PSi illustrating surface regions of the waveguide structure. The green region indicates the thermal oxide on pore walls; the yellow represents silane molecules; DNA oligos are represented by the red (probe) and black (target) helix structures attached on the silane molecules. The chemical reactions present a possible mechanism for corrosion of a silicon atom initiated by sequential nucleophilic attacks by water molecules and resulting in the release and dissolution of the atom in the form of

Si(OH)₄. Reprinted with permission from Ref. [122]. Copyright 2014 American Chemical Society..... 50

Figure 3.1. Schematic illustration of the models for (a) flow-over and (b) flow-through porous sensing systems. Binding sites are represented by blue probes in the porous regions, and target analyte molecules in the contacting solution are represented by orange spheres. Reprinted with permission from Ref. [149]. Copyright 2016 American Chemical Society. 55

Figure 3.2. Simulated equilibrium time of the flow-over porous sensor consisted of 50 pores, 200 pores, 500 pores, 1000 pores, and 1200 pores. The dotted line is shown as a guide to the eye. 63

Figure 3.3. Schematic of the flow cell-integrated PSi sensor used in COMSOL simulations. (a) Schematic of a closed-ended PSi membrane in a flow-over operation mode. The flow cell dimensions are $L = 100 \mu\text{m}$ and $H = 60 \mu\text{m}$. The start of the porous region is located $50 \mu\text{m}$ away from the inlet. (b) Schematic of an open-ended PSi membrane in a flow-through operation mode. The flow cell dimensions used for the upper and bottom channels are $L = H = 60 \mu\text{m}$. The start of the porous region is located $40 \mu\text{m}$ away from the inlet. Eq 3.16 applies to the blue highlighted PSi area as the boundary condition. (c) Zoom-in of the PSi area showing equally spaced pores with pore diameter = 25 nm and period = 30 nm . The computational space comprises 500 pores along a distance $w = 15 \mu\text{m}$ and a height $h = 4 \mu\text{m}$ 63

Figure 3.4. (a) Velocity distribution and analyte concentration distribution at 180 s into the simulation for the flow-over scheme. In the velocity distribution plot, the color bar indicates the flow rate of the solution. Zoom-in image shows the flow rate around the pores. In the concentration distribution plot, the color bar indicates the concentration gradients of analytes in solution. Zoom-in image shows that most analytes do not reach the PSi sensing area due to the formation of the depletion zone. (b) Velocity and concentration distributions at 180 s into the simulation for the flow-through scheme. Zoom-in image of the velocity distribution shows rapid flow through the pores. Zoom-in image of the concentration distribution confirms that the analyte is transported into the PSi sensing region. Reprinted with permission from Ref. [149]. Copyright 2016 American Chemical Society. 65

Figure 3.5. Analyte concentration distributions in the porous region at different times for (a) the flow-over and (b) the flow-through scheme. The illustrated pores represent those from the center of the simulated porous region..... 67

Figure 3.6. Simulated average surface concentration of analytes that were captured by flow-over and flow-through porous sensors as a function of time. Reprinted with permission from Ref. [149]. Copyright 2016 American Chemical Society..... 68

Figure 3.7. Equilibrium time of both flow schemes as a function of the flow velocity. Analyte concentration = 1 μM . Reprinted with permission from Ref. [150]. Copyright 2016 Springer... 69

Figure 3.8. Total volume of analyte solution required in closed-ended, flow-over porous sensors and open-ended, flow-through porous sensors to reach equilibrium at different flow velocities. Analyte concentration = 1 μM . Reprinted with permission from Ref. [150]. Copyright 2016 Springer..... 70

Figure 3.9. Effect of analyte concentration on equilibrium time. Flow velocity = 5 $\mu\text{L}/\text{min}$. The equilibrium times of flow-over sensors with closed-ended pores and flow-through sensors with open-ended pores show an inverse dependence on analyte concentration. Reprinted with permission from Ref. [150]. Copyright 2016 Springer..... 72

Figure 3.10. Equilibrium time of both flow schemes for analytes with different diffusivities D and adsorption rate constants k_a . Flow velocity= 5 $\mu\text{L}/\text{min}$, and analyte concentration = 1 μM . Reprinted with permission from Ref. [150]. Copyright 2016 Springer..... 73

Figure 4.1. Process flow for PSi membrane fabrication. 79

Figure 4.2. Images of a fabricated PSi membrane. (a) Optical microscope image and schematic illustration of PSi membrane surrounded by silicon nitride. (b) Cross-sectional SEM image of the edge of the membrane region showing the sacrificial layers, PSi layers comprising the microcavity, and the remaining silicon nitride film. (c) Top view SEM image of the PSi membrane region. (d) Magnified cross-sectional SEM image of the microcavity region showing the high quality of the interfaces. Reprinted with permission from Ref. [149]. Copyright 2016 American Chemical Society. 81

Figure 4.3. (a) Top-view and (b) side-view of the PSi membrane sensors integrated with PDMS flow cells..... 83

Figure 4.4. Reflectance spectra of the PSi microcavity measured after electrochemical etching (black line), oxidation (red line), removal of silicon substrate (green line), and flow cell attachment (blue line). All measurements were taken in air. The resonance wavelength after each step is identified with an arrow..... 84

Figure 4.5. Comparison of real-time PSi microcavity response for closed-ended pores in the flow-over scheme and open-ended pores in the flow-through scheme. Time-dependent PSi microcavity resonance wavelength shifts upon exposure to (a) 3-APTES, (b) HRP, and (c) CAT. Solid symbols are experimental data obtained from an open-ended, flow-through PSi microcavity membrane; hollow symbols are experimental data from a closed-ended flow-over PSi microcavity. Dotted lines provide guides to the eye. Reprinted with permission from Ref. [150]. Copyright 2016 Springer..... 86

Figure 4.6. Reflectance spectra of the flow-through PSi membrane measured after oxidation, 3-APTES functionalization, biotin attachment, and streptavidin binding. All spectra were recorded in a flow cell environment after equilibrium was reached. The resonance wavelength after each step is identified with an arrow. Reprinted with permission from Ref. [149]. Copyright 2016 American Chemical Society. 89

Figure 4.7. Comparison of real-time sensor response to 5 μM STV solution with different flow schemes. Measured PSi microcavity resonance wavelength shifts were plotted as a function of exposure time. Reprinted with permission from Ref. [149]. Copyright 2016 American Chemical Society..... 90

Figure 4.8. PSi microcavity wavelength shift measured after (a) 20 min and (b) 2 h exposures to 500 nM, 1 μM , and 5 μM STV solutions under different flow schemes. Reprinted with permission from Ref. [149]. Copyright 2016 American Chemical Society. 92

Figure 4.9. Photoluminescence spectra measured under 488 nm laser excitation from QDs adsorbed within flow-through and flow-over PSi microcavities and a control PSi microcavity sample with no QD functionalization. The inset shows camera images of the samples under UV excitation at 365 nm: 1) QDs in an open-ended PSi membrane in the flow-through scheme and 2) QDs in a closed-ended PSi film in the flow-over scheme. Both the PL spectra and camera images were obtained in air from PSi microcavities after their removal from the flow cells. Reprinted with permission from Ref. [149]. Copyright 2016 American Chemical Society. 93

Figure 4.10. Absorbance and photoluminescence spectra for $\text{AgInS}_2/\text{ZnS}$ quantum dots in a 30 μM aqueous solution..... 94

Figure 4.11. Camera image and schematic illustration of the experimental setup for pressure test. Adapted with permission from Ref. [214]. Copyright 2015 Macmillan Publishers Limited. 96

Figure 4.12. Vertical deflection of the PSi membrane at various applied pressures. Height profile was obtained from interferometric profilometry. The dashed line is shown as a guide to the eye.

Microscope images of the 1 mm × 1 mm PSi membrane under different pressure are shown in bottom panels. At 0 psi of applied pressure, the membrane showed initial bulging due to build-in stress. The membrane maintained its structural integrity at 10 psi. Breakage occurred at 11 psi. 97

Figure 5.1. (a) Camera image of the PSi microcavity microarray. The diameter of each array element is 300 μm and the distance between each element is 700 μm. (b) Reflectance spectra of a PSi microcavity element in the array. 104

Figure 5.2. Schematic illustration of colorimetric sensing in QD coupled PSi microcavity. QDs are infiltrated into PSi microcavity to achieve cavity modified QD emission. Any changes to the environmental refractive index of the sensor upon target molecule capture will perturb the cavity resonance conditions, causing a shift in the cavity coupled QD emission spectra. This shift in the QD emission profile can be detected as color change using a camera. 106

LIST OF TABLES

Table 1.1. Comparison of characteristic parameters for different types of biosensors.....	5
--	---

CHAPTER 1

INTRODUCTION

1.1 Optical Biosensors

Biosensors are analytical devices that incorporate a biological receptor and a transducer. The biological receptor, most commonly an enzyme, an antibody, or an oligonucleotide sequence, is used to create a recognition event in the presence of a target analyte. This bio-recognition event is then converted into a measurable signal by a transducer. Both the presence and the concentration of a target analyte can be obtained from the signal provided by a biosensor. The biosensor industry has witnessed a significant growth over the past decade. Due to an increasing demand for biosensing technology in point-of-care diagnostics, environmental monitoring, the food industry, and security applications, the total biosensor market, valued at \$11.39 billion in 2013, is expected to reach \$22.68 billion in 2020 [1,2]. A number of different technologies, such as electrochemical, piezoelectric, mechanical and optical based transduction systems, have been developed to construct biosensors. Among these different categories, optical biosensors have been the most widely reported, given their high detection sensitivity, ease of use, compatibility with multiplexed assays, and the variety of transduction techniques available. Optical transducers may detect molecular binding events as changes in luminescence, light absorbance, polarization, refractive index, Raman scattering, and surface plasmon resonance (SPR) [3,4]. The most commonly used optical biosensing method, known as labeled sensing, requires a specialized label on the analyte to report its binding to a receptor. The major advantage of labeled sensors is their high sensitivity. For example, the detection limit (the lowest concentration at which target detection is possible) of enzyme-linked immunosorbent assays (ELISA) is ~ 0.1 pM [5]. However, the long required analysis time (> 1 hour) is a major drawback of labeled sensing

methods. The whole process including sample pretreatment could take up to several days. Additionally, the complex and time-consuming labelling procedures limit the cost-effectiveness and the potential for widespread use of labeled sensors. Ideally, a biosensor should operate label-free, be sensitive, and provide fast read-out.

Efforts to develop such biosensing platforms have mainly focused on SPR and refractive index techniques. These techniques allow users to study the interaction between immobilized receptors and target analytes in solution, in real time without labeling of the analyte. One of the most successful commercially available label-free optical biosensors is produced by Biacore (GE Healthcare) [6]. This instrument utilizes an array of SPR sensors to detect target analytes such as low molecular weight drugs, antibodies, peptides, and oligonucleotides [7-9], for which a typical experimental set-up is shown in Figure 1.1. The interaction of light with surface charges in a metal (typically gold or silver) creates surface plasmon waves that propagate along the interface between metal and dielectric materials (air, biological or chemical species) [10]. The most commonly used configuration to excite surface plasmon waves is prism coupling, in which the incident light is totally reflected at the metal/prism boundary, creating an evanescent wave that penetrates the thin metal layer [11]. When the wavevector component of incident light parallel to the metal surface matches that of the surface plasmon wave, light is coupled into the surface plasmon wave [12]. This condition only happens at certain angles of incidence, appearing as a drop in the reflectivity of incident light. The electromagnetic field of a surface plasmon wave decays evanescently into both the metal and dielectric medium, but the majority of the evanescent field is in the dielectric medium due to increased damping in the metal. As a result, SPR is very sensitive to changes in the dielectric medium. Binding of molecules to surface-immobilized receptors will change the refractive index of the dielectric medium and lead to a

shift of the SPR angle. A detection limit of 0.01 ~ 3 nM has been reported for label-free SPR sensors [13,14]. Although this number is more than two orders of magnitude higher than that for ELISA, SPR provides much faster analysis time (~ 10 s) and has the capability to perform real-time, kinetic, and thermodynamic analysis [15,16].

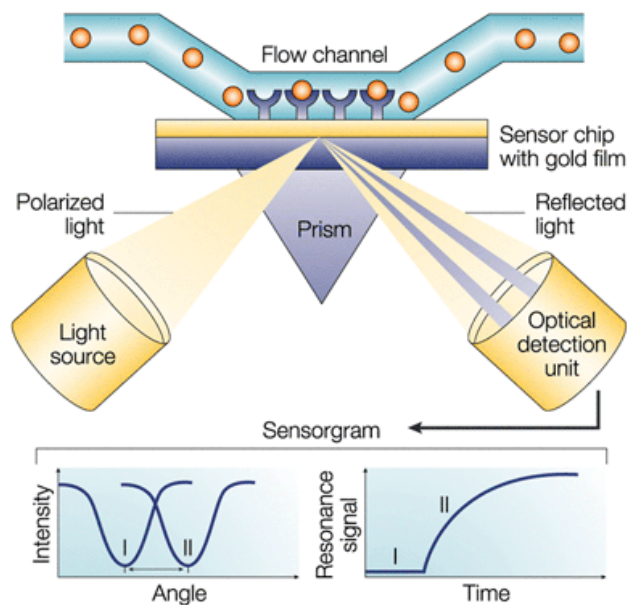


Figure 1.1. Experimental set-up for an SPR biosensor. Prism coupling configuration is used for exciting a surface plasmon wave at the surface of the sensor chip. When light couples into the surface plasmon wave, the SPR angle is observed as a sharp drop in the reflectivity of incident light. The SPR angle shifts (from I to II in the lower left plot) when molecules bind to the surface. Binding affinities and kinetics can be determined by monitoring the change of resonance signal versus time (lower right plot). Reprinted with permission from Ref. [7]. Copyright 2002 Nature Publishing Group.

In spite of product and technology innovations, current label-free biosensors face significant challenges for small molecule detection and detection in complex media [17-19]. Most optical

structures in biosensor applications possess a strong electromagnetic field within a solid material and an evanescent field at the sensor surface. As a result, molecules captured on the sensor surface only interact with a small fraction of the evanescent field, which limits the sensitivity and detection limit of a biosensor. Additionally, contaminant molecules bound on the sensor surface may cause false positives in the readout. Porous materials are promising candidates as substrates for the next generation of optical biosensors due to their large internal surface area for molecular binding and light-matter interaction as well as their tunable pore size distributions that enable size-selective filtering of contaminant molecules [20-22]. A variety of porous materials including porous silicon [23-25], porous alumina [26-28], porous titania [29,30], and various polymers [31,32] have been studied for the development of optical biosensors. Among those materials, porous silicon has been considered as a particularly favorable material for constructing low-cost label-free optical biosensors due to the easy manipulation of its pore sizes, optical properties, and surface chemistries [33-35]. Label-free porous silicon biochips (SKi Sensors) used for real-time monitoring of biomolecular interactions have been commercialized by Silicon Kinetics [36]. Table 1.1 summarizes the response times and detection limits of various existing and emerging biosensing technologies.

Table 1.1. Comparison of characteristic parameters for different types of biosensors.

Transduction Techniques	Description	Analyte	Response Time †	Detection Limit	Ref.
Optical labeled detection					
Immunofluorescent assay	ELISA*	antibodies, antigens, hormones	60 min	0.1 pM in serum	[5]
Lateral flow immuno-chromatographic assay	Pregnancy test*	hCG	3 min	10 µM in urine	[37]
Colorimetric bio-barcode amplification assay	Protein amplification by functionalized nanoparticles	proteins	1 - 3 hr	0.5 - 50 fM in serum	[38-40]
Optical label-free detection					
Surface plasmon resonance	Biacore SPR system*	small organic compounds	10 s	10 pM in buffer	[6]
Porous silicon biosensor	SKi Sensor by Silicon kinetics*	small organic compounds	10 min/cycle	100 pg/ml in buffer	[36]
	Single layer, Rugate filter, microcavity	DNA, proteins	5 - 45 min	1 pM - 1 µM in buffer	[20,33]
Silicon photonics biosensor	Genalyte microring resonator*	antibodies, antigens	10 - 30 min	45 ng/ml in blood	[41]
	Photonic crystal, waveguide, microring, interferometer	DNA, proteins	2 - 10 min	3 pM - 10 nM in buffer	[42-45]
Mechanical detection					
Surface stress sensors	Microcantilever	disease biomarkers	10 min	300 pM in buffer	[46]
	PZT cantilever	antigen	10 min	0.3 pM in buffer	[47]
Mass sensing	Microcantilever	antigen	4 hr	1.5 fM in serum	[48]
	Quartz crystal microbalance	DNA	3.5 hr	1 fM in buffer	[49]
Electrical detection					
Field-effect transistor	Silicon nanowire	DNA, antigen	10 - 20 min	5 - 10 pM in buffer	[50,51]
	Silicon nanoribbon	disease biomarkers	10 min	0.6 pM in blood	[52]
Electrochemical detection					
Voltammetry/Amperometry	Glucose test*	glucose	5 s	1 mM in blood	[53]
	Enzyme-based electrode	herbicides	20 - 40 s	5 - 500 nM in buffer	[54]
Impedance	Gold nanoparticle modified electrode	antibody	5 - 10 s	2 µg/ml in buffer	[55]
	Carbon nanotube array electrode	antibody	5 - 10 s	200 ng/ml in buffer	[56]

* Commercialized biosensors.

† Response time for a sensor is governed by the minimum detectable signal change and is usually significantly shorter than the saturation time.

1.2 Porous Silicon (PSi)

1.2.1 Formation and Fabrication

Porous silicon, a nanostructured material consisting of pores that are most typically electrochemically etched into a silicon substrate [57], has attracted considerable interest for potential application in fields ranging from biochemistry [58-61] to photonics [62-64], and solid state electronics [65-68]. The most common way to form PSi is anodization, which is initiated by anodically biasing a silicon wafer in a fluoride-based electrolyte solution, although stain etching and metal-assisted chemical etching can also be used [69-72]. In this work, PSi films are anodized in a two-electrode cell as shown in Figure 1.2. The working electrode is an anode and is usually a doped silicon wafer. The cathode is typically platinum, and it is immersed in an electrolyte solution containing hydrofluoric acid (HF). The electric field moves positively charged holes in the silicon valence band towards the surface, creating polarized surface Si-H bonds that are susceptible to nucleophilic attack by fluoride ions. The resulting highly polarized and reactive Si-F bonds are prone to continuous attack by fluoride ions, leading to dissolution of the silicon atom in the form of SiF_6^{2-} . The process repeats when another valence hole reaches the surface. Valence holes tend to aggregate near the pore tips due to the high radius of curvature in that region which generates a locally enhanced electric field. As a result, the etching preferentially proceeds at the pore tips, allowing the fabrication of sharp interfaces between PSi layers of different porosities by simply adjusting the etching current. The (100) crystallographic face contains strained Si-H bonds that are less stable than Si-H bonds in other faces; hence, pores primarily propagate in the $\langle 100 \rangle$ direction [73-75]. The electrochemical reaction occurring at the platinum cathode is primarily the reduction of protons to hydrogen gas. The accumulation of

hydrogen gas bubbles at the surface of the wafer and in the porous region can lead to lateral variation in layer thickness and porosity. For the formation of PSi multilayer structures, improved interface uniformity has been achieved by incorporating a short period of zero bias between individual layers, thereby allowing the hydrogen to diffuse out of the pores, and the fluoride to be replenished at the pore tips [76].

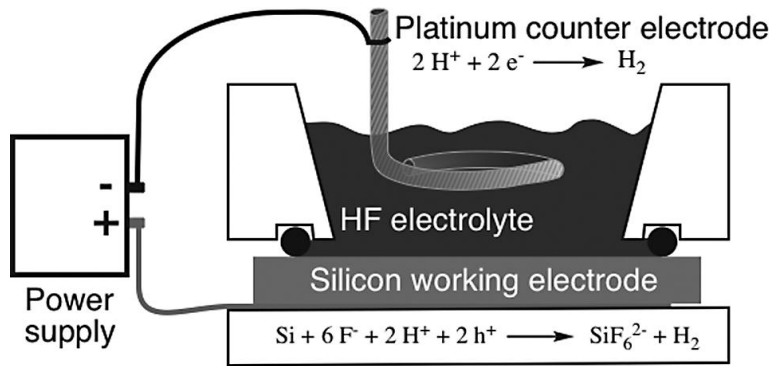


Figure 1.2. Schematic of a two-electrode etch cell used to make PSi. The main oxidation and reduction half-reactions that occur during PSi formation are shown. Note the lower case h^+ represents a valence band hole and the upper case H^+ is a proton in these equations. Reprinted with permission from Ref. [57]. Copyright 2012 Wiley-VCH.

1.2.2 Refractive Index of PSi

When its pore diameter is much smaller than the wavelength of light, PSi can be treated as an effective medium whose refractive index is a weighted average of the refractive indices of separate components in the composite matrix [77,78]. Effective medium theory describes the effective refractive index of PSi (n_{eff}) as a function of the complex refractive index of silicon (n_{Si}) and that of the pore-filling material ($n_{fill} = 1$, for air). The porosity P and the topology of

the porous structure will also affect n_{eff} . One of the most frequently used effective medium models is the Bruggeman approximation [79], which is given by

$$P \frac{n_{fill}^2 - n_{eff}^2}{n_{fill}^2 + 2 n_{eff}^2} + (1 - P) \frac{n_{Si}^2 - n_{eff}^2}{n_{Si}^2 + 2 n_{eff}^2} = 0$$

A porosity range of 30 to 90% gives an approximate refractive index range of 3.30 to 1.15, depending on the wavelength of light and morphology of the PSi. As PSi porosity is dependent on the current density used in anodization, PSi layers with different refractive indices can be etched into a silicon substrate in the vertical direction by appropriately varying the applied current densities and anodization times, enabling the fabrication of versatile photonic architectures with PSi films.

1.2.3 PSi in Label-Free Optical Biosensing

There are many advantages in using PSi for biosensing applications, including its ease of fabrication, large internal surface area ($>100 \text{ m}^2/\text{cm}^3$) available for molecule capture, compatibility with many functionalization chemistries, and capability for size-selective infiltration of target species [33,35,80,81]. Since its first use as a biosensor almost two decades ago, PSi has emerged as a promising nanomaterial for label-free optical biosensing applications as its optical properties, such as photoluminescence (PL) or reflectance, are highly sensitive to the presence of chemical and biological species inside the pores [20,60,82,83].

Some of the earliest sensing work using PSi took advantage of the PL properties of the material. Room-temperature PL of PSi was first discovered in the early 1990's [82]. While PL tags are commonly used for labeled sensing, label-free sensing has been realized in PSi by observing changes in the PL of PSi as affected by the analyte [84-87]. For example,

immunocomplex formation between an antibody and antigen within a PSi matrix has been observed to quench the material's PL [84]. Binding of target DNA to a complementary DNA probe immobilized in the porous matrix has been confirmed through PL spectra shifts since DNA hybridization increases the effective refractive index of PSi, inducing a redshift in the PL spectra [85]. However, in recent years, PL-based transduction methods are less studied in comparison to sensors relying on reflectance-based transduction methods. This preference is related to the comparative greater error associated with measuring PL intensity changes [88].

PSi biosensors relying on reflectance-based transduction methods utilize photonic structures whose reflectance spectra shift upon molecular binding in the porous matrix. By appropriately varying etching conditions, photonic structures such as interferometers [61,89], Bragg mirrors [90,91], rugate filters [92,93], microcavities [94,95], and waveguides [96,97] have been demonstrated with PSi layers and used as biosensors. The large surface area of PSi, arising from the presence of nanoscale pores, facilitates enhanced light-matter interaction (i.e., light-molecule interaction) in PSi photonic structures, especially for those structures that support guided modes in the PSi film. It is well known that enhanced light-matter interaction leads to improved sensitivity to biomolecule binding events [98]. For nonporous materials, the majority of the active sensing region that spatially overlaps with guided modes is inaccessible to molecules as it resides inside a solid material; molecules can only interact with an evanescent field at the sensor surface [99]. In the case of PSi, molecules infiltrate the porous matrix and directly interact with a guided mode. The effective index of the guided mode is greatly perturbed by the addition of molecules, changing the refractive index of the PSi according to the effective medium approximation as discussed in Section 1.2.2. The following sections describe several types of PSi

photonic structures including interferometer, waveguide, and microcavity, along with their applications in optical biosensing.

1.3 PSi Photonic Structures

1.3.1 Single Layer Interferometer

The simplest structure for reflectance-based sensors consists of a single-layer PSi film with a few microns thickness (Figure 1.3b). Under normal incidence white light illumination, reflectance interference fringes are observed (Figure 1.3c). The Fabry-Perot relationship for thin film interference states that the reflectance fringe maxima are described by the relationship given by eq 1.1,

$$m\lambda = 2nL \quad (1.1)$$

where λ is the wavelength of incident light, n is the refractive index of the thin film, L is the film thickness, and m is an integer. Taking a Fourier transform (FFT) of the reflectance data as a function of wave number produces a peak corresponding to the term $2nL$, which is the effective optical thickness (EOT) of the PSi layer (Figure 1.3d). Upon infiltration of molecules into the pores, the effective refractive index of the PSi film changes, causing a change of EOT and a spectral shift of the Fabry-Perot fringes. By monitoring the magnitude of spectral fringe shift or EOT change, the amount of infiltrated molecules can be quantitatively determined in a label-free way.

Due to its ease of fabrication and straightforward measurement, single-layer interferometer has been used for the detection of a variety of target analytes, such as DNA, proteins, and bacteria [60,100-102]. For the detection of large molecules that are excluded from the pores, Segal *et al.* have demonstrated real-time observation of bacteria attachment by monitoring

intensity changes in the reflectance spectrum of PSi interferometer [102-104]. They reported detection of *E. coli* bacteria at relatively low concentration ranges of $10^3 - 10^5$ cells/mL within a few minutes of analysis time, which may be applied for identification and quantification of food pathogens. However, for the detection of low concentrations of small molecules captured inside the pores, the EOT changes of interferometer are barely noticeable, leading to low sensitivity in direct binding assays. One possible method to enhance the optical signal generated by specific attachment of a small analyte is by labeling the analyte with quantum dots (QDs) [105]. Gaur *et al.* have shown that QDs may serve both as high refractive index signal amplifiers for reflectance measurements and as fluorescent labels for the verification of molecule capture in the functionalized pores [105]. A greater than 5-fold enhancement in the measured reflectance fringe shift and a nearly 3 order of magnitude improvement in the detection limit for only 6% surface area coverage of QDs inside the porous matrix were demonstrated for detecting target QD-biotin conjugates with streptavidin probes immobilized in PSi single-layer films.

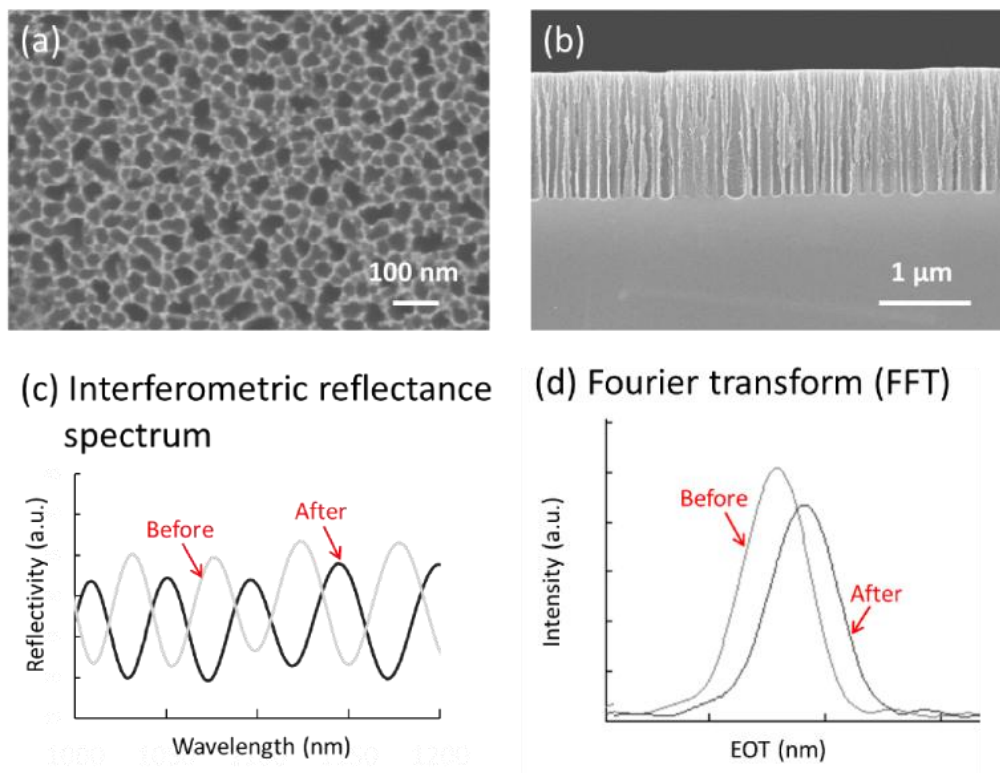


Figure 1.3. (a) Top view and (b) cross-sectional SEM images of a PSi single-layer film. The brighter regions indicate silicon and the darker regions indicate air. (c) The Fabry-Perot fringes in the reflectance spectrum of PSi interferometer before (grey line) and after (black line) infiltration of molecules into the pores. (d) The EOT, obtained via FFT analysis of the reflectance spectrum, shows an increase upon molecule infiltration.

1.3.2 Waveguide

While single layer PSi interferometers do enable a greater interaction between light and molecules compared to a nonporous thin film or interferometer, due to the larger number of molecules captured in the pores, resonant PSi optical structures further benefit from increased intensity of light within a guided mode layer, which also increases the detection sensitivity of

optical structures [106]. Wei *et al.* have demonstrated a resonant PSi slab waveguide capable of achieving high sensitivity for label-free detection of small molecules [107,108]. Figure 1.4a shows the SEM image of a PSi waveguide consisting of two layers: a top, low porosity, high refractive index layer known as the waveguide layer and a bottom, high porosity, lower refractive index layer referred to as the cladding layer. In this structure, light is trapped in the high index waveguide layer due to total internal reflection at the interfaces with the lower index cladding layer below and air above. While light is only guided in the waveguide layer, an exponentially decaying field exists in the regions directly above and below the waveguide layer. This evanescent field allows light to be efficiently coupled into and out of the waveguide under specific conditions (e.g., angle of incidence, wavelength of light). A dip in the attenuated reflectance spectra of PSi waveguides corresponds to a coupled mode and the angle at which the dip appears directly corresponds to the effective index of the PSi waveguide (Figure 1.4b) [109]. A redshift of the resonance dip suggests that molecules have been added inside the pores of the PSi waveguide, increasing the effective refractive index, while a resonance blueshift suggests that material has been removed from the waveguide, which decreases the effective refractive index of the waveguide. Unlike SPR sensors in which an evanescent, exponentially decaying wave interacts with bound molecules, in PSi waveguides, guided waves propagate through the material overlapping with the molecular binding region. Previous work has demonstrated the PSi waveguides have the potential to outperform traditional SPR sensors by a factor of 60 [110].

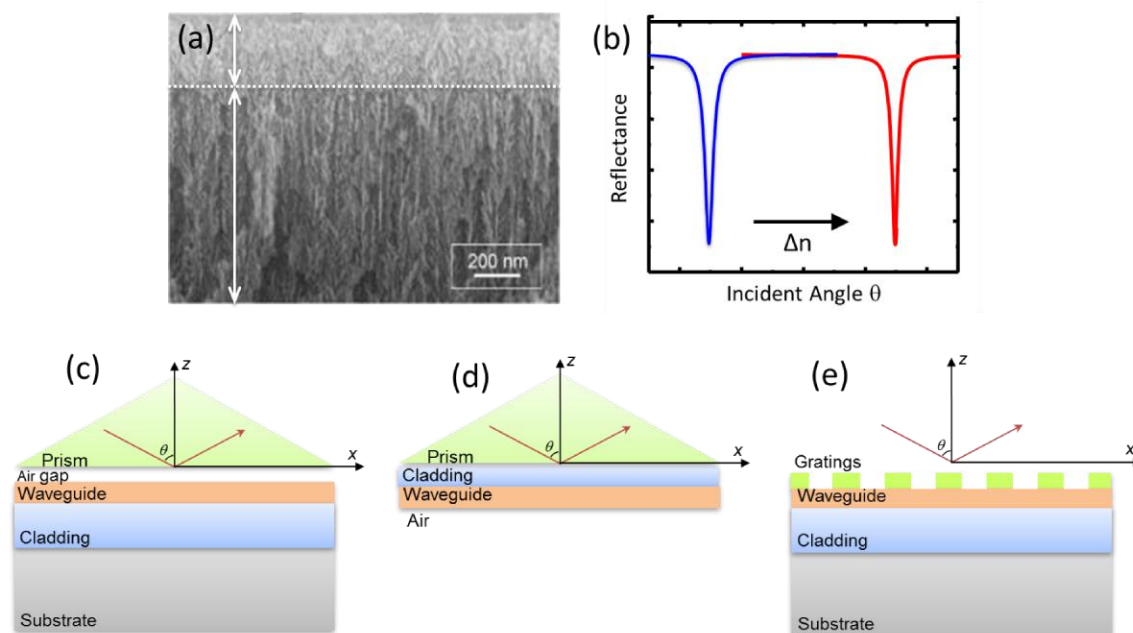


Figure 1.4. (a) Cross-sectional SEM image of a double-layer PSi waveguide. (b) Reflectance spectra of a PSi waveguide. The resonance angle shifts in response to the change of the effective refractive index of the PSi waveguide layer. (c-e) Common coupling configurations for PSi waveguide: (c) prism coupling in the Otto configuration, (d) prism coupling in the Kretschmann configuration, and (e) grating coupling.

A major advantage to use the waveguide structure as sensing platforms is that the most sensitive sensing region is the top waveguide layer that is most easily accessible for molecule infiltration. However, for light to couple into a waveguide, incident light needs to be phase matched to the propagating mode within the waveguide. Figure 1.4c, d show schematic illustrations of PSi waveguide structures based on the Otto configuration and the Kretschmann configuration, respectively, which are two commonly used methods for prism coupling. The Otto configuration is used for double-layer PSi waveguides with an air gap between the waveguide

and the prism. The Kretschmann configuration is used for single-layer PSi waveguides with a low index layer (e.g., polymer or metal) deposited directly on the prism to act as a cladding layer. Figure 1.4e shows another commonly used coupling method, grating coupling, where the phase mismatch is overcome by a periodic grating if the wave vector of higher order diffracted light matches the wave vector of a guided mode. Previous work has demonstrated the use of PSi waveguides for the detection of DNA and proteins, with the lowest expected detection limit in the nanomolar range [97,111,112].

1.3.3 Microcavity

A one-dimensional multilayer microcavity is comprised of alternating layers of low and high refractive index possessing optical thicknesses corresponding to one-fourth of the resonant wavelength (i.e., Bragg mirrors) and a central defect layer with an optical thickness that is typically equivalent to half the resonant wavelength of the microcavity. Light is localized in the central defect layer, making it the most sensitive region of the microcavity for detecting target analyte as a result of strong light-matter interaction. A high quality PSi microcavity requires several periods of alternating high and low porosity films as shown in Figure 1.5a, with the exact number of periods dependent on the refractive index contrast within the Bragg mirror layers. The reflectance spectrum of a microcavity is characterized by a resonance dip in the middle of a high reflectance band (Figure 1.5b). The resonance wavelength of a PSi microcavity is strongly dependent on the effective refractive index of the PSi defect layer and also depends on the effective refractive index of the surrounding PSi mirror layers. In order for the PSi microcavity to be effective in biosensing applications, the pore size must be sufficiently large to allow infiltration of target analytes through the Bragg mirror into the defect layer. When molecules are

captured on the pore walls, the effective refractive index of PSi increases and the microcavity resonance red-shifts to longer wavelengths. Both microcavities and waveguides have the potential to achieve the lowest detection limits [113], with microcavities being simpler to implement as the reflectance spectrum of a microcavity is measured by a spectrometer with near normal incident light while each waveguide requires complex instrumentation for angle dependent coupling.

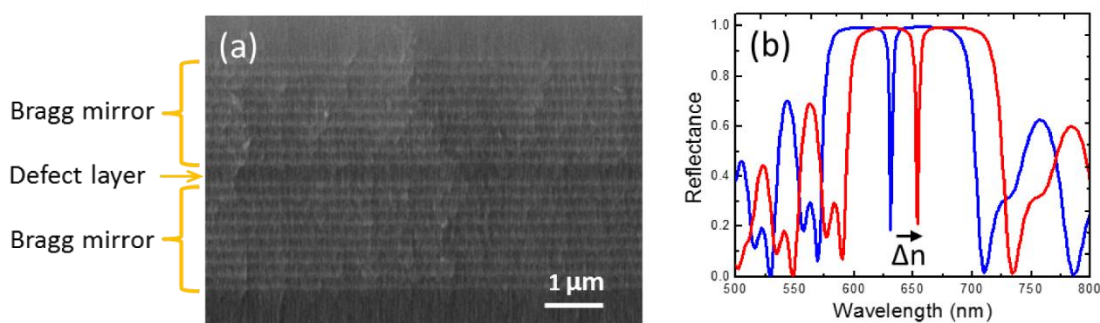


Figure 1.5. (a) Cross-sectional SEM image of a PSi microcavity. The brighter layers indicate low porosity films and the darker layers indicate high porosity films. (b) Reflectance spectra of a microcavity with a resonance dip due to light being trapped in the defect of the microcavity. The resonance wavelength red-shifts after species are added to the PSi matrix.

1.4 Current Challenges in PSi Biosensing

1.4.1 Surface Passivation

Freshly etched PSi surfaces are hydride-terminated and oxidize readily upon exposure to aqueous solutions [100]. Si-H and Si-Si bonds in PSi are both competent reducing agents, and are able to reduce water to hydrogen. Oxidation of Si-Si bonds by water generates new surface Si-H bonds, which leads to continued oxidation and corrosion of PSi, as shown in Figure 1.6. In biosensing applications, the degradation and dissolution of PSi over time in aqueous solutions is

detrimental to the sensitivity, accuracy, and lifetime of the sensor. Indeed, P*Si* has been exploited as a delivery vehicle for pharmaceuticals precisely because of its biocompatibility, low toxicity, and ability to dissolve over time in a physiological environment [114]. Adsorption of DNA oligonucleotides has been shown to accelerate P*Si* oxidation and dissolution [115]. It was postulated that the negative charges on DNA's phosphate backbone attract the positively charged carriers in *p-type* silicon to the P*Si* surface, facilitating the nucleophilic attack by water molecules that ultimately leads to P*Si* dissolution. DNA hybridization amplifies P*Si* corrosion and dissolution, which limits sensing reproducibility and leads to device failure. In order to improve the sensing performance of practical P*Si* biosensors, especially for DNA sensing applications, the sensor surfaces require protection from degradation.

A common method of P*Si* surface passivation is to grow an oxide layer to slow down further oxidation. Several oxidation methods have been used to treat P*Si*, including thermal oxidation, oxidation via aqueous hydrogen peroxide treatment, and ozone oxidation [115-117]. Among those methods, thermal oxidation at 700 °C or above tends to form much more stable oxides of P*Si* [118]. Ozone oxidation forms a hydrophilic, hydrated oxide that readily dissolves in an aqueous environment [100]. Peroxide-based chemical oxidation is challenged by concurrent hydrogen bubble formation which may induce non-uniformity of the oxide [119]. In addition, thermal oxide generated at temperatures above 300 °C is predominated by Si-O-Si bonding with few Si-OH species [116]. Si-O-Si species are less polar than Si-OH species and show greater resistance to attack by water molecules, leading to slower rates of degradation in solution. Subsequent silanization of the oxidized P*Si* surface forms a densely packed silane layer that limits the access of water to the underlying surface and protects the surface from degradation, as shown in Figure 1.6. The reactive groups at the silanes provide attachment points

for biorecognition molecules. However, the silane chemistry is not ideal. Silane molecules tend to couple to themselves, forming multilayers that can clog the pores and block access for additional reagents or target analytes [120,121]. PSi sensors well-passivated via thermal oxidation and silanization have shown improved aqueous stability in the presence of DNA molecules [122]. In this thesis, a saturation in the corrosion effect was observed on thermally oxidized and silanized PSi, contrary to prior reports of continuous dissolution. The corrosion process was further mitigated by decreasing the overall concentration of negative charges within the PSi sensing volume, leading to improved reusability and reliability of the PSi DNA sensor.

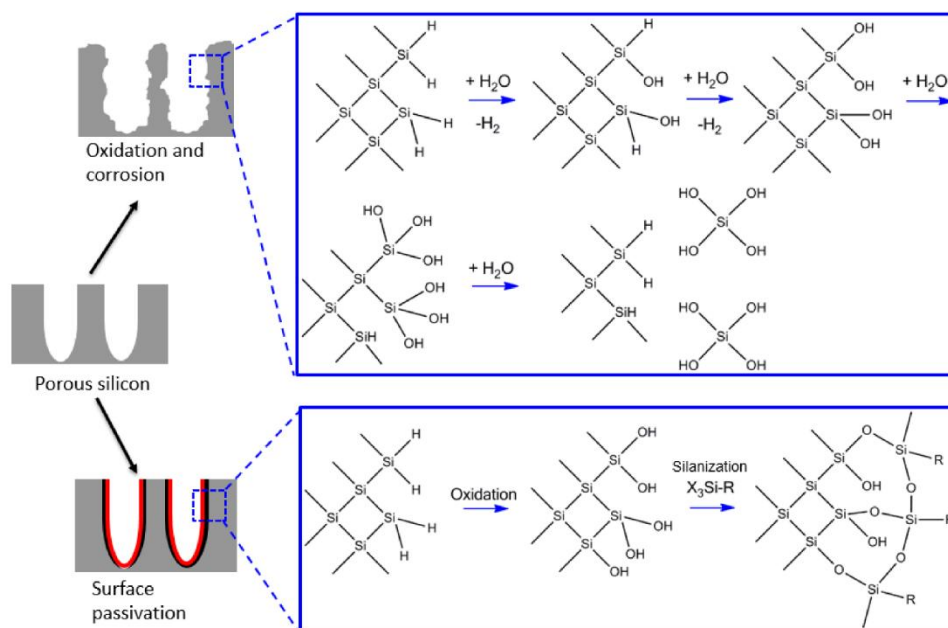


Figure 1.6. Top: oxidation and corrosion process of freshly etched PSi illustrating surface regions of the porous structure. Bottom: modification of PSi by oxidation and silanization provides surface passivation. Left: the grey region indicates the porous matrix; the black represent oxide layers, the red represents network of silane molecules.

Alternatively, PSi can be passivated by forming Si-C surface bonds. Si-C bonded species show greater kinetic stability than Si-O bonded species and could potentially withstand years of exposure to aqueous solutions without degradation [123]. The most common reaction used to form Si-C bonds is hydrosilylation of alkenes or alkynes at the hydride terminated PSi surface [124-126]. The hydrosilylation reaction typically converts just a few percent of Si-H species on PSi. Because most functional organic molecules are too large to fit into the smaller pore opening in PSi, the maximum conversion efficiency reported for hydrosilylation was less than 30% [126,127]. The fact that reactive Si-H species still exist in PSi makes the modified sample still susceptible to aqueous dissolution [128]. Another method to form Si-C bonds is thermal carbonization. This reaction involves decomposition and partial pyrolysis of acetylene gas on a PSi sample held at elevated temperatures [129,130]. The temperature of the pyrolysis reaction plays a key role in determining the carbon content. When the reaction is carried out at temperatures above 500 °C, significant carbonization occurs, removing most residual hydrogen and leading to black PSi films with high carbon content [131,132]. Due to the difficulty of balancing the trade-offs between carbon content and optical transparency, passivating PSi optical biosensors via thermal carbonization can be more challenging than oxidation. Replacing the acetylene precursor with an organic polymer (polyfurfuryl alcohol) has been reported to improve the optical transparency of carbonized PSi films [133]. The pyrolyzed PSi-carbon composite is chemically stable and optically smooth, leading to strong interest in label-free biosensing applications [132-134].

1.4.2 Mass Transport Efficiency

For applications ranging from biosensing to drug delivery, molecules of interest have to be transported into or out of inner pore spaces within PSi. Lawrie *et al.* demonstrated that infiltrating PSi waveguides with biomolecules can be challenging, even when the pore diameters of the waveguide are up to five times larger than the size of biomolecules [112]. The high aspect ratio of the nanopores may cause significant barrier to mass transport within PSi. The biosensing performance of a PSi microcavity is especially inhibited by infiltration challenges, as the most sensitive sensing region of a microcavity, known as the defect layer, is buried underneath the Bragg mirror layers. Target molecules have to pass the low porosity layers in the Bragg mirror to reach the buried defect layer. The average pore sizes of the low porosity layers etched from highly doped p-type silicon range from 5 to 20 nm, which are on the same order as the sizes of typical target molecules such as antibodies, enzymes and short nucleic acids. A common strategy to overcome the infiltration challenge is pore widening. For example, partial dissolution of freshly etched PSi in alkaline solution widens the internal pore space and facilitates mass transport through PSi multilayers [135,136]. However, the extent of pore widening is limited by the existing pore morphology and the requirement of sufficient index contrast between PSi multilayers. Extensive pore widening can lower the porosity difference in PSi multilayers and compromise the optical quality of PSi photonics structures, which will negatively impact the sensitivity of biosensors [113,137].

In recently years, the incorporation of PSi biosensors into lab-on-chip devices has shown great promise for sensitive and reliable molecule detection in real time [138,139]. Microfluidic systems are integrated with PSi for the transport of bulk analyte to the porous sensing region. Most of the PSi sensing approaches that incorporate microfluidics rely on closed-ended porous

films in a flow-over operation mode, in which the analyte solution is transported over the external surface of the nanoporous film [140-142] (Figure 1.7a). Due to the infiltration challenge in PSi, the flux into an individual pore can be as slow as a few molecules per pore per second [143-145]. As a result, most molecules are swept past the PSi region without reacting with its interior porous sensing surface. The performance of PSi sensors is traditionally limited by slow response times for the detection of analyte with slow diffusivity. Increases in the flow rate or analyte concentration in the provided stream can enhance transport of more analyte into the sensor but at the expense of requiring a greater input of analyte. Recycling the sample multiple times over the sensor surface can improve the capturing efficiency from the sample, but suffers from a complicated design and a slowdown in binding with every cycle due to progressive depletion [146,147]. Vilensky *et al.* have recently demonstrated a novel microfluidic device that integrates an oxidized PSi sensor with electrokinetic focusing for the detection of nucleic acid [148]. First, DNA target molecules are focused in the microfluidic channel using an electric field. Then, the highly concentrated sample is transported to the PSi sensor and is held stationary to allow efficient hybridization with capture probes immobilized within the porous matrix. The authors demonstrated detection of 15-base DNA hybridization at concentrations as low as 1 nM in 20 min of analysis time. However, this technique can only be applied for the detection of charged target molecules.

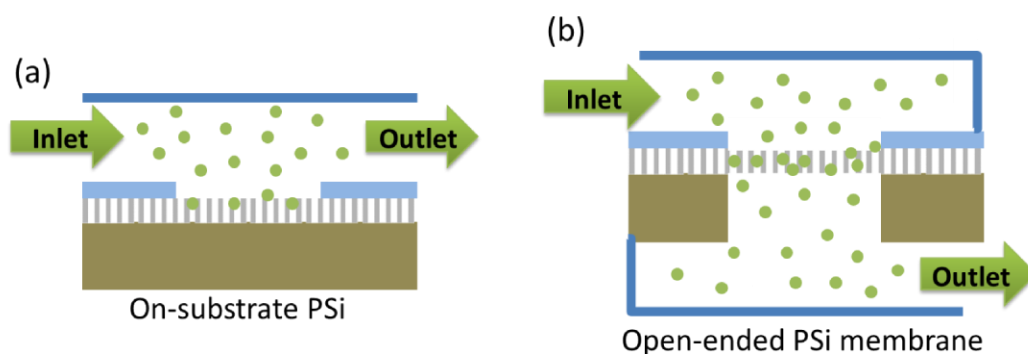


Figure 1.7. Schematic illustrations of (a) flow-over and (b) flow-through PSi sensors. Improved infiltration and mass transport can be achieved using open-ended pores in the flow-through configuration.

In order to improve the mass transport efficiency in PSi, an open-ended PSi membrane that allows analytes to flow through the pores in microfluidic-based assays and interact more favorably with the inner pore surfaces has been demonstrated [149,150]. As shown in Figure 1.7b, the PSi membrane samples were sealed between two micro-channels. The upper channel contained the inlet for the analyte solution while outlet was present in the bottom channel, forcing the solution to pass through the open-ended pores. For label-free optical biosensors, such flow-through sensing systems are predominantly based on SPR transducer approaches where an improvement in response time of the flow-through scheme over the conventional flow-over scheme has been reported [151-154]. Suspended metallic nanohole arrays have been used this way, but their reliance on expensive and sophisticated fabrication processes limits their cost-effectiveness and potential for mass production [155-157]. In this work, standard photolithography is used to pattern electrochemically etched PSi and selectively create open-ended PSi membranes, enabling low-cost high-throughput production at wafer scales [149]. For

biosensing applications, it is advantageous to utilize resonant optical structures to achieve stronger electric field localization, which leads to improved detection sensitivity. Accordingly, the PSi membranes used in this work were formed as microcavity structures. The mass transport and reaction kinetics in these PSi membranes are analyzed and are experimentally and numerically compared with those for closed-ended PSi in a flow-over scheme. The flow-through design greatly improves molecule transport efficiency in microcavity structures and reduces sensor response time as compared to the flow-over methods [149,150].

1.5 Overview of the Dissertation

This work is aimed at solving two of the key challenges in achieving practical application of PSi-based biosensors: surface passivation and efficient mass transport. The ability to mitigate charge-induced degradation and the analysis of transport and binding kinetics in open-ended and closed-ended nanopores will be an important resource for a broad scientific community interested in utilizing porous materials for various applications including batteries, fuel cells, artificial cell membranes, and biosensors.

Chapter 2 examines the influence of charge density and surface passivation on the corrosion process in PSi. In DNA sensing applications, the PSi sensing performance not only suffers from inefficient infiltration due to the length of DNA sequences, but also undergoes challenges of amplified PSi corrosion induced by the negative charges on DNA's phosphate backbone. As a result, the DNA binding, which leads to an increase in refractive index due to the hybridization event, can also induce a concurrent decrease in refractive index due to corrosion of the PSi matrix. Hence, there are competing factors that make it challenging to interpret the change in the PSi optical properties following DNA sensing. Chapter 2 provides strategies to

eliminate such sensing signal ambiguity, and proposes a mechanism behind the DNA-induced corrosion behavior in well-passivated PSi.

In **Chapter 3**, the benefit of flow-through sensing in open-ended porous materials as compared to flow-over sensing with closed-ended porous materials is quantified by solving transport equations and binding reactions using finite element method simulations, and assuming a pore diameter of 25 nm, which is consistent with the pore size of many porous semiconductors, porous oxides, and porous metals. The advantages of flow-through sensors are strongest for the detection of large molecules with low diffusivities. The analytical and numerical calculations of mass transport and binding kinetics in flow-over and flow-through pores can be applied broadly to different types of porous materials.

In **Chapter 4**, the sensing performance of PSi microcavity films in the flow over (i.e., no membrane) and flow-through (i.e., membrane) schemes is experimentally demonstrated. The PSi membrane integrated with flow-through microfluidics significantly improves mass transport of large protein molecules through the nanopores and demonstrates a 6-fold improvement in response time of streptavidin binding in comparison to a conventional flow-over PSi sensor, which is in excellent agreement with the computational predictions in Chapter 3. The enhanced analyte transport efficiency for using open-ended PSi membranes is further confirmed by quantum dot-based fluorescence measurements. A pressure test used to characterize the mechanical stability of PSi membranes is also shown in this chapter.

Chapter 5 presents a concluding summary and future research opportunities that will further improve the PSi-based sensing technologies demonstrated in this work. Overall, the improvement of surface stability and mass transport efficiency in PSi is significant progress towards fast, accurate, and reliable lab-on-chip sensing technologies based on PSi.

CHAPTER 2

DNA INDUCED CORROSION IN POROUS SILICON BIOSENSORS

2.1 Introduction

A major challenge for PSi biosensors, which also impacts PSi-based electrodes realized in lithium batteries [67,158], fuel cells [66], and supercapacitors [159], is its reactive surface that tends to make its physical structure unstable in water and various electrolytes [100]. Freshly etched PSi surfaces are hydride-terminated and are highly susceptible to oxidization and dissolution. Accordingly, PSi must be robustly passivated to enable reliable and reusable biosensing applications. Prior reports have focused on the rapid oxidation and hydrolysis (i.e., corrosion) of PSi fabricated from *p*-doped silicon that occurs when the PSi films are exposed to solutions containing negative charges. In particular, hybridization of negatively charged DNA oligonucleotides was shown to accelerate PSi dissolution [115]. It was suggested that the negative charges on the phosphate backbone of DNA attract positively charged carriers in *p*-type silicon to the PSi surface, facilitating nucleophilic attack by water molecules that ultimately leads to PSi dissolution. Importantly, in the work by Steinem *et al.*, PSi samples were weakly oxidized to produce a surface with a large fraction of Si-OH bonds and some remaining Si-H_x bonds, and then functionalized with a silane molecule and single stranded DNA. These samples experienced continuous degradation and ultimately structural collapse upon exposure to the complementary DNA sequence; this corrosion occurred at a much faster rate than background dissolution of the functionalized material in a phosphate buffer solution.

In this chapter, we expand upon prior studies to investigate the effect of DNA-induced degradation on PSi samples that are well-passivated with a thermal oxide and silane layer. PSi

waveguide structures consisting of a top, low porosity guiding layer and a bottom, high porosity cladding layer are utilized to enable highly sensitive optical measurements that quantify material added to the PSi matrix (e.g., chemical or biological molecules attached to the silicon surface) or material removed from the PSi matrix (e.g., due to corrosion). A sufficiently high DNA probe density to cause PSi corrosion is achieved in this work based on an *in situ* DNA synthesis process utilizing sequential solid-phase phosphoramidite coupling reactions [160]. Contrary to previous reports on poorly passivated porous silicon, in which corrosion led to continuous dissolution and finally structural collapse of the PSi thin film, the well passivated PSi waveguide in this work exhibits a saturation effect during the corrosion process, as reported in Ref. [122]. For practical implementation of PSi structures for DNA detection, we show that charge neutral peptide nucleic acid (PNA) probe molecules can be used to capture the desired target DNA molecules without a confounding corrosion effect. Finally, with supporting Fourier transform infrared spectroscopy (FTIR) measurements, a modified model based on nucleophilic attack of oxidized PSi surface by water molecules is proposed to explain the DNA-induced corrosion process in well-passivated PSi samples.

2.2 Fabrication of PSi Waveguides

The PSi waveguides were fabricated by electrochemical etching of *p*-type silicon wafers (<100>, 0.01-0.02 Ω -cm, 650-700 μm) in a 15% hydrofluoric acid (HF) in ethanol. Before anodization, the silicon wafer samples ($2 \times 2 \text{ cm}^2$) were first soaked in 15% HF for 1 min to remove the native oxide. The two-layer waveguide structure was then etched at 5 mA/cm^2 for 42 s to form the waveguiding layer and then 48 mA/cm^2 for 60 s to form the cladding layer. After etching, the samples were soaked in 1.5 mM KOH in ethanol for 30 min to widen pores.

Scanning electron microscope (SEM) images were used to approximate the porosities, pore diameters, and layer thicknesses for these waveguide structures. The resulting PSi waveguide layer has a refractive index of approximately 1.77, pore diameters ranging from 15 - 25 nm, and a thickness of approximately 220 nm. The bottom, cladding layer has slightly larger pore diameters, a refractive index of approximately 1.32 and a thickness of approximately 1400 nm.

2.3 Surface Functionalization

2.3.1 In Situ DNA Synthesis

PSi waveguides were first thermally oxidized in a furnace (Lindberg Blue M) in ambient air at 800 °C for 30 min. Following oxidation, a hydroxyl-terminated silane, N-(3-triethoxysilylpropyl)-4-hydroxybutyramide (TEOS-HBA) was used to functionalize the PSi surface with reactive moieties used to initiate DNA oligo nucleotide synthesis from the waveguide surface. The oxidized waveguide samples were incubated in a 4% solution of TEOS-HBA, composed of 83 µL TEOS-HBA, 100 µL deionized (DI) water, and 1900 µL ethanol, for 4 hours at room temperature. The samples were then rinsed with ethanol to remove excess solvents, and annealed at 200 °C for 16 hours in the furnace in ambient air. The annealing step cross-links neighboring silane molecules, increasing the hydrolytic stability of the silane coating [121]. Samples were then soaked in DI water at room temperature for at least 4 hours to remove weakly bound multilayers of silane molecules.

DNA probes were synthesized within silanized waveguides using an Applied Biosystems Model 392 DNA Synthesizer that was modified to direct reagent flow onto the waveguide surface for base-by-base oligonucleotide synthesis in PSi. The phosphoramidite method was used as described previously [160]. Ultra-mild phosphoramidites and reagents (Glen Research) were

used to allow for a moderate, basic deprotection step and reduce the possibility of PSi dissolution during DNA synthesis. A 16-mer probe DNA sequence (5'-TAG CTA TGG TCC TCG T-3') with a melting temperature of 50 °C in 4-(2-hydroxyethyl)-1-piperazineethanesulfonic acid (HEPES) buffer solution was synthesized. HEPES buffer solution was prepared by dissolving 20 mM HEPES, 150 mM NaCl, and 5 mM ethylenediaminetetraacetic acid (EDTA) in 1000 mL DI water. The resulting ionic strength was 110 mM. NaOH or HCl was used to adjust the pH of HEPES buffer to 7.4. After completion of DNA synthesis, the PSi waveguide was rinsed with ethanol and water. Cyanoethyl groups attached to synthesized DNA molecules block the negative charges on the phosphate backbone and need to be removed together with protection groups on each base (phenoxyacetyl protection for adenine, 4-isopropyl-phenoxyacetyl protection for guanine, and acetyl protection for cytosine) before hybridization. Synthesized DNA probe molecules were activated for sensing by deprotection in a 1:1 volume ratio solution of ethylenediamine and ethanol for 30 min at room temperature.

2.3.2 *In Situ* PNA Synthesis

Waveguides were first thermally oxidized in the furnace in ambient air at 800 °C for 30 min and then functionalized with 1% 3-aminopropyltriethoxysilane (3-APTES) in anhydrous toluene for 20 min at room temperature. The silanized waveguides were thermally annealed at 150 °C in ambient air for 20 min to promote stable 3-APTES monolayer formation and then soaked at room temperature in HEPES buffer for 1 hour to remove weakly bound silane multilayers. *In situ* PNA synthesis of the same 16-mer sequence used for probe DNA (5'-TAG CTA TGG TCC TCG T-3') was conducted directly on APTES-functionalized PSi within a PS3 automated peptide synthesizer (Protein Technologies). Monomers for PNA synthesis, rink amide LL resin, and 2-

(6-chloro-1H-benzotriazole-1-yl)-1,1,3,3-tetramethylamminium hexafluorophosphate (HCTU) activator were purchased from PNA Bio, EMD Millipore, and Chempep , respectively. The synthesis process is described in detail in Ref. [161].

2.3.3 Nucleic Acid Sensing

100% Complementary target DNA (5'-ACG AGG ACC ATA GCT A-3') and 100% non-complementary mismatch DNA (5'-GGT TTC TGA TGC TGA C-3') purchased from Eurofins MWG Operon were diluted to 100 μM in HEPES buffer and stored at $-20\text{ }^\circ\text{C}$. Immediately prior to hybridization, 10 μL of the 100 μM DNA solution was diluted to a working concentration of 10 μM in 90 μL HEPES buffer. PSi waveguides functionalized with either probe DNA or probe PNA were incubated in 100 μL solutions of 10 μM target DNA as well as mismatch DNA. Uncharged PNA molecules with the same sequence as complementary target DNA were purchased from BioSynthesis Inc and were utilized to hybridize with PNA probes in order to prevent PSi corrosion associated with negative charges on target DNA. The 10 μM target PNA solutions were prepared by diluting 100 μM PNA in HEPES buffer. Magnesium chloride hexahydrate ($\text{MgCl}_2 \cdot 6\text{H}_2\text{O}$) was dissolved into the HEPES buffer solution used for target DNA hybridization with synthesized PNA probes at a concentration of 2 M in order to shield the negative charges on DNA and evaluate the resulting effect on PSi corrosion. All hybridization experiments were performed at room temperature.

2.4 Prism Coupling Measurements

A Metricon 2010 prism coupler employing a rutile prism ($n_{prism} = 2.1677$) in the Otto configuration was used to evanescently couple a TE polarized 1550 nm laser beam into the waveguide. At a specific resonant angle, the light is coupled through the prism into the

waveguide; otherwise the light is entirely reflected. Therefore, a dip in the reflectance spectrum is observed for each coupled mode. The resonant angle directly corresponds to the effective refractive index of the waveguide according to the relation

$$n_{eff} = n_{prism} \sin\theta \quad (2.1)$$

where n_{eff} and n_{prism} are the effective index of the waveguide and refractive index of the prism, respectively, and θ is the angle of incidence of light in the prism corresponding to the resonant angle. Molecule infiltration inside the pores of the PSi waveguide causes the refractive index of PSi to increase, leading to a redshift (i.e., shift to higher angle) of the resonant angle. On the contrary, loss of materials inside the PSi waveguide, for example due to corrosion of the PSi matrix, causes the refractive index to decrease, resulting in a blueshift (i.e., shift to lower angle) of the resonant angle. The magnitude of the resonant angle shift correlates to, and allows quantification of, the amount of material added to or removed from the PSi waveguide. The resolution of the Metricon 2010 prism coupler used in this work is 0.002 °.

2.5 Characterization of PSi Passivation

The degree of passivation of the PSi waveguides after thermal oxidation and silanization in TEOS-HBA was first established through prism coupling measurements following exposure to an aqueous environment. Thermal oxidation produces a SiO₂ layer and Si-O-Si bonds, leaving the PSi surface free of hydrides and thus less susceptible to corrosion in aqueous environments. The oxidation process also yields sufficient Si-OH surface groups, which are necessary for TEOS-HBA silane attachment [116]. While a complete monolayer coating of silane would serve to further passivate the PSi surface against corrosion, the TEOS-HBA silane tends to form in multilayer islands [162]. Figure 2.1a shows reflectance spectra taken by prism coupling of an

oxidized PSi waveguide after silanization and subsequent soaking in DI water over the course of several hours. The redshift of the waveguide resonance following silanization confirms that silane molecules are attached to the waveguide while the subsequent resonance blueshift after the first two hours of exposure to DI water indicates a loss of material from the PSi waveguide, likely due to removal of loosely bound silane molecules. After 4 hours in DI water, the resonant angle shift stabilized and additional water exposure resulted in negligible shifts in resonance angle (Figure 2.1b), implying that the remaining silane film is hydrolytically stable.

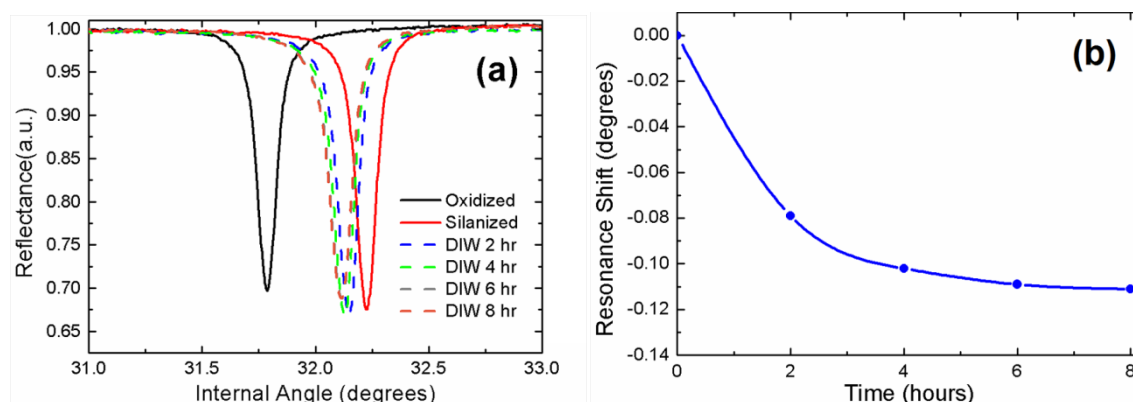


Figure 2.1. (a) Stabilization of silanized PSi waveguides. Reflectance spectra are given for a PSi waveguide after oxidation (black, solid line), TEOS-HBA silanization (red, solid line), and soaking in DI water for 2, 4, 6, or 8 hours (blue, green, gray, orange dashed lines, respectively). Hydrolysis is indicated by shifts of the resonance to lower angles after soaking in DI water. (b) Resonance angle shift as a function of time during DI water soak. Reprinted with permission from Ref. [122]. Copyright 2014 American Chemical Society.

The fractional coverage of the molecules in the PSi waveguide can be determined by using transfer matrix theory [163] and Lugo's three component effective medium model [164] to fit the

magnitude of the resonance angle shifts according to established procedures [96]. Using this method, we found that the shift in resonance angle due to silanization shown in Figure 2.1, 0.392° , corresponds to a sub-monolayer surface coverage of approximately 34%. This value should be treated as an upper bound since multilayer islands of silane molecules may still exist on the surface after the annealing and hydrolysis process. According to previous studies on TEOS-HBA silane functionalized PSi, higher coverage up to nearly 90% can be achieved in PSi waveguides through extended incubation in TEOS-HBA solutions [162]. However, the lower silane coverage was chosen in this work because the surface coverage of silane molecules is directly related to the ensuing probe DNA density in the PSi waveguide and it has been shown that an approximately 25% probe DNA coverage in PSi waveguides minimizes steric hindrance and results in the largest sensor response upon exposure to complementary target oligos [165].

2.6 Influence of Probe DNA on PSi Corrosion

As shown in Figure 2.2a, 16-mer probe DNA synthesis on the silanized PSi waveguides led to a large resonance redshift, confirming molecule attachment. Subsequent deprotection of the DNA probes to give them the structures needed for sensing resulted in a small blueshift, corresponding to the removal of the protecting groups from the DNA chains. Based on the overall measured resonance shift of the PSi waveguide resonance due to activated probe DNA attachment (1.113°), the 16-mer probe DNA surface coverage was estimated to be approximately 31%, assuming no corrosion resulted from the attachment process and assuming all sequences were complete 16-mer DNA strands. We note that the magnitude of the resonance shift from probe DNA attachment is larger than from silane attachment due to the respective sizes of the molecules (16-mer DNA ≈ 3.52 nm long; TEOS-HBA silane molecule ≈ 0.9 nm long).

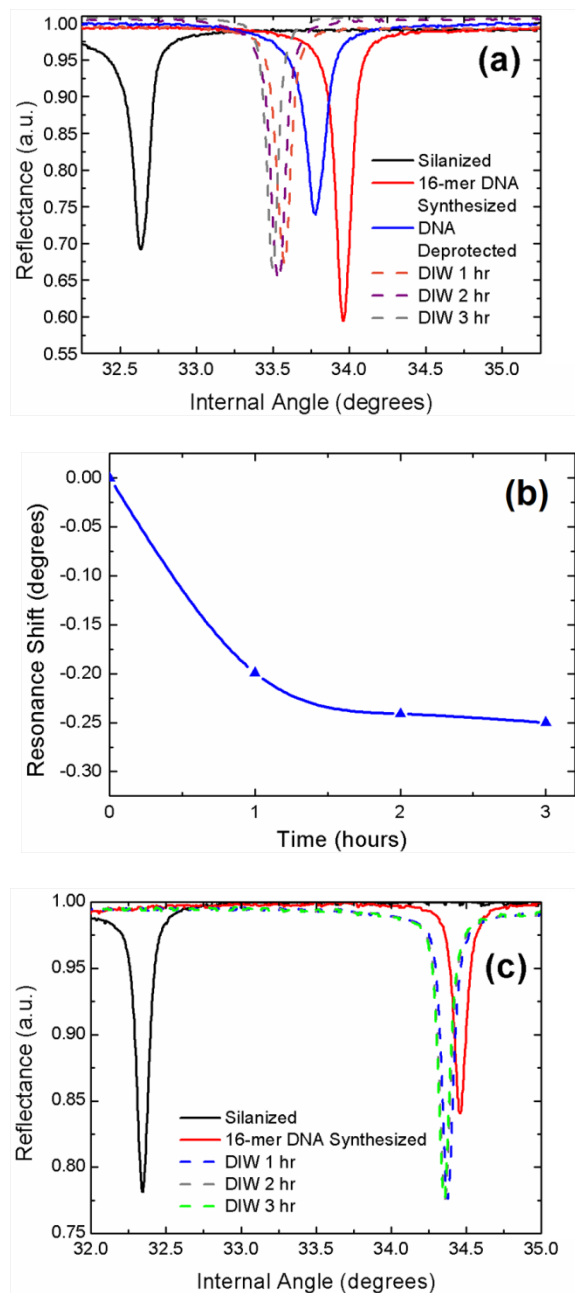


Figure 2.2. Optical characterization of *in situ* DNA probe synthesis and subsequent degradation of an activated PSi waveguide biosensor in DI water. (a) Probe DNA was synthesized from a stabilized PSi waveguide functionalized with TEOS-HBA silane (black, solid line). Reflectance

spectra following *in situ* synthesis of 16-mer DNA probe and deprotection of charge-masking groups from the sugar-phosphate backbone are indicated by red and blue solid lines, respectively. Incubation of the deprotected probe DNA molecules with negatively charged backbones in DI water results in a blueshift to lower resonant angles (dashed lines). (b) Resonance angle shift as a function of time during DI water soak after probe DNA deprotection. (c) Reflectance spectra of a PSi waveguide stably functionalized with TEOS-HBA silane (black solid line), after *in situ* synthesis of probe DNA molecules that have not been deprotected (red solid line), and after soaking the waveguide in DI water (dashed lines). Reprinted with permission from Ref. [122]. Copyright 2014 American Chemical Society.

The stability of the PSi waveguides functionalized with *in situ* synthesized probe DNA molecules against corrosion was evaluated by soaking in DI water. Prior studies did not report any corrosion due to the attachment of negatively charged probe DNA molecules [115] and similar studies performed in our group with pre-synthesized DNA probes having approximately 10% surface coverage also did not show any measurable corrosion effect, likely due to the relatively low concentration of negatively charged species [166]. As shown in Figure 2.2 a, b, a blueshift of the waveguide resonance angle with a magnitude that gradually decreases after the first hour of exposure to DI water was measured, suggesting that the concentration of negative charge provided by the *in situ* synthesized DNA probes is large enough to lead to measurable corrosion. Since removal of the protecting groups following *in situ* synthesis leaves the backbone of the probe DNA molecule negatively charged, control experiments on PSi waveguides functionalized with *in situ* synthesized charge-neutral DNA probes that have not been deprotected could be conducted. Such negative control experiments were performed using

protected probe DNA and showed that a smaller waveguide resonance blueshift occurred during the first hour of exposure to DI water and ceased thereafter (Figure 2.2c). Thus, without deprotection, the charge neutral DNA probe molecules do not facilitate oxidative corrosion of the PSi surface. From these experiments, we conclude that there may be a small quantity of residual chemicals from the *in situ* synthesis process or a small quantity of additional incompletely cross-linked silane monomers that are removed during the first hour of DI water exposure to the probe DNA functionalized PSi waveguides but there is clearly concurrent and measurable corrosion that occurs due to the presence of the negative charges on the sugar-phosphate backbones of the deprotected DNA probe molecules. Accordingly, to minimize corrosion effects that may potentially mask the binding signal from target DNA molecules during DNA hybridization assays, all *in situ* DNA probe-functionalized waveguides were stabilized in DI water for at least 2 hours after deprotection.

2.7 Influence of DNA Hybridization on PSi Corrosion

Using the stabilized PSi waveguides with *in situ* synthesized DNA probes, the effect of corrosion upon DNA hybridization was investigated. As shown in Figure 2.3, hybridization with 10 μM complementary DNA target molecules caused the PSi waveguide resonance angle to blueshift approximately 0.1° , suggesting that even though these waveguides were well-passivated, corrosion of the PSi upon exposure to the DNA duplex occurs.

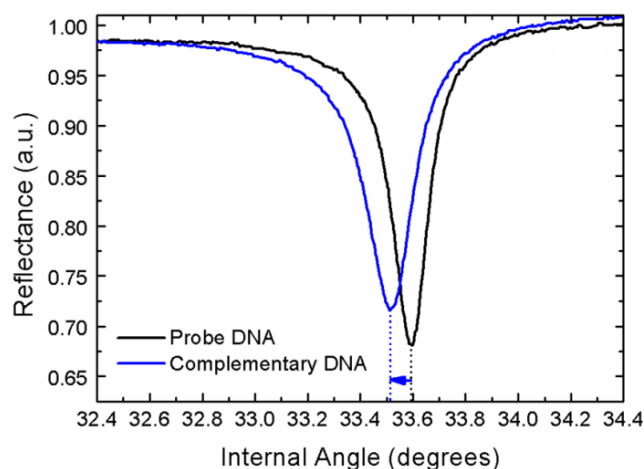


Figure 2.3. Resonance angle blueshift upon hybridization of a 100% complementary DNA target (10 μM) with DNA probes synthesized on a PSi waveguide. Reprinted with permission from Ref. [122]. Copyright 2014 American Chemical Society.

6-FAM labeled DNA target molecules (absorption maximum near 494 nm, emission maximum near 525 nm) were used to confirm the presence of DNA duplexes within PSi. A 488nm laser (Coherent OBIS) was operated at 4 mW to excite 6-FAM emission. A fiber-coupled Ocean Optics USB400 CCD spectrometer was used to record 6-FAM emission between 500 nm and 800 nm. PSi waveguides functionalized with *in situ* synthesized 16-mer DNA probes were exposed to complementary DNA targets labeled with 6-FAM. The fluorescence spectrum of this sample showed a noticeable peak near 525 nm (red line), corresponding to the emission maximum of 6-FAM fluorescein. A control sample functionalized with a DNA probe sequence not complementary to the fluorescently labeled target DNA did not show any peak near 525 nm (black dotted line).

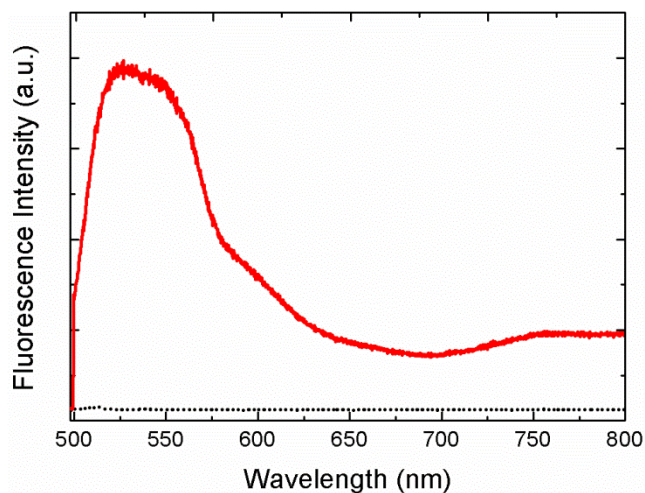


Figure 2.4. Fluorescence spectra of porous silicon waveguides functionalized with probe DNA complementary (red solid line) and not complementary (black dotted line) to 6-FAM labeled DNA target that was exposed to both waveguides. A distinct fluorescence signature indicating DNA hybridization is only present for the complimentary probe-target system.

To verify that the measured blueshift is due to corrosion upon DNA hybridization, a 100% mismatch 16-mer DNA sequence was used as a control and no shift of the resonance angle was detected (Figure 2.5). Therefore, the formation of DNA-DNA hybrids at the waveguide surface is necessary for the corrosion observed in Figure 2.3. The role of the DNA surface coverage should also be considered to understand the observed corrosion effect upon DNA hybridization in PSi. Previous work reported that ozone oxidized PSi did not exhibit corrosion during DNA hybridization unless the target DNA was labeled with a charge-carrying metal complex [167]; however, the probe DNA coverage in that work was estimated to be 1-2 nmol cm⁻² while our probe DNA coverage is estimated to be one order of magnitude higher (10-25 nmol cm⁻²) due to the *in situ* DNA synthesis process.

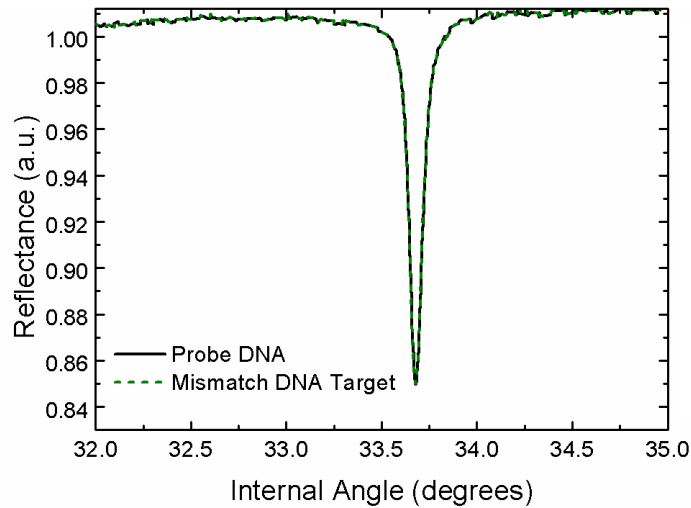


Figure 2.5. No waveguide resonance shift is observed upon exposure of an *in situ* probe DNA functionalized PSi waveguide to a 100% mismatch DNA sequence.

A key distinction in this work compared to a previous study utilizing poorly passivated PSi samples [115] is that the corrosion of the passivated PSi waveguides is not a continuous process that results in complete dissolution of the PSi structure, but rather the extent of corrosion appears to saturate over time. An examination of the time-dependent shift in waveguide resonance angle in Figure 2.6 reveals that the PSi waveguide resonance ceases to shift to lower angles after 2 hours of incubation with complementary DNA targets; a saturating redshift of smaller magnitude than the corrosion-dominated blueshift was observed upon further incubation. These shifts suggest that PSi corrosion initially occurs at a rate fast enough to mask DNA binding events. As the corrosion progresses, the corrosion rate appears to slow down, similar to what was observed upon *in situ* synthesized probe DNA attachment, and a resonance redshift can be observed due to continued target DNA binding. However, the overall PSi waveguide resonance shift due to target DNA binding is to a smaller angle indicating that the corrosion effect would dominate the

measured transduction signal for DNA sensor applications when well-passivated PSi waveguide sensors are functionalized with DNA probe molecules.

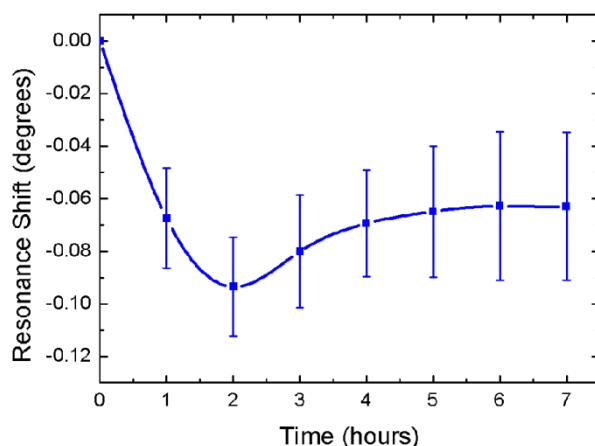


Figure 2.6. Resonance angle shift of PSi waveguide as a function of incubation time with 100% complementary DNA sequence. Reprinted with permission from Ref. [122]. Copyright 2014 American Chemical Society.

Since the doubling of negative charges on the surface during hybridization increases corrosion, it is expected that, in general, PSi corrosion is enhanced with increasing target DNA concentration. As shown in Figure 2.7, a study of the effect of DNA target concentration on PSi corrosion after 1 hour exposure reveals that the corrosion level on passivated PSi waveguides increases with DNA target concentration, reaching a saturation as evidenced by no additional resonance blueshift for concentrations above approximately 10 μM . As the target DNA concentration reaches this threshold value, most of the accessible probe DNA molecules have been hybridized by complementary DNA targets within the 1 hour measurement. Hence, both the resonance blueshift, which is likely due to corrosion of exposed Si-OH bonds, and the resonance redshift due to target DNA attachment saturate.

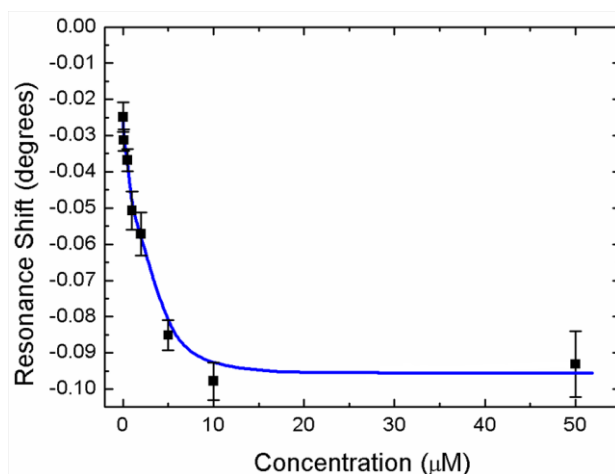


Figure 2.7. Dependence of PSi biosensor corrosion on target DNA concentration. Waveguide resonance blueshift upon one hour incubation with 100% complementary DNA sequence at different concentrations. The line is shown as a guide to the eye. Reprinted with permission from Ref. [122]. Copyright 2014 American Chemical Society.

2.8 Mitigating DNA Induced Corrosion in PSi

DNA hybridization and PSi corrosion can happen simultaneously, and the redshift resulting from target DNA binding can therefore be obscured by the blueshift resulting from corrosion. This obscurity must be eliminated in order to quantitatively determine molecule infiltration into PSi. The first strategy presented to mitigate PSi corrosion is to decrease the concentration of negative charges within the sensing volume by replacing negatively charged DNA molecules with charge neutral PNA molecules. The second anti-corrosion strategy discussed herein is to shield the negatively charged DNA during biosensing with cations such as Mg^{2+} .

2.8.1 DNA Hybridization with Synthesized PNA Probes

One possible strategy for preventing PSi surface corrosion during functionalization and minimizing the corrosion during target DNA hybridization is to replace DNA probes with

neutrally-charged PNA probes. In this way, a smaller concentration of negative charge attaches to the functionalized PSi surface during target DNA capture. Meanwhile, due to its uncharged polyamide backbone, PNA can hybridize to negatively charged DNA without electrostatic repulsion, which increases the rate of hybridization and binding affinity [168,169]. As a direct analog of the *in situ* synthesis method of growing DNA probe molecules base-by-base inside the PSi waveguide, a recently developed method of *in situ* probe PNA synthesis was employed in PSi waveguides [161]. Based on the magnitude of the resulting waveguide resonance shift, a similar surface coverage of probe PNA molecules ($\approx 28\%$) as compared with DNA molecules ($\approx 31\%$) was achieved after PNA synthesis and deprotection. As shown in Figure 2.8, soaking the PNA probe functionalized PSi waveguide sample in DI water yielded a small blueshift that saturated after 1 hour (-0.061°) similar to that observed when the PSi waveguide functionalized with protected, neutrally charged, DNA probes was soaked in DI water (Figure 2.2c). This suggests that no oxidative corrosion occurs on the probe PNA functionalized PSi structure.

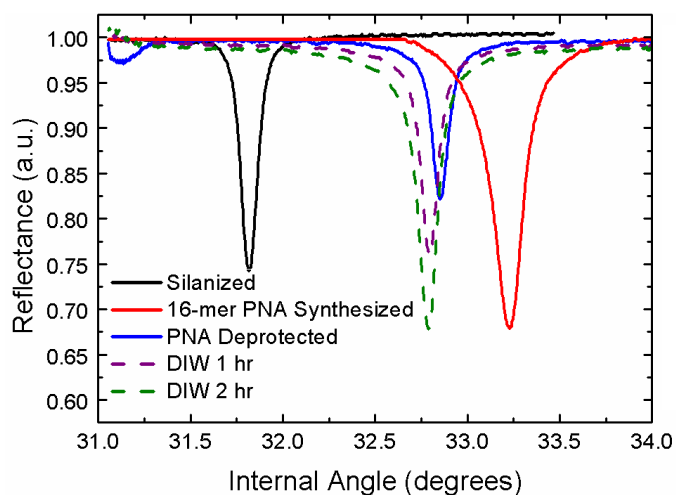


Figure 2.8. Response of PSi waveguide functionalized with 3-APTES silane (black, solid line) and *in situ* synthesized probe PNA (as-synthesized: red, solid line; deprotected: blue, solid line)

upon exposure to DI water. Following a slight initial blueshift (dashed lines) no additional shift is observed, suggesting that neutrally-charged PNA probes do not cause PSi corrosion.

Figure 2.9a shows that a waveguide resonance redshift of 0.068° was observed after 1 hour incubation of the PNA functionalized PSi sample with $10\ \mu\text{M}$ complementary DNA in HEPES buffer. Hence, the dominant effect is clearly PNA-DNA hybridization. As a control, a negligible shift was observed after incubation with a 100% mismatch DNA sequence (Figure 2.9b).

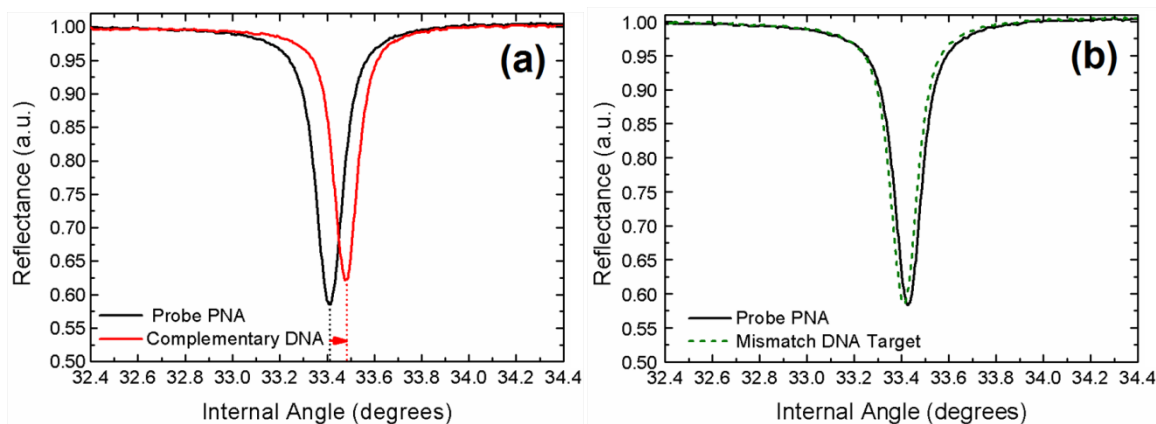


Figure 2.9. Functionalization of PSi waveguide surface with neutrally-charged PNA probes mitigates waveguide corrosion during hybridization with DNA targets. Resonance shifts are shown for a PNA probe-functionalized PSi waveguide upon incubation with (a) 100% complementary DNA sequence and (b) 100% mismatch DNA sequence. Reprinted with permission from Ref. [122]. Copyright 2014 American Chemical Society.

In order to determine whether corrosion still occurs during DNA hybridization to PNA probes, we conducted an experiment in which PNA target molecules were hybridized to *in situ* synthesized PNA probe molecules in a passivated PSi waveguide. In this case, no negative

charges are present and the only effect on the waveguide resonance shift is the material addition due to PNA attachment. Figure 2.10 shows that a waveguide resonance redshift of 0.152° was observed after 1 hour incubation of the PNA functionalized PSi sample with $10\ \mu\text{M}$ complementary PNA in DI water. The PNA-PNA duplex has a rise per base pair of $3.2\ \text{\AA}$, similar to the rise per base pair in a PNA-DNA helix ($3.5\ \text{\AA}$); however, the PNA-PNA duplex is a wider helix with a diameter of $28\ \text{\AA}$ compared to the PNA-DNA helix that has a diameter of $22\ \text{\AA}$ [170,171]. Considering the respective sizes of PNA-DNA and PNA-PNA hybrids, if no corrosion effect occurs during PNA-DNA hybridization, the redshift observed for target PNA attachment would be about 1.5 times larger than the redshift observed for target DNA attachment, corresponding to a PNA-PNA hybridization redshift of approximately 0.10° . However, since the measured resonance redshift for PNA-PNA hybridization (0.152°) was larger than this value, we concluded that even with utilization of a charge neutral PNA probe molecule, DNA sensing in PSi is still challenged by corrosion during the hybridization of the negatively charged DNA molecules. Note that for both PNA-DNA binding and PNA-PNA binding, relatively low hybridization efficiencies were observed, likely due to size-dependent molecular infiltration challenges for the target molecules [112]. If all of the probe PNA molecules capture target PNA molecules, then a resonance shift of nearly equal magnitude to that shown by the waveguide after probe PNA attachment would be observed while if all probe PNA molecules capture DNA targets, a 1.5 times smaller magnitude resonance shift compared to that shown by the waveguide after probe PNA attachment would result. While a non-ambiguous waveguide resonance redshift is observed for target DNA hybridization to probe PNA molecules, the overall response of the sensor is still compromised by the concurrent blueshift that occurs due to corrosion. Therefore, the sensitivity of the sensor is also compromised by the corrosion effect.

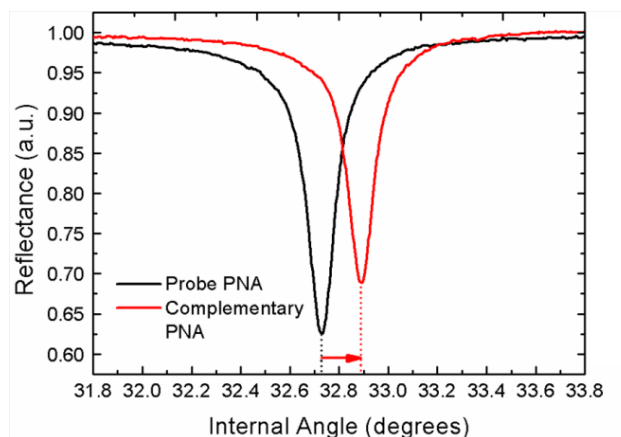


Figure 2.10. Resonance shift for a PNA probe-functionalized PSi waveguide upon incubation with 100% complementary PNA oligo target.

2.8.2 Compensating DNA Charge with Magnesium

In order to more completely shield the PSi surface from the negative charges on the phosphate groups of the target DNA molecules, and to fully mitigate DNA-induced corrosion of PSi, Mg^{2+} ions were introduced into the incubation solution used for target molecule hybridization with synthesized PNA probes, following results reported in Ref. [115], Mg^{2+} ions have a positive two charge; thus, when binding to the DNA strands, they can shield the negative charge accumulated at the PSi surface more effectively than cations with a single positive charge, such as Na^+ , K^+ [172,173]. Shielding of the negative charges accumulated at the PSi surface prevents PSi corrosion and enhances the detection signal for the PNA functionalized PSi waveguide, as shown by the increased magnitude of the waveguide resonance redshift from 0.068° (no $MgCl_2$ in buffer, Figure 2.9a) to 0.107° (2 M $MgCl_2$ in buffer, Figure 2.11a) upon hybridization with $10\ \mu M$ 100% complementary target DNA molecules after 1 hour incubation. The magnitude of the redshift observed after DNA hybridization in the presence of Mg^{2+} ions is about 1.4 times smaller than the sensing results with PNA hybridization, which is consistent with

the respective sizes of the PNA-DNA and PNA-PNA helices and suggests that the Mg^{2+} ions effectively mitigate the DNA-induced corrosion process during hybridization. A negligible resonance shift was detected for mismatch DNA target in the same buffer solution with Mg^{2+} , suggesting there are no non-specific binding events (Figure 2.11b).

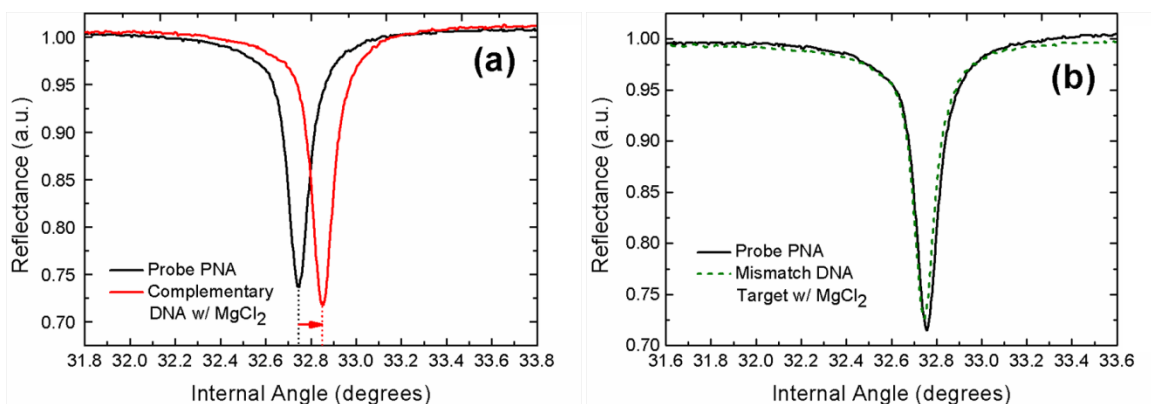


Figure 2.11. Addition of Mg^{2+} ions mitigates PSi waveguide corrosion during hybridization of DNA targets to PNA probes. Resonance shifts are shown upon incubation with (a) 100% complementary DNA and (b) 100% mismatch DNA in the presence of 2 M $MgCl_2$. Reprinted with permission from Ref. [122]. Copyright 2014 American Chemical Society.

The detection sensitivity of the well-passivated PSi waveguide functionalized with *in situ* synthesized probe PNA was estimated through exposure to various concentrations of DNA target molecules in the presence of 2 M $MgCl_2$. As shown in Figure 2.12, a detection limit near 10 nM is expected. For target DNA concentrations above approximately 10 μ M, the saturation of the resonance redshift suggests that most of the accessible probe molecules are hybridized with target molecules, which agrees well with the saturation effect observed for DNA-DNA hybridization in Figure 2.7. Although a detection limit near 0.1 nM was reported for a PSi single

layer biosensor based on exploitation of the corrosion effect with a poorly passivated film [167], the repeatability and reliability of the sensing results are sacrificed using this corrosion-based transduction approach.

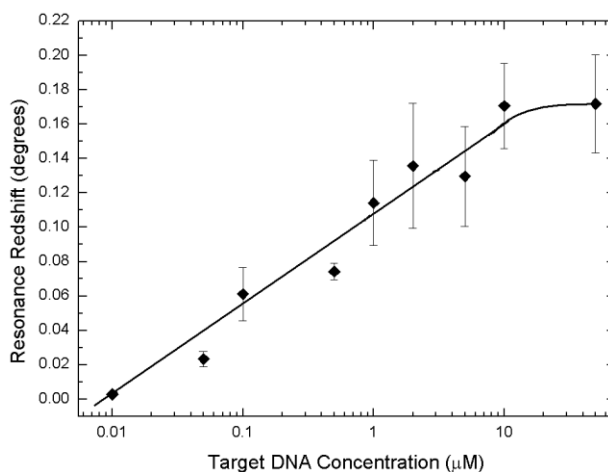


Figure 2.12. Resonance redshift of PSi waveguide functionalized with *in situ* synthesized PNA probes upon one hour hybridization with 100% complementary DNA at various concentrations in the presence of 2 M MgCl_2 . The line is shown as a guide to the eye.

2.9 Mechanism of Corrosion on Passivated PSi

Based on the experimental measurements characterizing the effect of corrosion in PSi waveguides, we propose a model in which the corrosion in PSi waveguides depends on the surface charge density and passivation conditions of the PSi structures. When the surface coverage of the immobilized DNA molecules increases, the amount of negative charge associated with DNA increases as well. The accumulation of negative charges near the PSi surface attracts the majority carriers of *p*-type PSi to move to the vicinity of the DNA binding event, which enhances the localized electric field near the DNA-oxide interface. This electric field may promote further oxidation of the Si pore wall and result in a blueshift of the PSi

waveguide reflectance spectrum. However, an enhanced electric field is unlikely the main reason for the PSi corrosion that is experimentally observed as the increased silicon oxidation rate reported previously in literature requires an applied electric field of approximately 10^4 V/cm with a high temperature of 850°C [174], which is not applicable to the PSi DNA sensors studied in this work. Another possible explanation for PSi corrosion is the electrical double layer, with one polar component of the electrolyte being preferentially accumulated at the electrode surface and in the diffuse layer, while the other polar component is depleted in the same region [175]. The electrical double layer was reported to accelerate the wet etching of SiO_2 by locally increasing the concentration of hydroxide around a hydrophobic carbon nanotube [176]. However, electric double layer formation is also not likely the predominant reason for the observed corrosion effect because a hydrophilic, thermally oxidized PSi surface functionalized with silane molecules and negatively charged DNA strands cannot adsorb the high effective concentration of hydroxide that would be necessary to accelerate SiO_2 etching. According to a previously proposed mechanism for DNA hybridization enhanced corrosion, which is the most likely cause of PSi corrosion, the accumulation of negatively charged DNA near the PSi surface enhances the polarization of surface silicon bonds and facilitates nucleophilic attack by water molecules starting at exposed Si-H bonds [115]. As shown in Figure 2.13, the FTIR spectrum of a freshly etched PSi waveguide showed strong reflectance in the region from 2038 to 2280 cm^{-1} and at 900 cm^{-1} attributed to Si-H_x ($x = 1, 2, 3$) groups on the surface. After thermal oxidation at 800°C for 30 min, PSi waveguide samples showed FTIR spectral signatures for Si-O-Si bonds from 900 to 1300 cm^{-1} and 800 cm^{-1} , and the isolated SiO-H stretching at 3750 cm^{-1} [116]. The spectral band representing Si-Si bonding near 620 cm^{-1} as well as the bands for Si-H_x bonds disappear after oxidation, indicating that the PSi waveguide structure has been well-oxidized.

Due to the low sensitivity of the IR measurement, it is not possible to confirm complete oxidation of the PSi waveguide surface based on the disappearance of Si-Si and Si-H_x bands. Disappearance of the Si-H_x groups after thermal oxidation, however, does indicate good passivation of the PSi waveguide surface. The Si-H bond is a reducing agent and is susceptible to nucleophilic attack by water. Oxidation first turns the surface silicon atoms into Si-OH bonds. Further oxidation results in condensation of neighboring surface Si-OH bonds forming Si-O-Si bridges, which contribute to passivation of the PSi surface [177]. Following silanization, the FTIR spectrum shows characteristic peaks for triethoxysilane in the region around 1595 cm⁻¹. The isolated peak at 3750 cm⁻¹ for SiO-H disappears after silane attachment. The region of PSi covered by silane is well passivated by a covalent Si-O-Si bonding pattern on the surface; however, any remaining Si-OH bonds on PSi surface are susceptible to nucleophilic attack by water molecules. After *in situ* synthesis of 16-mer DNA molecules, characteristic peaks for DNA appears in the region from 1500 to 1800 cm⁻¹.

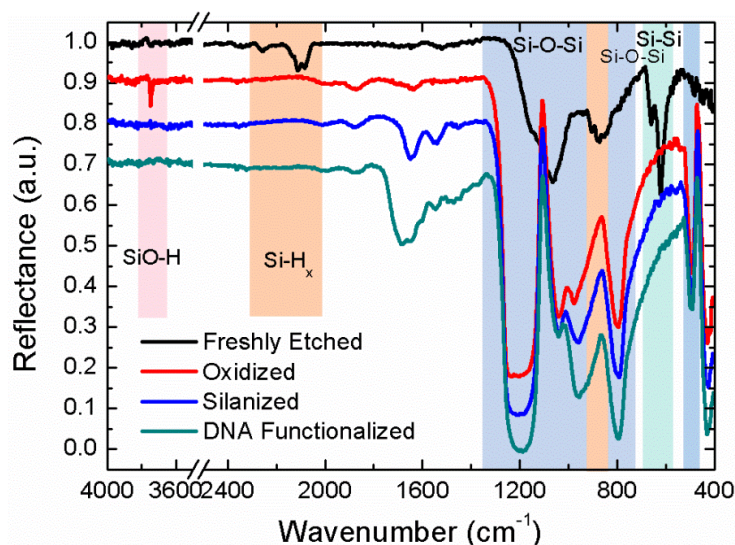


Figure 2.13. FTIR spectra of PSi waveguide freshly etched, oxidized at 800 °C for 30 min, functionalized with TEOS-HBA silane, and with deprotected 16-mer DNA probes. Reprinted with permission from Ref. [122]. Copyright 2014 American Chemical Society.

The presence of Si-O-Si bonds at the PSi waveguide surface even after synthesis of DNA probes provides a mechanism for the DNA-induced corrosion observed throughout this study. We propose the following scheme for DNA-induced corrosion of PSi waveguides passivated with thermal oxide, TEOS-HBA silane, and *in situ* synthesized probe DNA molecules. Before deprotection, a cyanoethyl group masks the negative charges on the probe DNA backbones (Figure 2.14a). Following deprotection, the corrosion process initiates at Si-O-Si bonds adjacent to immobilized DNA probes (Figure 2.14b). During hybridization, the local concentration of negative charges in the PSi matrix increases due to target DNA binding (Figure 2.14c). The increased concentration of negative charges enhances the corrosion rate of the PSi surface in regions that are not passivated by silane and PNA/DNA molecules. Si-O bonds on oxidized PSi surfaces are highly polarized, and thus, susceptible to nucleophilic attack, according to the reaction equations in Figure 2.14.

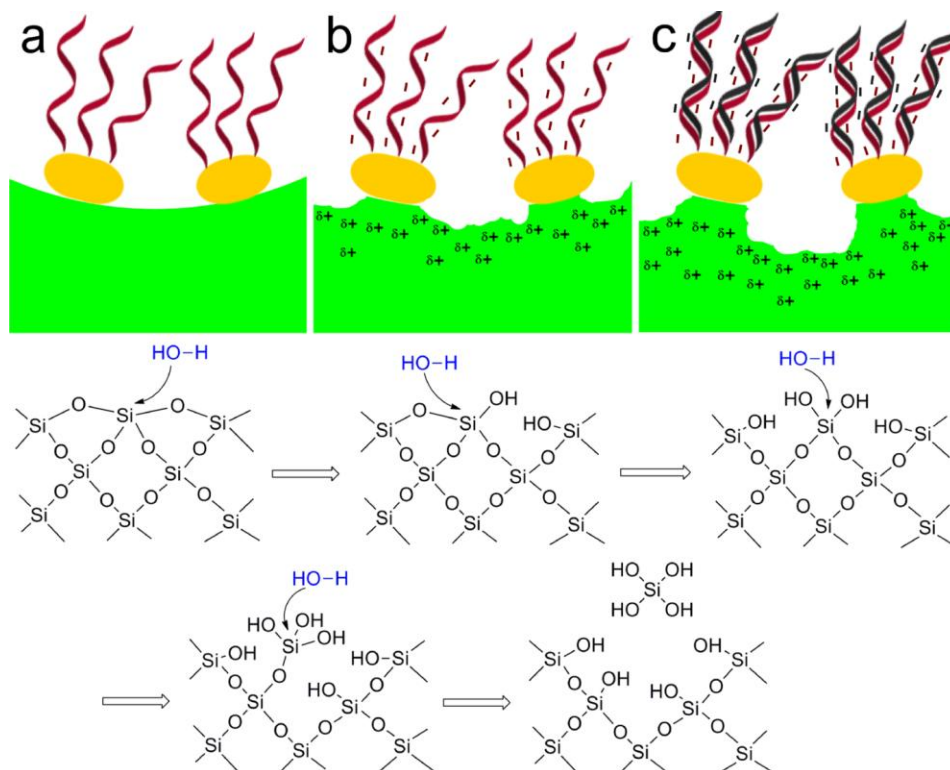


Figure 2.14. Schematic of the DNA induced corrosion process in PSi illustrating surface regions of the waveguide structure. The green region indicates the thermal oxide on pore walls; the yellow represents silane molecules; DNA oligos are represented by the red (probe) and black (target) helix structures attached on the silane molecules. The chemical reactions present a possible mechanism for corrosion of a silicon atom initiated by sequential nucleophilic attacks by water molecules and resulting in the release and dissolution of the atom in the form of $\text{Si}(\text{OH})_4$. Reprinted with permission from Ref. [122]. Copyright 2014 American Chemical Society.

Negatively charged DNA at the surface enhances the polarization of silicon bonds; therefore, positive charges in *p*-type PSi accumulate near the surface where DNA binding events occur. The resulting highly polarized and reactive surface-bound silicon atoms are prone to

chemical attack by water molecules, leading to accelerated corrosion of PSi. On poorly passivated PSi samples, the low energy required to break Si-H and Si-Si bonds (bond energies of 318 kJ/mol and 197 kJ/mol, respectively) leads to continued corrosion. In the case of well passivated PSi, the blueshift of the resonance angle resulting from corrosion was most pronounced during the first two hours of incubation. The corrosion rate slows down for longer incubation times, as the energy required to break Si-O bonds with average bond energy of 368 kJ/mol is higher than that required to break Si-H and Si-Si bonds. When the corrosion progresses deeper into the pore walls and reaches the underlying Si-O-Si bridges formed during thermal oxidation, the polarization enhancement of silicon bonds resulting from negatively charged DNA on the surface ceases, making nucleophilic attack towards Si atoms by water molecules more difficult and preventing continued corrosion of PSi. Thus, the corrosion process for passivated PSi waveguide samples was observed to saturate over time. Importantly, this saturation of the corrosion process allows reusability of the passivated PSi sensor. In this work, the PSi waveguide sensor was reused for DNA detection after denaturing the DNA-DNA or DNA-PNA duplex structures in DI water at 70 or 95 °C for 30 seconds. After denaturing, the DNA/PNA probes remained active for the next hybridization event, while the target molecules were unbound from the probes. The PSi waveguide sensors can be reused at least five times and maintain stability and reproducibility of the sensing results. Ultimately, the lifetime of these passivated PSi sensors is likely to be limited by activity retention of probe DNA/PNA molecules as well as degradation of both silane molecules and the PSi network that may occur upon repeated usage of the sensors.

2.10 Summary

Charge density and surface passivation of PSi play significant roles in the accuracy, sensitivity and stability of PSi based biosensors. When the amount of negative charges immobilized in the PSi matrix increases, the polarization of silicon bonds on the PSi surface is enhanced, facilitating nucleophilic attack of silicon atoms by water molecules. This corrosion process is highly charge-dependent, as both increased DNA probe density and increased DNA target concentration led to a blueshift of the waveguide resonance angle. Corrosion can be partially mitigated by replacing the DNA probe with charge neutral PNA or fully mitigated by additionally introducing Mg^{2+} ions to shield negative charges on the target DNA backbone during hybridization to the PNA probes. Through these methods, the signal ambiguity for PSi based DNA sensing can be overcome and repeatable DNA sensing results can be achieved. PSi waveguide biosensors in this study were reused at least five times without sacrificing sensitivity or specificity.

CHAPTER 3
COMPUTATIONAL ANALYSIS OF CLOSED-ENDED AND OPEN-ENDED
POROUS SENSORS

3.1 Introduction

In recent years, porous materials have attracted a great deal of interest in research fields such as energy conversion [178,179], drug delivery [180,181], and medical diagnostics [182,183] due to their large internal surface area and tunable pore size distributions. Open-ended pores present in porous membranes are widely used in micro-fuel cells as gas diffusion layers and proton exchange membranes [184,185], and many studies have been carried out to investigate the mass transport properties of porous membranes in fuel cell applications [186,187]. Similarly, the out-diffusion of drugs from porous particles has been investigated [188,189]. However, in biosensing applications, the use of open-ended porous membranes is not common and has not been widely studied. Most biosensing approaches that incorporate microfluidic systems utilize closed-ended pores due to an ease of fabrication, and thus rely only on diffusive transport of analytes in solution to the inner pore sensing surfaces [140,190,191]. In this flow-over configuration, the diffusive flux into each individual pore can be as slow as a few molecules per second for molecules whose size approaches that of the pore opening. In this configuration, the majority of the molecules of interest are swept through the microfluidic channel and past the sensor without interacting with the inner pore sensing surfaces [144,145].

Open-ended porous membranes [27,192,193] and nanohole arrays [153,154,194] offer the possibility to overcome inefficient mass transport and achieve fast sensor response by allowing analytes to flow through the pores and interact more favorably with their inner surfaces. Despite

these advantages, implementing flow-through sensing requires many important design considerations and it is necessary to determine the kinetic conditions under which an open-ended, flow-through porous membrane offers advantages over simpler, closed-ended, flow-over porous sensors. In this chapter, the benefits of using open-ended PSi membranes for flow-through sensing as compared to closed-ended PSi films in the flow-over scheme are quantified by theoretically evaluating the relevant transport and reaction influences in open-ended and closed-ended pores, as reported in Ref. [149,150]. The effects of flow velocity, bulk analyte concentration, analyte diffusivity, and adsorption kinetics on sensor response are simulated using finite element methods and compared between the two different flow schemes. The analysis shows that open-ended pores enable analyte flow through the pores and greatly reduce the response time and analyte consumption for detecting large molecules with slow diffusivities compared with closed-ended pores for which analytes largely flow over the pores. We note that the computational analysis is not limited to PSi, but can be more broadly applied to evaluate the analyte transport and time response of other material systems comprised of nanopores.

3.2 Analytical Calculation of Analyte Transport Efficiency

In order to determine the analyte delivery efficiency in flow-over and flow-through porous sensing systems, the characteristic parameters to define the performance of both systems were calculated and evaluated. These calculations are based on the analytical solution of surface-based biosensors by Squires *et al.* [195].

For the flow-over model, the PSi sensor was considered as a flat square with width $w = 1$ mm, length $l = 1$ mm and average pore diameter $d = 25$ nm, being placed in a micro-channel of height $H = 60$ μm and width $W = 2$ mm. The sensor is modeled as an array of circular sensing

spots on a flat surface, as shown in Figure 3.1a. For simplicity, each spot represents the entry in a pore. The density of binding sites on the porous surface is $b_0 = 1 \times 10^{16}$ sites/m². A solution of analyte with concentration $c = 1$ μ M, and diffusivity $D = 10$ μ m² s⁻¹ is assumed to flow at rate $Q = 2$ μ L/min. An association constant of $k_a = 1 \times 10^4$ m³ mol⁻¹ s⁻¹ was used to represent high affinity binding reactions.

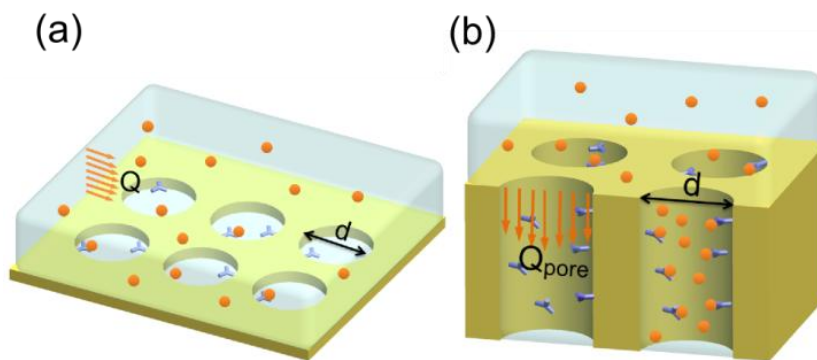


Figure 3.1. Schematic illustration of the models for (a) flow-over and (b) flow-through porous sensing systems. Binding sites are represented by blue probes in the porous regions, and target analyte molecules in the contacting solution are represented by orange spheres. Reprinted with permission from Ref. [149]. Copyright 2016 American Chemical Society.

For these conditions, the depletion zone thickness (δ) was estimated by

$$\delta \sim \frac{DHW}{Q} = 36 \text{ nm} \quad (3.2)$$

The Peclet number (P_e), defined as the ratio of the time for molecules to reach the sensing surface by diffusion over convection, was calculated by

$$P_e \equiv \frac{\text{convective transportation}}{\text{diffusive transportation}} \sim \frac{Q/W}{D} = 1700 \gg 1 \quad (3.3)$$

The Peclet number describes the size of the depletion zone relative to the microfluidic channel. Within the depletion zone, the concentration of analyte solution is extremely low, while in regions away from the depletion zone, the analyte solution is increasingly concentrated. At sufficiently low Peclet numbers, the depletion zone extends far into the channel and all target molecules entering the channel would be collected by the sensor. In the flow-over model, the Peclet number in the channel is calculated to be 1700. This large Peclet number means that the depletion zone is much thinner than the channel height and that most of the supplied analyte is swept downstream through the channel instead of diffusing into the pores of the sensor.

We also calculate a shear Peclet number for the flow-over model, which considers analyte transport within a thin layer near the sensor surface, where the flow may be approximated by a linear shear flow [196]. This number, depending on shear rate and sensor length, determines the size of depletion zone relative to the sensor length, and can be calculated by

$$P_{e_s} = 6 \left(\frac{l}{H} \right)^2 P_e = 2.8 \times 10^6 \quad (3.4)$$

The large value of the shear Peclet number indicates that the depletion zone extends in the channel well beyond the length of the sensor. Together, these two Peclet numbers indicate that the sensor operates in a diffusion-limited regime, where most target molecules are swept downstream before they can diffuse into the sensor pores.

For large P_{e_s} , the dimensionless mass transport flux (F) delivered to the sensor surface can be obtained by

$$F(P_{e_s} \gg 1) \approx 0.81 P_{e_s}^{1/3} = 1.47 \left(\frac{l^2 Q}{DWH^2} \right)^{1/3} = 114 \quad (3.5)$$

F varies weakly with flow rate (Q) in this limit such that the flow rate must increase 1,000-fold to enhance the mass transport flux by a factor of 10. The dimensional flux (J_D), or the number of analytes transported to the sensor per area per second was obtained via

$$J_D = DcwF = 6.86 \times 10^8 \text{ molecules/s} \sim 1.1 \text{ molecules/pore} \cdot \text{s} \quad (3.6)$$

meaning that only one analyte can be delivered to an individual pore every second by mass transport. This number represents an upper limit on analyte collection by mass transport and may be lowered by binding kinetics.

The Damkohler number (Da) is defined as the ratio of reactive to diffusive flux, and was calculated by

$$Da_{(flow-over)} = \frac{k_a b_0 l}{DF} = 146 \quad (3.7)$$

If the Damkohler number is much smaller than 1, mass transport supplies target molecules faster than reactions can consume them; thus, the chemical reaction is the rate limiting step. In contrast, if the Damkohler number is much larger than 1, the rate that analytes reach the sensing surface is slower than the possible reaction rate; hence, mass transport is rate limiting. The Damkohler number in the flow-over model is calculated to be 146, indicating that the flow-over PSi biosensor operates in the diffusion-limited regime, in which the binding reactions occur rapidly but the mass transport of analyte to the binding sites is slow.

Next, we consider a similar analysis of an open-ended porous sensor operating in the flow-through scheme, where the channel geometries, PSi parameters, fluidic parameters, and reaction constants are the same as for the flow-over model. This flow-through system can be modeled as an array of infinite columnar holes of diameter $d = 25$ nm and height $h = 4$ μm , being placed between two channels where the analyte solutions pass through the nanopores (Figure 3.1b). The

number of pores on the sensor is approximately $N \approx 1 \times 10^9$, yielding a flow rate through each pore of $Q_{pore} = Q/N = 0.033 \mu\text{m}^3/\text{s}$. For simplicity, the sensing area comprises the area enclosed by the inner sidewalls of the pore; any exterior surfaces that could contain binding sites are ignored.

The Peclet number within an individual pore (P_{epore}) for the flow-through scheme was calculated as

$$P_{epore} = \frac{Q_{pore}/d}{D} = 0.133 \quad (3.8)$$

This value indicates that mass transport is influenced by both convection and diffusion. The lower value of the Peclet number for the flow-through model implies that more analyte will reach the inner pore walls than for the flow-over model. As a result, the analyte concentration would show little variation laterally in the pore.

The shear Peclet number for an individual pore (P_{espore}) is given by

$$P_{espore} = 6 \left(\frac{h}{d}\right)^2 P_{epore} = 20,000 \gg 1 \quad (3.9)$$

This shear Peclet number indicates that analyte depletion extends well beyond the length of the pores. Under the condition ($P_{espore} \gg 1$), the mass transport flux (F_{pore}) was determined by

$$F_{pore}(P_{espore} \gg 1) \approx 0.81 P_{es}^{1/3} \approx 22 \quad (3.9)$$

The number of analytes transported to each individual pore per second (J_{pore}) was obtained by

$$J_{pore} = DcdF_{pore} \approx 3350 \text{ molecules/pore} \cdot \text{s} \quad (3.10)$$

This analyte transport flux is more than three orders of magnitude greater than in the flow-over scheme. The Damkohler number in the flow-through case was calculated as

$$Da_{(flow-through)} = \frac{k_a b_0 h}{DF_{pore}} \approx 3 \quad (3.11)$$

meaning that the sensor operates in a regime that is neither reaction-limited nor diffusion-limited.

The above figure-of-merit calculations offer broad estimates of the sensing performance for these two geometries, suggesting that the flow-through scheme overcomes the mass transport limitations experienced in flow-over sensors and enables efficient analyte delivery to the sensor surface. These comparisons are supported and extended with the COMSOL simulations presented in the following sections.

3.3 Numerical Model and Simulation

The transport and adsorption kinetics of both the flow-over (i.e., closed-ended pores) and flow-through (i.e., open-ended pores) schemes were simulated using the finite element method software COMSOL Multiphysics (v 4.2). To simplify the model employed in the simulations, variations in analyte concentrations across the width of the flow cells were neglected, reducing the 3D geometry to 2D. In addition, because the molecular binding kinetics in the pores are not affected by the microfluidic channel length, the simulated length of the microfluidic channel was reduced to 100 μm in the flow-over scheme and 60 μm in the flow-through scheme.

The following parameters were used in the COMSOL simulations: inlet velocity $u_0 = 10^{-6} - 10^{-2}$ m/s, reference pressure $p_{ref} = 1$ atm, analyte concentration in bulk flow $c_0 = 10^{-4} - 10^{-3}$ mol/m³, diffusivity $D = 10^{-11} - 10^{-9}$ m²/s, adsorption rate constant $k_a = 10^2 - 10^4$ m³/mol·s, desorption rate constant $k_d = 1 \times 10^{-6}$ s⁻¹, concentration of adsorption sites at the sensing surface $b_0 = 1 \times 10^{-7}$ mol/m², number of pores = 500, and lateral extent of porous region $w = 15$ μm . The pore geometry used in the simulations was chosen to approximate the PSi sensors: pore diameter = 25 nm, pore separation = 5 nm, and pore depth $h = 4$ μm . The flow cell dimensions are height $H = 60$ μm and channel length $L = 100$ μm in the flow-over scheme with closed-ended pores,

and $H = 60 \text{ }\mu\text{m}$ and $L = 60 \text{ }\mu\text{m}$ in the flow-through scheme with open-ended pores. Water is considered as the medium inside the flow cell along with the molecules under test, density $\rho = 1000 \text{ kg/m}^3$ and dynamic viscosity $\mu = 8.9 \times 10^{-4} \text{ Pa}\cdot\text{s}$. The models are meshed using triangular elements with refined mesh sizes in the porous area; the maximum element size is 10 nm and the minimum element size is 0.9 Å.

The Reynolds number (R_e), defined as the ratio of inertial forces to viscous forces within a fluid, was calculated by

$$R_e = \frac{\rho u L}{\mu} < 1.12 \quad (3.12)$$

where ρ is fluid density, u is flow velocity, L is channel length, and μ is dynamic viscosity. For low Reynolds numbers ($R_e < 2000$), the behavior of fluid depends mostly on its viscosity and the flow is steady, or laminar. For high Reynolds numbers ($R_e > 4000$), the momentum of the fluid determines its behavior more than the viscosity and the flow is unsteady, or turbulent. The Reynolds number calculated from the parameters used in the simulation is lower than 1.12. Therefore, laminar flow is used in the simulation to obtain the steady state velocity distribution.

The simulation was divided into three parts. First, the steady-state velocity distribution in the flow cell was obtained for laminar flow. Second, analyte concentrations were calculated by solving both the convection and diffusion equations to determine the analyte transport efficiency. Finally, surface binding kinetics were obtained by combining the binding reactions with analyte transport at the sensor surface.

The analyte solution with a concentration c_0 enters the microfluidic channel from the left inlet at a flow rate u_0 . The steady state velocity profile was obtained by solving Navier-Stokes equation in a 2D model as given by eq 3.13,

$$\rho \frac{\partial \mathbf{u}}{\partial t} + \rho(\mathbf{u} \cdot \nabla)\mathbf{u} = \nabla \cdot (-p + \mu \cdot \nabla \mathbf{u}) \quad (3.13)$$

where ρ is fluid density, u is flow velocity, p is pressure, and μ is dynamic viscosity. The boundary conditions for the pressure-driven flow were:

$$\text{Inlet: } u = u_0$$

$$\text{Outlet: } p = p_{ref} = 1 \text{ atm}$$

$$\text{Other boundaries: } u = 0$$

Analyte transport was described by the diffusion equation in eq 3.14,

$$\frac{\partial c}{\partial t} + \nabla \cdot (-D\nabla c + c\mathbf{u}) = 0 \quad (3.14)$$

where c is the analyte concentration in bulk phase, D is the diffusivity of analyte, and u is the flow velocity calculated previously. The initial condition sets the concentration in the bulk at $t = 0$ to be $c = c_0$.

The binding reaction between analytes and bioreceptors immobilized at the sensor surface was described by eq 3.15,



where A represents bulk analyte species whose concentration is c , B represents active binding sites whose concentration is b , and $A \cdot B$ represents the bound species on the sensor surface with a concentration of c_s . The association and dissociation rate constants are k_a and k_d , respectively.

The concentration of active binding sites b , is the difference between the initial concentration of binding sites b_0 at sensor surface and the number of sites already occupied by the complexes.

Therefore, eq 3.15 can be written as

$$\frac{\partial c_s}{\partial t} = k_a c(b_0 - c_s) - k_d c_s \quad (3.10)$$

Eq 3.16 is the boundary condition at the sensing surface. It contains the bulk concentration c , and thus must be solved together with eq 3.14. The other boundary conditions are:

$$\text{Inlet: } c = c_0$$

$$\text{Outlet: No diffusive transport, } \nabla \cdot (-D\nabla c + \mathbf{c}\mathbf{u}) = \nabla \cdot \mathbf{c}\mathbf{u}$$

$$\text{Non-PSi surface: No flux, } \nabla \cdot (-D\nabla c + \mathbf{c}\mathbf{u}) = 0$$

Porous geometries containing different numbers of pores were simulated. Figure 3.2 shows the simulated equilibrium time of the flow-over porous sensor as a function of the number of pores when analyte diffusivity $D = 1 \times 10^{-11} \text{ m}^2/\text{s}$, analyte concentration in bulk flow $c_0 = 1 \text{ } \mu\text{M}$, and inlet flow velocity $u_0 = 5 \times 10^{-5} \text{ m/s}$. The equilibrium time, which will be discussed in detail in the following sections, is defined as the time when the sensor response reaches saturation. Increasing the number of simulated pores leads to longer equilibrium times, with a saturation in this effect beginning when the number of simulated pores is greater than approximately 500. Therefore, the PSi structure was represented by 500 pores throughout this thesis. As shown in Figure 3.3, the simulated pores have uniform pore diameter of 25 nm, pore depth of 4 μm , and center to center pore spacing of 30 nm. In the flow-over scheme, the microfluidic channels were scaled down to 60 μm in height and 100 μm in length. In the flow-through scheme, the channels were scaled down to 60 μm in height and 60 μm in length.

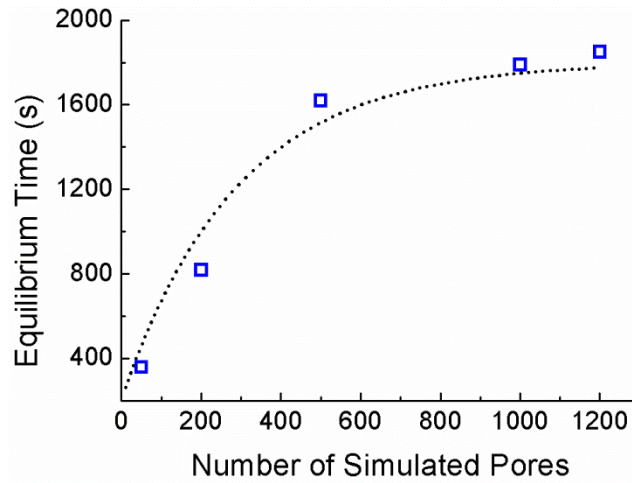


Figure 3.2. Simulated equilibrium time of the flow-over porous sensor consisted of 50 pores, 200 pores, 500 pores, 1000 pores, and 1200 pores. The dotted line is shown as a guide to the eye.

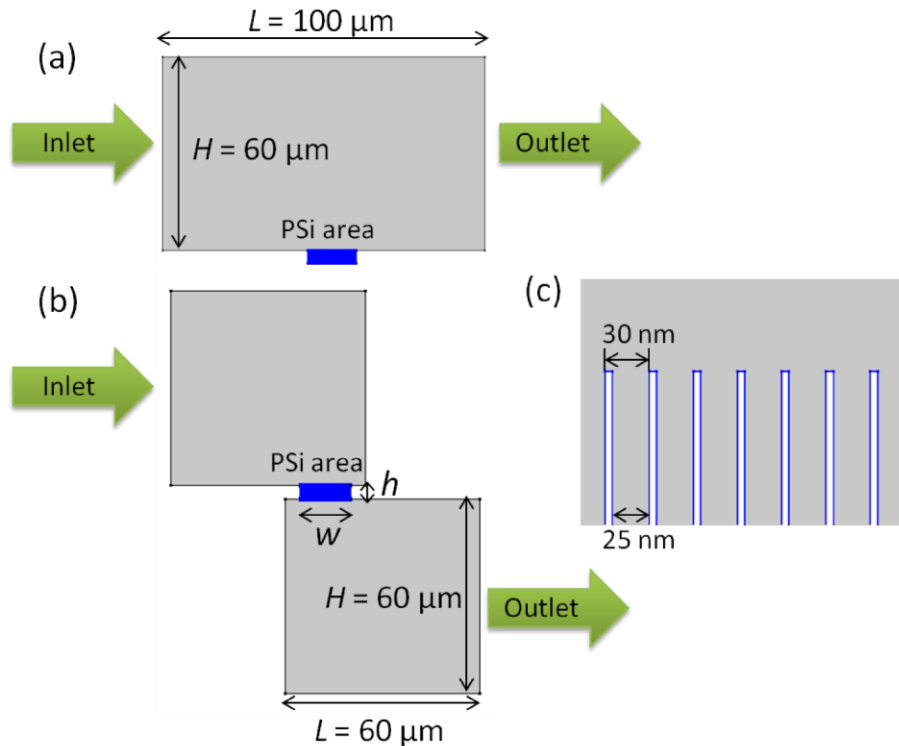


Figure 3.3. Schematic of the flow cell-integrated PSi sensor used in COMSOL simulations. (a) Schematic of a closed-ended PSi membrane in a flow-over operation mode. The flow cell dimensions are $L = 100 \mu\text{m}$ and $H = 60 \mu\text{m}$. The start of the porous region is located $50 \mu\text{m}$ away

from the inlet. (b) Schematic of an open-ended PSi membrane in a flow-through operation mode. The flow cell dimensions used for the upper and bottom channels are $L = H = 60 \mu\text{m}$. The start of the porous region is located $40 \mu\text{m}$ away from the inlet. Eq 3.16 applies to the blue highlighted PSi area as the boundary condition. (c) Zoom-in of the PSi area showing equally spaced pores with pore diameter = 25 nm and period = 30 nm . The computational space comprises 500 pores along a distance $w = 15 \mu\text{m}$ and a height $h = 4 \mu\text{m}$.

3.4 Simulated Transport and Reaction Kinetics

3.4.1 Velocity Distribution and Analyte Concentration Distribution

The simulated velocity distribution and analyte concentration distribution for the flow-over scheme are shown in Figure 3.4a. The flow direction is represented by the arrows and the flow rate is represented by the arrow length. The convective flow is fastest in the center of the channel and slowest at the channel edges. The concentration distribution shows that a depletion zone forms near the PSi sensing region. As a result, most analytes flow through the micro-channel without reaching or interacting with the PSi surface. In contrast, in the flow-through scheme shown in Figure 3.4b, analyte is guided toward the PSi sensing region. From the velocity distribution plot for the flow-through scheme, convective flow is strong in each pore, which provides analyte transport to receptors immobilized along the pore walls. The enhanced analyte transport in the flow-through scheme is further confirmed by the lack of lateral variations in the concentration distribution plot, which is in agreement with the analytical calculations in Section 3.2 that the analyte concentration would show little variation laterally in the pore under the flow-through scheme. No depletion zone is present laterally in the porous region and the concentration of analyte in the solution decreases progressively along the depth of the pores.

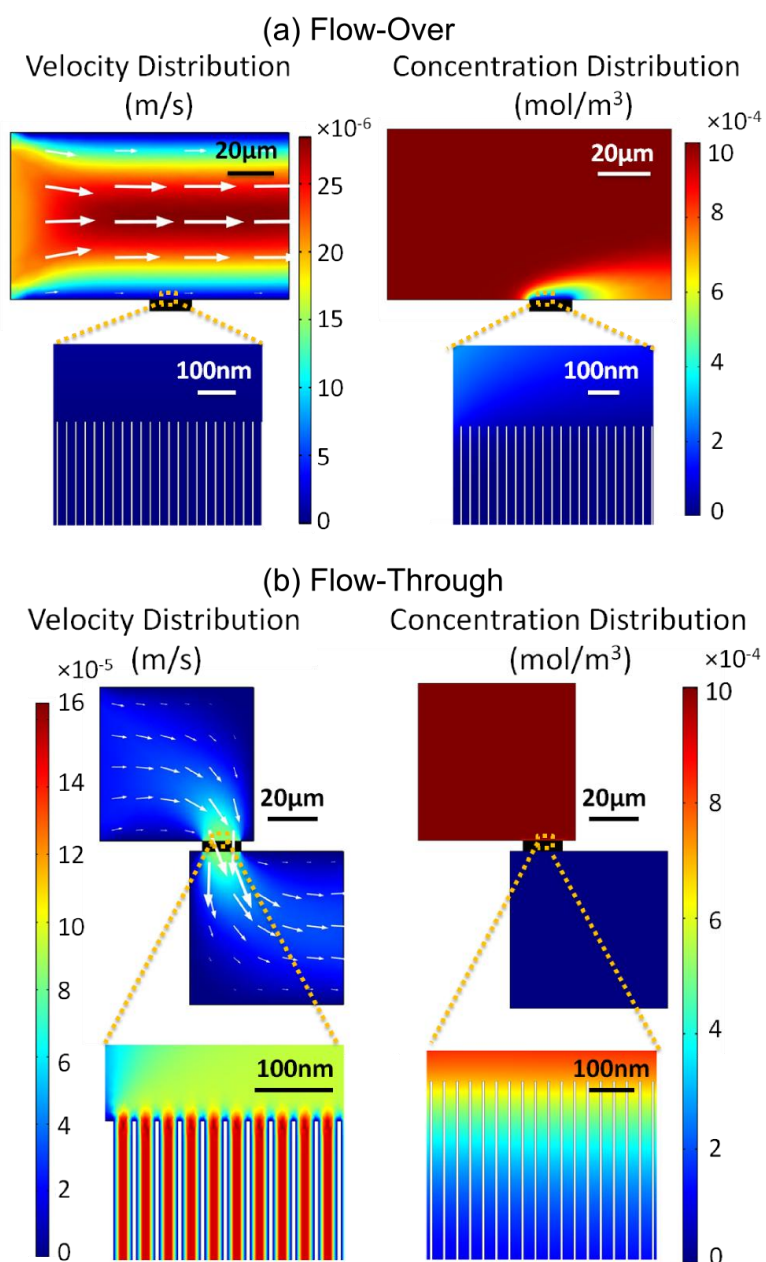
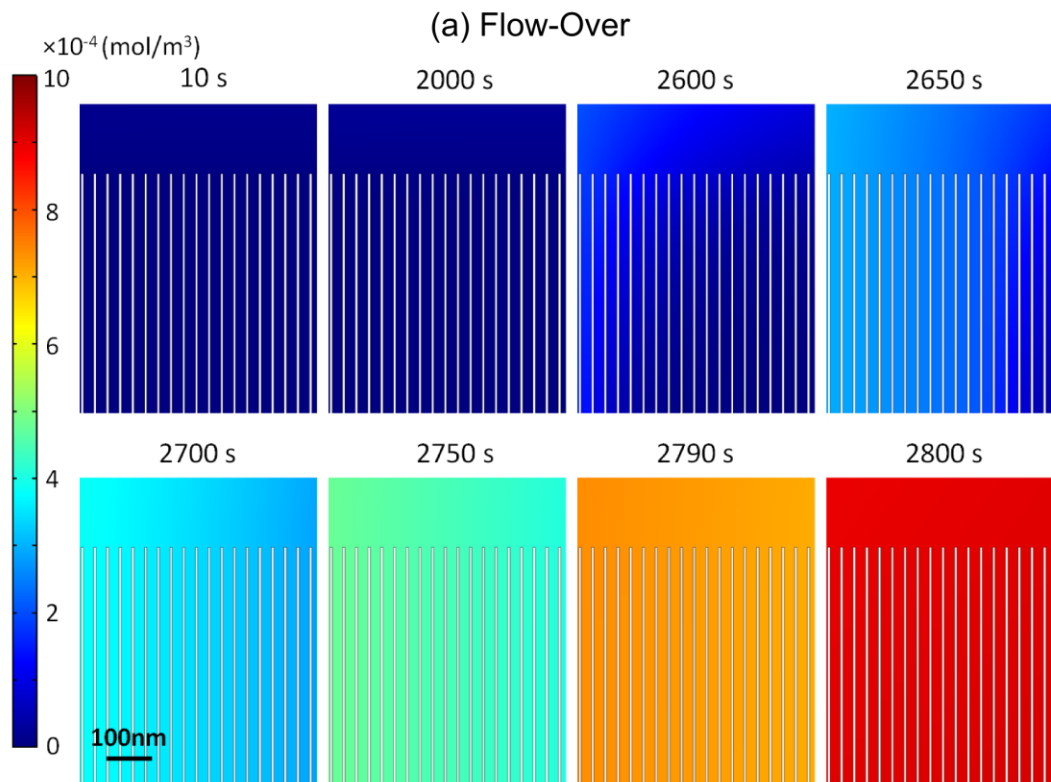


Figure 3.4. (a) Velocity distribution and analyte concentration distribution at 180 s into the simulation for the flow-over scheme. In the velocity distribution plot, the color bar indicates the flow rate of the solution. Zoom-in image shows the flow rate around the pores. In the concentration distribution plot, the color bar indicates the concentration gradients of analytes in solution. Zoom-in image shows that most analytes do not reach the PSi sensing area due to the

formation of the depletion zone. (b) Velocity and concentration distributions at 180 s into the simulation for the flow-through scheme. Zoom-in image of the velocity distribution shows rapid flow through the pores. Zoom-in image of the concentration distribution confirms that the analyte is transported into the PSi sensing region. Reprinted with permission from Ref. [149]. Copyright 2016 American Chemical Society.

As time increases, the concentration of analyte increases at each position along the pore as binding sites become saturated. Figure 3.5 shows these simulated concentration distributions for both the flow-through and flow-over schemes at different times. For the flow-over scheme, the concentration distribution varies laterally. For the flow-through scheme, the concentration of analyte solution increases progressively along the depth of pores as time increases.



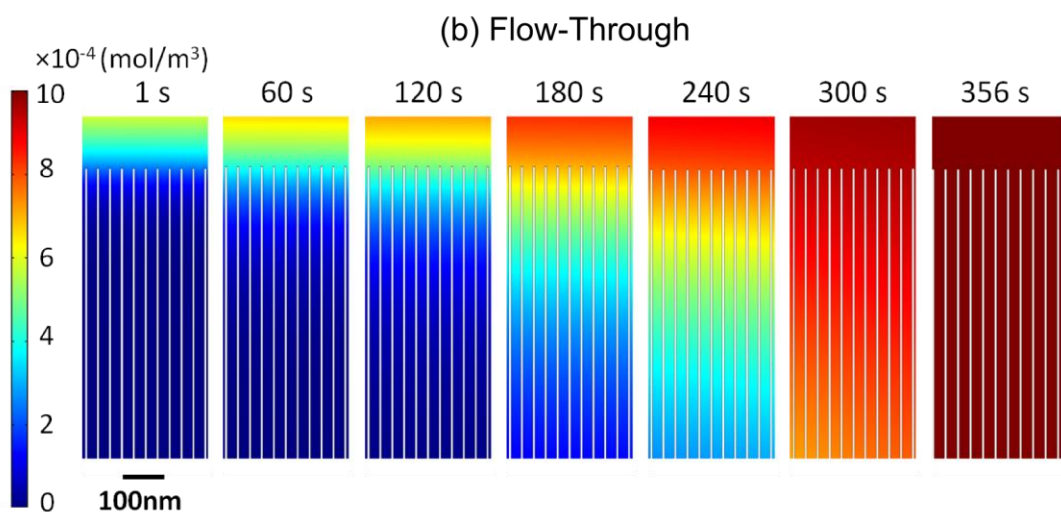


Figure 3.5. Analyte concentration distributions in the porous region at different times for (a) the flow-over and (b) the flow-through scheme. The illustrated pores represent those from the center of the simulated porous region.

The amount of analyte captured on the porous surface as a function of time was calculated to estimate the sensor equilibrium time for both flow geometries. The equilibrium time was estimated to be the time required to reach a surface coverage with $< 0.01\%$ variance of its saturation value, which can be considered as the time when all available sites on the sensor surface have been occupied by analytes and the sensing signal reaches plateau. In practice, the response time for a sensor would be governed by the minimum detectable signal change and therefore could be significantly shorter than the equilibrium time defined here. Figure 3.6 shows the average surface concentration of analytes bound to the pore walls as a function of time for both flow schemes when analyte diffusivity $D = 1 \times 10^{-11} \text{ m}^2/\text{s}$, analyte concentration in bulk flow $c_0 = 1 \text{ } \mu\text{M}$, and inlet flow velocity $u_0 = 2 \times 10^{-5} \text{ m/s}$. The equilibrium time for the flow-

through scheme is 356 s, which is approximately 8 times faster than the response time (2800 s) for the flow-over scheme.

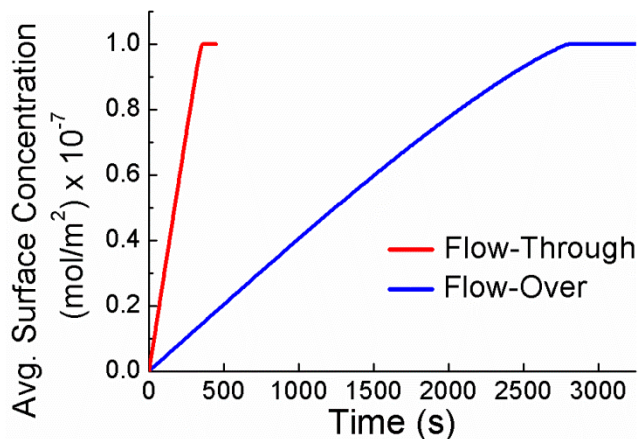


Figure 3.6. Simulated average surface concentration of analytes that were captured by flow-over and flow-through porous sensors as a function of time. Reprinted with permission from Ref. [149]. Copyright 2016 American Chemical Society.

3.4.2 Influence of Flow Velocity

Numerical simulations under different flow velocities were performed in order to study and compare the efficiency of analyte transport in flow-through porous sensors with open-ended pores and flow-over porous sensors with closed-ended pores. Figure 3.7 shows the equilibrium time of closed-ended and open-ended porous sensors in their respective flow schemes as a function of the flow velocity when analyte diffusivity $D = 1 \times 10^{-11} \text{ m}^2/\text{s}$, which is representative of large protein molecules [197,198], and a bulk analyte concentration is of $c_0 = 1 \text{ } \mu\text{M}$. The flow velocity is given in dimensional form by multiplying the input velocity specified earlier for the COMSOL simulation by the channel height of $60 \text{ } \mu\text{m}$ and width of 2 mm . To focus on the role of transport, rapid adsorption kinetics with $k_a = 1 \times 10^4 \text{ m}^3 \text{ mol}^{-1} \text{ s}^{-1}$ and $k_d = 1 \times 10^{-6} \text{ s}^{-1}$ were applied so that analytes adsorb to the sensor surface immediately.

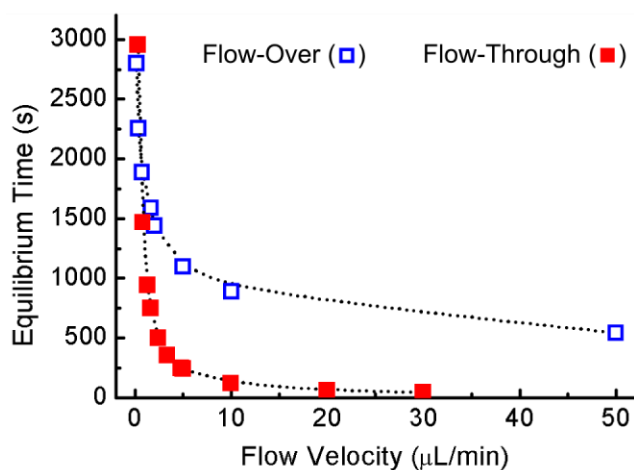


Figure 3.7. Equilibrium time of both flow schemes as a function of the flow velocity. Analyte concentration = 1 μM . Reprinted with permission from Ref. [150]. Copyright 2016 Springer.

As shown in Figure 3.7, when there is no flow (e.g., flow velocity = 0 $\mu\text{L}/\text{min}$), both flow schemes represent stagnant analyte solutions, where the replenishment of consumed analyte near the sensor surface relies only on diffusion. Likewise, at low flow velocities (< 1 $\mu\text{L}/\text{min}$), both flow schemes operate in a diffusion-limited regime resulting in similarly long equilibrium times. The equilibrium time shortens when flow velocity increases due to enhanced mass transport. However, at flow velocities greater than 10 $\mu\text{L}/\text{min}$, further increases in the flow velocity become less effective for both flow schemes because the sensor response approaches the reaction-limited regime where mass transport supplies analyte quicker than the sensor can adsorb them. At flow velocities between 2 and 10 $\mu\text{L}/\text{min}$ in which both flow schemes are neither reaction-limited nor diffusion-limited, the equilibrium time is reduced at least 5-fold by employing the flow-through scheme with open-ended pores.

While increasing the flow rate reduces the response time for porous sensors, the amount of analyte consumed must be considered. In biosensing applications when sample availability is

limited, minimizing the total analyte volume consumed is especially important. Figure 3.8 shows the total volume of analyte solution required for both flow schemes to achieve their equilibrium response for different flow velocities. Analyte diffusivity, concentration, and rate constants were the same in Figure 3.8 as in Figure 3.7. The volume of analyte consumed was calculated by multiplying the dimensional flow velocity by the equilibrium time. The total required volume of analyte solution in the flow-over scheme with closed-ended pores increases rapidly in response to the increases in flow velocity as most of the analyte molecules flow past the sensor region without entering the pores. However, in the flow-through scheme with open-ended pores, the required volume of analyte changes little with flow velocity. This result can be explained by recalling the assumption of rapid adsorption kinetics used in the simulation and considering that the flow-through configuration forces all analytes to pass through the nanopores in close proximity to the pore walls. Accordingly, the flow-through scheme is particularly favorable for porous sensors as it facilitates rapid response time and a reduced analyte volume.

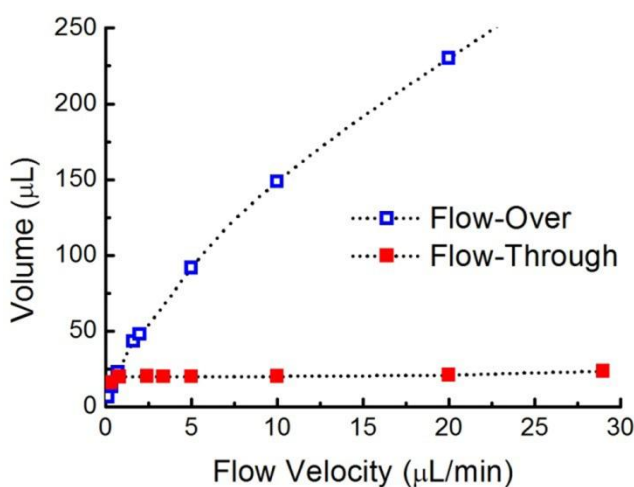


Figure 3.8. Total volume of analyte solution required in closed-ended, flow-over porous sensors and open-ended, flow-through porous sensors to reach equilibrium at different flow velocities.

Analyte concentration = 1 μM . Reprinted with permission from Ref. [150]. Copyright 2016 Springer.

3.4.3 Influence of Analyte Concentration

Next, we evaluate how the bulk concentration of analyte in the micro-channel affects analyte transport in both flow schemes. Figure 3.9 shows the simulated equilibrium time at different target analyte concentrations ranging from 0.1 to 5 μM with a fixed flow velocity of 5 $\mu\text{L}/\text{min}$. The same analyte diffusivity and rate constants were used in Figure 3.9 as in Figures 3.7 and 3.8. In both flow schemes, analyte at a lower bulk concentration of 0.1 μM requires approximately 50 times longer to reach equilibrium than analyte at a higher concentration of 5 μM . In agreement with the assumption of first-order Langmuir kinetics [195], at a sufficiently low desorption rate constant, the equilibrium time in both flow schemes is inversely proportional to the analyte concentration, as shown in Figure 3.8. We note that although the flow-through configuration with open-ended pores maintains approximately 5-fold improvement in equilibrium time throughout the simulated concentration range, the impact on time saving by the flow-through scheme is stronger for analyte at lower bulk concentrations. At a low analyte concentration of 0.1 μM , the equilibrium time is reduced from approximately 3 h to 40 min by replacing closed-ended, flow-over porous sensors with open-ended, flow-through porous sensors. For analytes at a higher concentration of 5 μM , although the same improvement ratio is achieved, the open-ended sensors only reduce the equilibrium time by less than 3 min. Thus, the flow-through sensing approach is especially advantageous for providing more reasonable sensor response times when detecting dilute samples.

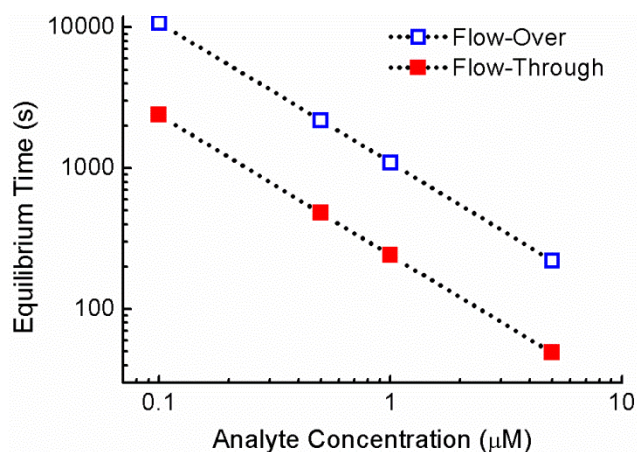


Figure 3.9. Effect of analyte concentration on equilibrium time. Flow velocity = 5 $\mu\text{L}/\text{min}$. The equilibrium times of flow-over sensors with closed-ended pores and flow-through sensors with open-ended pores show an inverse dependence on analyte concentration. Reprinted with permission from Ref. [150]. Copyright 2016 Springer.

3.4.4 Influence of Analyte Diffusivity and Adsorption Rate

Analyte size plays an important role in their transport within porous matrices. Larger molecules have slower diffusivities; for instance, the diffusion constant for the protein bovine serum albumin (69 kDa) in an aqueous solution is approximately $1 \times 10^{-11} \text{ m}^2/\text{s}$ [197], while those for small ions and for ethanol in water are around $10^{-9} \text{ m}^2/\text{s}$ [199]. The transport of large molecules within porous materials is slower than in bulk solution due to hindered diffusion in nanoscale pores. As a result, molecular diffusivities in nanopores depend not only on the nature of the molecules themselves, but also on the geometry and morphology of the porous materials [200,201]. The equilibrium times for porous sensors having closed-ended pores in the flow-over scheme and open-ended pores in the flow-through scheme was investigated for analytes with different diffusivities and adsorption kinetics. Adsorption rate constants of $k_a > 10^2 \text{ m}^3/\text{mol}\cdot\text{s}$ are typical for most molecular adsorption events, we consider adsorption rate constants between 10^2

- $10^4 \text{ m}^3/\text{mol}\cdot\text{s}$ in our model. For these conditions, Figure 3.10 shows that the equilibrium time is reduced with faster adsorption kinetics and diffusivities. Similar to the impact of porous structures on molecular diffusivities, the effective adsorption rate in nanoscale pores can be 10^2 - 10^4 times smaller than the adsorption rate on flat surfaces due to mass transport limitations [141,202]. Moreover, adsorptions with large rate constants are more significantly affected in nanoporous regions compared to adsorptions with small rate constants [144], resulting in a reduced dynamic range of effective adsorption rate constants in porous sensing regions. Therefore, although Figure 3.9 considers a three order of magnitude difference in adsorption rate constant, this rate constant is the bulk one and the range of effective adsorption rate constants in the nanopores is smaller. Consequently, although the inverse dependence of equilibrium time on adsorption rate constant is clearly shown in Figure 3.10, as is expected from first-order Langmuir kinetics [195], the time to reach equilibrium does not show a strong dependence on the adsorption rate constant.

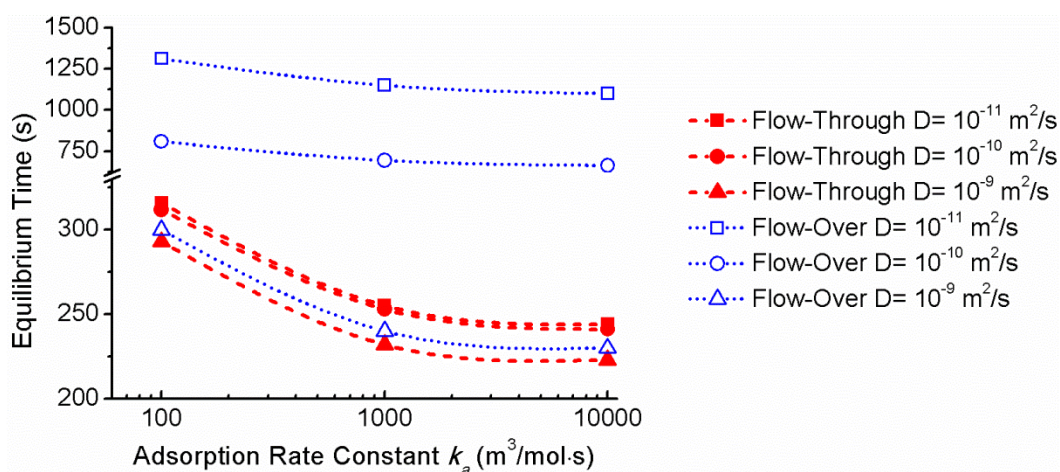


Figure 3.10. Equilibrium time of both flow schemes for analytes with different diffusivities D and adsorption rate constants k_a . Flow velocity= $5 \mu\text{L}/\text{min}$, and analyte concentration = $1 \mu\text{M}$. Reprinted with permission from Ref. [150]. Copyright 2016 Springer.

Examining the role of diffusivity, we find the benefit of the flow-through scheme with open-ended pores is less significant for small analytes (i.e., molecular weight < 1 kDa) with diffusivities on the order of 10^{-9} m²/s because their small molecular size provides relatively fast diffusive transport rate in both systems. For analytes with bulk diffusivities around 10^{-10} m²/s, the flow-through configuration provides less than 3-fold improvement in simulated equilibrium times compared to the flow-over scheme. When applied to larger analytes (i.e., molecular weight > 100 kDa) with slow diffusivities around 10^{-11} m²/s, the flow-through scheme shows an approximately 5 times faster equilibrium time than the flow-over scheme, which is consistent with the results in Figures 3.7 and 3.9. For those large analytes, the flow-through configuration offers significant benefit of enhancing the mass transport efficiency by providing convective transport of analytes through the open-ended pores. The enhanced convective transport of analytes in the open-ended pores causes the sensor response time to be less dependent on analyte diffusion rate; therefore, large molecules with low diffusivities reach equilibrium almost as rapidly as small molecules in the flow-through configuration.

In the above analysis, the 2D simulation space included 500 straight pores with uniform diameters of 25 nm in order to keep the computational time to manageable levels. Actual porous sensors contain many more pores and often with a complicated morphology. In the biosensing experiments detailed in the following chapter, the PSi sensors contain approximately 10^9 pores that alternate in layers of high and low porosity with slightly different average pore diameters. The increased amount of pores and the tortuosity in the PSi matrix impact both the diffusion and adsorption of molecules in the nanoscale pores. Therefore, the simulated results for open-ended and closed-ended porous sensors serve as a guide to estimate the relative trends of the performance for the flow-through and flow-over sensing formats. Because the results have a

strong dependence on the geometry and morphology of the porous matrix, the exact results from simulation cannot be compared directly with those obtained in experiments.

3.5 Summary

Efficient mass transport through porous networks is essential for achieving rapid response times in sensing applications utilizing porous materials. In this work, we theoretically demonstrate that open-ended porous membranes can overcome diffusion challenges experienced by closed-ended porous materials in a microfluidics environment. The analyte transport and equilibrium time of open-ended, flow-through porous membranes were investigated via finite element method simulations and compared to conventional closed-ended, flow-over porous sensors. The simulation results indicate that the flow-through scheme is most beneficial for facilitating the transport of large analytes with slow diffusivity throughout the nanoscale pores using modest flow velocities of 2-10 $\mu\text{L}/\text{min}$. Additionally, the flow-through scheme enables more reasonable response times for the detection of dilute analytes (concentration $< 1 \mu\text{M}$) and reduces the volume of solution required for analysis. Experimental confirmation of the simulation results was carried out with open- and closed-ended PSi microcavities, as presented in the following chapter.

CHAPTER 4

FLOW-THROUGH POROUS SILICON MEMBRANES FOR LABEL-FREE BIOSENSING

4.1 Introduction

Due to the high aspect ratio of PSi nanopores, the performance of closed-ended PSi sensors is limited by infiltration challenges and slow sensor response when detecting large molecules such as proteins and nucleic acids. As shown in Chapter 3, employing a flow-through scheme for porous sensors holds great promise for improving molecule transport efficiency and reducing sensor response time. Freestanding PSi membranes have been previously used for label-dependent chemical and bio-separations [25,203,204]. The most straightforward way to form open-ended PSi is to apply much higher currents at the end of the etching process to lift off the PSi film from the silicon substrate. A PSi membrane fabricated with open-ended pores by this approach was demonstrated to exhibit lower background signals from non-specific adsorptions compared to on-substrate PSi films having closed-ended pores [193]. However, for producing high quality optical structures in PSi biosensors, this lift-off process is hindered by low repeatability and incompatibility with the integration in on-chip sensor arrays. An alternative for constructing PSi membranes involves a pre-thinning of selected regions on a silicon substrate by wet or dry etching and subsequent anodization through the thinned areas. This approach has been used to form proton-conducting PSi membranes for fuel cell applications [205,206]; however, due to carrier depletion in the remaining silicon, the anodization rate in the last few microns of silicon wafer is significantly lower and thus the time required to etch through the whole silicon region can be as long as a few hours. Additionally, this approach suffers from yielding a vertical porosity gradient, and is therefore inadequate to produce high quality optical structures in PSi. In

order to achieve high-throughput production and enhance the quality and mechanical stability of membrane structures, we utilize photolithographic techniques to pattern electrochemically etched PSi and selectively create open-ended PSi membranes at a wafer scale. This approach is readily adaptable for integration in massively parallel microarrays.

In this chapter, the transport and binding kinetics in these PSi membranes were compared through experiments with those from closed-ended PSi films of comparable thickness in a conventional flow-over sensing scheme. A microcavity structure was incorporated into the membrane to enable highly sensitive label-free optical sensing. As discussed in Chapter 1, the microcavity consists of a pair of Bragg mirrors separated by a cavity layer deep within the structure. Although molecules are accessible to the entire porous structure, the sensor response is predominantly determined by the effective index change in the cavity layer. While the microcavity is among the most sensitive sensor platforms, the long required diffusion depth for molecules in high aspect ratio pores presents an infiltration challenge for molecules that are not significantly smaller than the pore diameter [150]. To illustrate this issue, we first experimentally evaluated the adsorption kinetics in flow-over vs. flow-through PSi microcavities upon exposure to analytes with different sizes [150]. Next, the sensing performance of the PSi microcavity in both flow schemes were evaluated by detecting the specific binding of streptavidin to biotinylated PSi films, as reported in Ref. [149]. Quantum dot (QD) based fluorescence measurements were carried out to verify the improved analyte transport efficiency within open-ended PSi membranes. Finally, the mechanical strength of the membranes was tested with a non-contact approach based on interferometric profilometry. The PSi microcavity membrane used in this work showed good mechanical stability and could easily withstand up to approximately 7 psi of differential pressure applied cross it.

4.2 Device Fabrication and Measurement

4.2.1 Electrochemical Etching of PSi Microcavities

Double side polished, *p*-type silicon wafers (<100>, 0.01-0.02 Ω cm, 500-550 μ m) were etched using an AMMT wafer-scale silicon etching system with an electrolyte containing 15% HF acid in ethanol. For etching, a closed-back wafer holder was used to prevent electrolyte contact with the rear side of the wafer. The microcavity consisted of a multilayer structure with alternating regions of high (H) and low (L) porosity. A configuration of (L H)⁹(H L)⁹ was etched at the front side of the wafer using a current density of 48 mA/cm² (80% porosity, H) and 20 mA/cm² (65% porosity, L). The anodization times were 6.1 and 4.5 s for H and L, respectively, to fabricate layers that have optical thicknesses designed to be one quarter of the resonance wavelength. Two high porosity sacrificial layers, etched at 48 mA/cm², were included at the top and bottom of the microcavity, which were necessary for the open-ended membranes to provide process tolerance during photolithography, but were also included in the closed-ended PSi sample for consistency. The top sacrificial layer was \sim 2 μ m thick and the bottom sacrificial layer was \sim 15 μ m thick. These thicknesses were not optimized. As detailed in the following section, the RIE Bosch process used to remove the silicon substrate and open the PSi membrane window etches away PSi rapidly; therefore, the bottom sacrificial layer was thicker than the top one to ensure that the PSi microcavity layers were not inadvertently etched away. After anodization, the PSi wafer samples were oxidized in air in a furnace at 500 $^{\circ}$ C for 5 min. SEM images were used to obtain approximate measurements of the pore diameters and layer thicknesses for these structures. The resulting microcavity was approximately 4 μ m thick, sandwiched between two sacrificial layers, with pore diameter of \sim 25 nm and layer thickness of

~125 nm in the high porosity layers and pore diameter of ~20 nm and layer thickness of ~105 nm in the low porosity layers.

4.2.2 Photolithography Process for PSi Membrane Fabrication

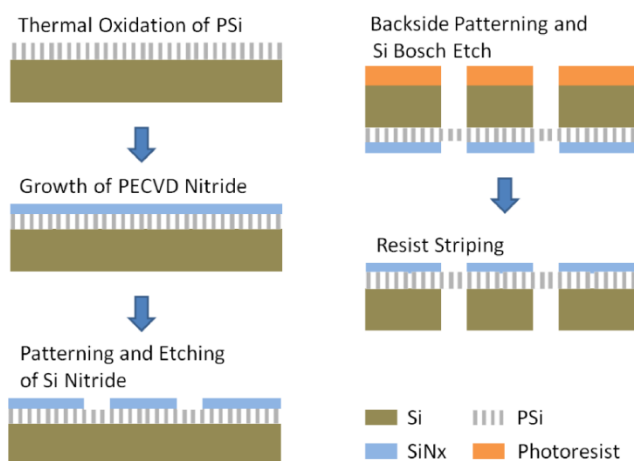


Figure 4.1. Process flow for PSi membrane fabrication.

Oxidized PSi wafer samples were lithographically patterned for membrane formation following the process flow in Figure 4.1. First, a 400 nm silicon nitride film was deposited on the PSi surface by plasma enhanced chemical vapor deposition (PECVD, Oxford Plasmalab System 100). The PSi wafers were then subjected to a photolithographic process in order to pattern the silicon nitride film and open up windows for analyte access to selected $1\text{ mm} \times 1\text{ mm}$ regions. The patterning process involved spin-coating the silicon nitride coated PSi wafers with MicroPrime P20 adhesion promoter (ShinEtsu MicroSi, Inc.) followed by deposition of a 2-3 μm thick layer of SPR 220 4.5 photoresist (Dow Chemical). The photoresist was soft baked at 115 $^{\circ}\text{C}$ for 90 s on a hotplate, exposed under 365 nm light for 15 s using a mask aligner (Quintel Mask and Contact Aligner), hard baked at 115 $^{\circ}\text{C}$ for 90 s on a hotplate, and then developed in CD-26 (Dow Chemical) for 1 min. Following pattern exposure and development, reactive ion

etching (RIE, Oxford Plasmalab 100) was used to etch away the exposed regions of silicon nitride with C_4F_8 gas. The remaining photoresist was subsequently removed upon exposure to acetone and multiple DI water rinse steps. An additional, aligned photolithography step was used to pattern the backside of the samples. The backside of the wafers were spin-coated with P20 adhesion promoter followed by a 7-8 μm thick layer of SPR 220 7.0 photoresist (Dow Chemical), soft baked at 115 °C for 90 s on a hotplate, and exposed under 365 nm light for 45 s using a mask aligner. The thick photoresist serves as an etch mask for deep silicon etching. The wafers were stored at room temperature for ~ 1 h before exposing them to a hard bake at 115 °C for 90 s, and then developed in CD-26. The ~ 1 h hold time between the exposure and post-exposure bake steps was necessary to allow water to diffuse back into the photoresist film and complete the photo-reaction. To form the defined silicon membrane regions, the exposed areas of the silicon surface were then etched using a RIE Bosch process with C_4F_8 and SF_6 gases. Following the RIE Bosch process, the samples were examined under an optical microscope to confirm the etching of the silicon substrate within the membrane regions and then the remaining photoresist was stripped away with acetone and isopropyl alcohol. The nitride film remaining on PSi ensures that analytes flow only into the membrane regions of the PSi films. The smooth surface of the nitride also facilitates the attachment of microfluidic channels, as discussed in the following section. For the fabrication of closed-ended PSi samples, a 400 nm silicon nitride film was first deposited on the surface of oxidized PSi wafer samples by PECVD. The same contact lithography and RIE was then used to pattern the silicon nitride film and open up windows on the top side of the samples. Figure 4.2 shows images of the fabricated PSi microcavity membrane. The total thickness of the resulting membrane was approximately 15 μm .

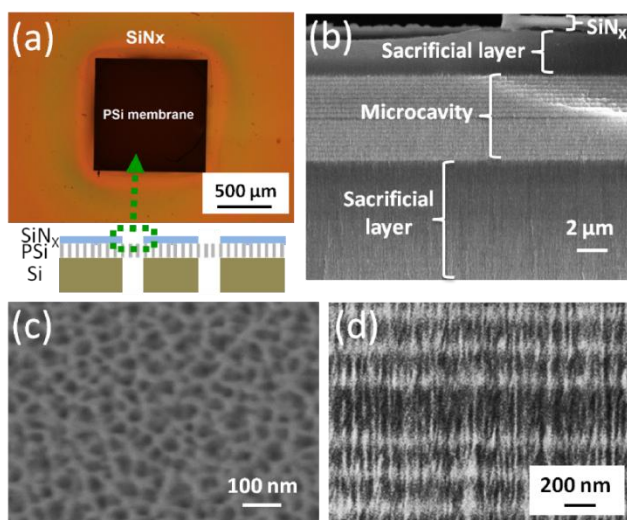


Figure 4.2. Images of a fabricated PSi membrane. (a) Optical microscope image and schematic illustration of PSi membrane surrounded by silicon nitride. (b) Cross-sectional SEM image of the edge of the membrane region showing the sacrificial layers, PSi layers comprising the microcavity, and the remaining silicon nitride film. (c) Top view SEM image of the PSi membrane region. (d) Magnified cross-sectional SEM image of the microcavity region showing the high quality of the interfaces. Reprinted with permission from Ref. [149]. Copyright 2016 American Chemical Society.

4.2.3 Microfluidics Integration

Polydimethylsiloxane (PDMS) microfluidic flow cells were attached to PSi samples to facilitate surface functionalization and real-time optical detection of target molecules. A Sylgard 184 silicone elastomer base and curing agent used to fabricate PDMS channels were purchased from Dow Corning. PDMS flow cells with dimensions of 7 mm × 2 mm × 60 μm were fabricated by standard soft lithography techniques as detailed in previous work [44]. Briefly, SU-8 micro-channels were patterned on a silicon wafer using standard photolithography. PDMS was then poured onto the SU-8 mold to obtain the patterned channel shell. The PDMS used in this

step was a mixture of pure PDMS and curing agent at a weight ratio of 10:1. After degassing in a vacuum chamber, the PDMS sample was cured in an oven for more than 4 hours at 65 °C. The cured PDMS replica was then cut out from the silicon wafer using a scalpel. Holes were punched at the end of each channel on the PDMS replicas using a 20 gauge punch. The surfaces of the PDMS flow cell and the patterned PSi were activated by a 30 s oxygen plasma treatment to create Si-OH groups, aligned under an optical microscope, and sealed together by keeping the two surfaces in contact for ~ 10 s without any external pressure. The PSi membrane samples were sealed on each side to a micro-channel. The upper channel contained the inlet for the analyte solution while the outlet was present in the bottom channel. Together, these two channels result in a flow path that forces the solution to pass through the open-ended pores. The closed-ended PSi samples were sealed onto a micro-channel containing both the inlet and outlet on the same side for a flow-over configuration. For all samples, metal pins (21 gauge) were inserted in the punched holes of the PDMS channels for the connection between the Tygon tubings and the PDMS shells. Analyte solutions were introduced to the Tygon tubing using syringe pumps. In order to avoid excessive pressure forces that could rupture the membranes, flow rates were kept under 15 $\mu\text{L}/\text{min}$ in the flow-through experiments, which is compatible with current microfluidic platforms [207]. Figure 4.3 shows images of the PSi membranes integrated with microfluidic channels.

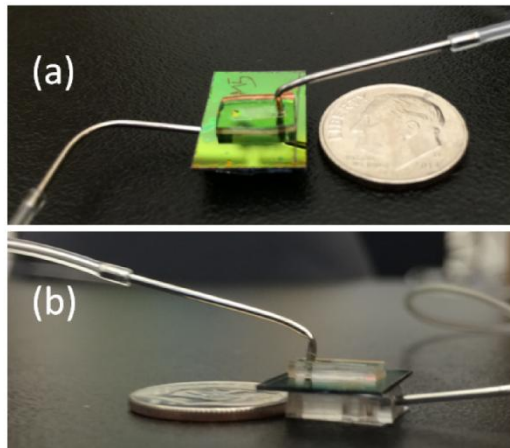


Figure 4.3. (a) Top-view and (b) side-view of the PSi membrane sensors integrated with PDMS flow cells.

4.2.4 Optical Reflectivity Measurement

A fiber-coupled Ocean Optics USB4000 CCD spectrometer was used to collect reflectance spectra over a spot size of approximately 1 mm in diameter at the center of the PSi samples. Reflectivity data were recorded continuously every 20 s with a spectral acquisition time of 10 ms over a wavelength range of 500 to 1000 nm. The measured reflectance spectra were referenced against a gold mirror standard.

Figure 4.4 shows the reflectance spectra of a PSi microcavity measured after each device fabrication step. Thermal oxidation reduced the index contrast in microcavity layers and blue-shifted the microcavity resonance. During the photolithography process, the silicon substrate underneath PSi was removed for the formation of open-ended membrane. The position of the microcavity resonance was maintained due to the protection from sacrificial layers that prevented any etching or other modification of the PSi microcavity; however, removal of the silicon substrate reduced the reflectance intensity of the PSi membrane. Finally, attachment of flow cells

slightly red-shifted the microcavity resonance. We note that the resonance wavelength of the fabricated PSi microcavity membranes can vary ± 5 nm depending on the position of the membrane on the silicon wafer. Such nonuniformity arises from anodization, during which time the current density applied to the center of a wafer is usually higher than the edge of a wafer, causing lateral variation in porosity. Reflectance spectra of on-substrate PSi microcavities in the flow-over configuration were very similar to those shown in Figure 4.4.

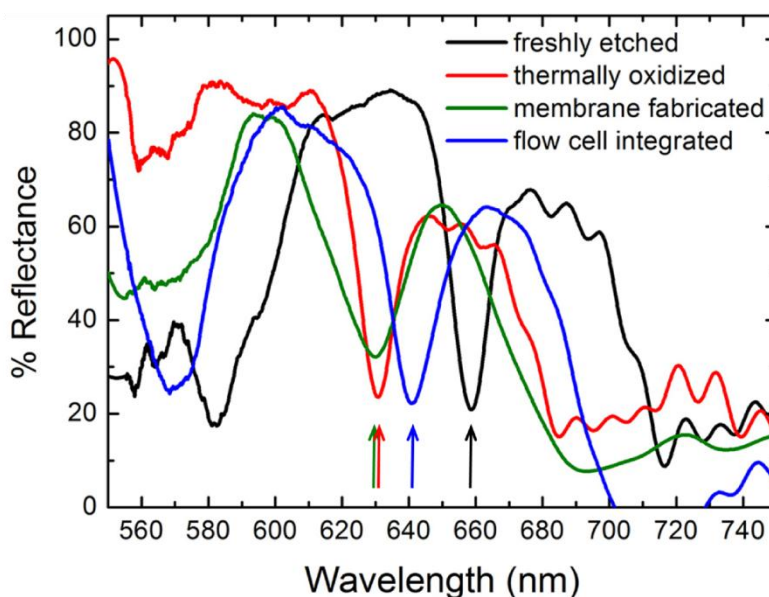


Figure 4.4. Reflectance spectra of the PSi microcavity measured after electrochemical etching (black line), oxidation (red line), removal of silicon substrate (green line), and flow cell attachment (blue line). All measurements were taken in air. The resonance wavelength after each step is identified with an arrow.

4.3 Effect of Analyte Size on Sensor Response

As discussed in Chapter 3, the sensor response time for the flow-over scheme can take hours when the analyte diffusivity is low, as is the case for high molecular weight species. In comparison, in the flow-through scheme, the enhanced efficiency of analyte transport in the

pores allows the response time to remain almost the same as the analyte diffusivity varies over orders of magnitude. To validate the computational results, 3-aminopropyltriethoxysilane (3-APTES), horseradish peroxidase (HRP), and catalase (CAT) were employed as representative analytes for their different molecular sizes and varied diffusivities in the range of 10^{-9} - 10^{-11} m²/s. 3-APTES is a small aminosilane with a molecular weight of 221 Da and a length \approx 0.8 nm. A 2% 3-APTES solution in DI water and methanol was continuously injected for reaction with the oxidized PSi. HRP is a 44 kDa glycoprotein with a diameter \approx 4 nm and isoelectric point of 7.2. A 1 mM sodium acetate buffer at pH 5 was used to prepare a 5 μ M HRP solution with pH 5. At pH values lower than its isoelectronic point, HRP molecules become positively charged, and they can therefore electrostatically adsorb onto the negatively charged oxidized PSi. CAT is a common enzyme that catalyzes the decomposition of hydrogen peroxide to water and oxygen. It is a relatively large 247.5 kDa molecule with a diameter \approx 10.2 nm and isoelectric point of 5.4. PBS buffer at pH 7 (8 g NaCl, 0.2 g KCl, 1.44 g Na₂HPO₄, and 0.24 g KH₂PO₄ in 1 L of DI water) was used to dilute the CAT solution to a concentration of 5 μ M at pH 7. All solutions were injected at 5 μ L/min and a rinsing step with DI water was performed after each molecular adsorption step to remove unbound species.

The attachment of 3-APTES involves a silanization process, while protein adsorption is charge-based. The simulation results in Figure 3.10 suggested that due to mass transport limitations, the response time of the porous sensor is dominated by analyte diffusivity, and is only weakly dependent on adsorption rate constants. Therefore, the sensor response for adsorption of 3-APTES and proteins is primarily determined by their different sizes (i.e., diffusivities) rather than adsorption mechanisms.

For the flow-over PSi microcavities with closed-ended pores, the adsorption of 3-APTES and HRP quickly reached saturation in approximately 10 and 20 min, respectively, while the adsorption of the large CAT protein was slow (Figure 4.5). This trend corresponds well to the simulation results presented in Figure 3.10 that show for larger molecules that diffuse more slowly, the closed-ended PSi sensor takes longer to reach equilibrium. For the CAT protein, an approximately 1.5 nm wavelength shift was measured using the closed-ended pore microcavity after 120 min of continuous analyte injection. The slow response of this PSi microcavity to CAT adsorption is attributed to the corresponding relatively low diffusivity of CAT and the relatively large size of this protein molecule compared to the nanoscale pore diameters. As the CAT molecules have a hydrodynamic diameter of approximately 10.2 nm, the pore diameters in the low porosity layers of the PSi sample become substantially reduced in half from 20 ± 5 nm to about 10 ± 5 nm upon capturing one CAT molecule. Electrostatic repulsion between protein molecules and steric hindrance in the pore entrance significantly reduce the probability of CAT protein molecules continuing to enter the pores.

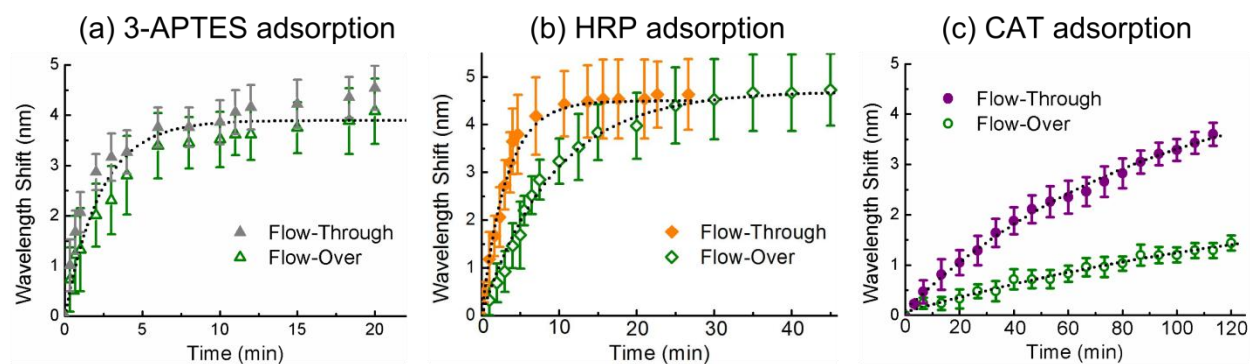


Figure 4.5. Comparison of real-time PSi microcavity response for closed-ended pores in the flow-over scheme and open-ended pores in the flow-through scheme. Time-dependent PSi microcavity resonance wavelength shifts upon exposure to (a) 3-APTES, (b) HRP, and (c) CAT.

Solid symbols are experimental data obtained from an open-ended, flow-through PSi microcavity membrane; hollow symbols are experimental data from a closed-ended flow-over PSi microcavity. Dotted lines provide guides to the eye. Reprinted with permission from Ref. [150]. Copyright 2016 Springer.

Replacing a closed-ended flow-over PSi microcavity with an open-ended flow-through PSi microcavity membrane should enable more efficient transport of analyte to the in-pore sensing surface based on the simulation results presented in Chapter 3. Accordingly, we performed the same molecule adsorption experiments with open-ended PSi microcavity membranes (Figure 4.5). The sensor response for 3-APTES adsorption was similarly fast in both flow schemes due to non-hindered pore entry for these small molecules and their fast diffusive transport. For larger analytes, there is little benefit to using the flow-through scheme for HRP adsorption since less than a 2-fold improvement in response time was obtained as compared to the flow-over scheme; however, for CAT adsorption, the flow-through membrane provided a much faster response. The time for the PSi microcavity to reach a 1 nm wavelength shift, a readily measurable value, was one-fourth that when the flow-through scheme was utilized. The experimental results indicate that the flow-through PSi membrane is most beneficial for analysis of analytes that can enter the pores but with relatively large dimensions such as antibodies, large proteins, and long nucleic acids. Those molecules, whose diffusivities are on the order of 10^{-11} m²/s, also exhibit the greatest improvement ratio by the flow-over format to the flow-through format in their simulated equilibrium times. In contrast, small analytes such as 3-APTES and HRP, whose diffusivities are faster than 10^{-10} m²/s, show no significant decreases in response time in both experimental and simulation results when employing the flow-through approach.

4.4 Surface Sensing

The sensing performance of the PSi films in both the flow-over (i.e., no membrane) and flow-through (i.e., membrane) schemes were evaluated by detecting the specific binding of streptavidin (STV, 52.8 kDa, ~5 nm diameter), a molecule whose diffusivity is on the order of 10^{-11} m²/s, to appropriately functionalized PSi films. In the first functionalization step, a 2% 3-APTES (~0.8 nm molecular length) solution composed of 20 μ L 3-APTES, 50 μ L DI water, and 950 μ L methanol was continuously flowed through the membrane and across the on-substrate sample for 30 min to provide amine terminations on the oxidized PSi. After drying in air, the PSi flow cell sample was transferred to an oven and baked at 150 °C for 20 min with a 30 min ramp up time and 30 min cool down time. This annealing step was used to promote stable 3-APTES monolayer formation. The relatively slow ramp times were necessary to ensure the integrity of the PSi membranes was not compromised due to thermal shock. In the next step, 1 mM sulfo-NHS-biotin (~1 nm diameter) in DI water was continuously injected into the flow cell for 30 min. Finally, STV solutions of various concentrations in DI water were continuously injected until all binding sites were saturated, as indicated by no further shifts in the microcavity resonance peak. The STV solutions were injected at 2 μ L/min while all the other solutions were injected at 5 μ L/min. A rinsing step with DI water was performed after each functionalization step to remove unbound species.

When analytes are captured on the pore walls, the effective refractive index of PSi increases and the microcavity resonance red-shifts to longer wavelengths. As a result, by monitoring the reflectance spectra, analyte binding can be detected quantitatively in a label-free way. Figure 4.6 shows the reflectance spectra of the flow-through PSi microcavity membrane measured after each surface functionalization step. Amine functionalization of an oxidized PSi membrane

microcavity with 2% 3-APTES led to a red-shift in its resonance wavelength of about 4 nm. Subsequent reaction of 1 mM sulfo-NHS-biotin to the amines shifted the spectra towards longer wavelengths by about 8 nm, and finally capturing 5 μ M of STV red-shifted the spectra by about 4 nm. Larger resonance shifts indicate the attachment of more material to the pores, either due to a molecule having a larger size or being present at a higher fractional surface coverage. All wavelength shifts in Figure 4.6 were measured after equilibrium was reached.

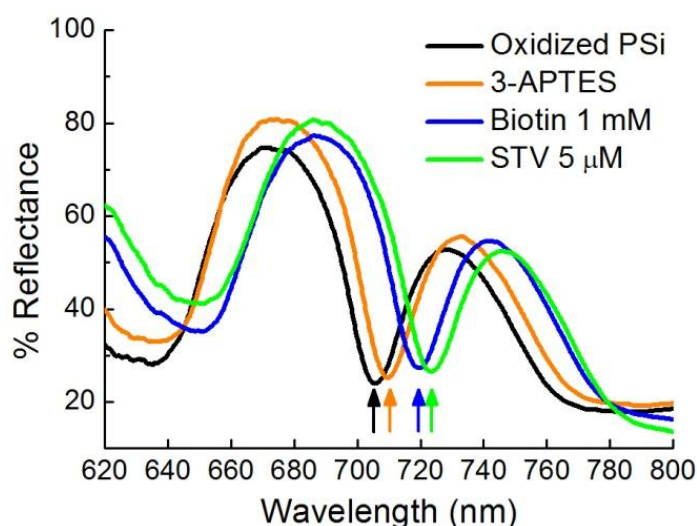


Figure 4.6. Reflectance spectra of the flow-through PSi membrane measured after oxidation, 3-APTES functionalization, biotin attachment, and streptavidin binding. All spectra were recorded in a flow cell environment after equilibrium was reached. The resonance wavelength after each step is identified with an arrow. Reprinted with permission from Ref. [149]. Copyright 2016 American Chemical Society.

The resonance shifts for the biotin-functionalized PSi upon exposure to 5 μ M STV as a function of time for both flow schemes are shown in Figure 4.7. The flow-through sensor exhibited a more rapid response. For example, in the first 10 min, a 2.7 nm wavelength shift was

observed for the flow-through scheme, while only 0.3 nm shift was measured for the flow-over scheme, suggesting a nine-fold faster sensor response by employing the flow-through PSi membranes. As time increased, the response by both flow schemes slowed as the PSi sensors approached saturation. The PSi sensor in the flow-through scheme reached its limitation of wavelength shift value in approximately 25 min, while it took more than 2 h for the PSi sensor in the flow-over scheme to saturate its response. This measurement indicates that the sensor saturation time for STV detection is reduced to one-sixth when the open-ended PSi membrane design is utilized, which is consistent with the simulations in Chapter 3. For a practical biosensor, the signal needed for detection is less than its saturation response and therefore the flow-through approach may provide more than this 6-fold improvement in sensing time.

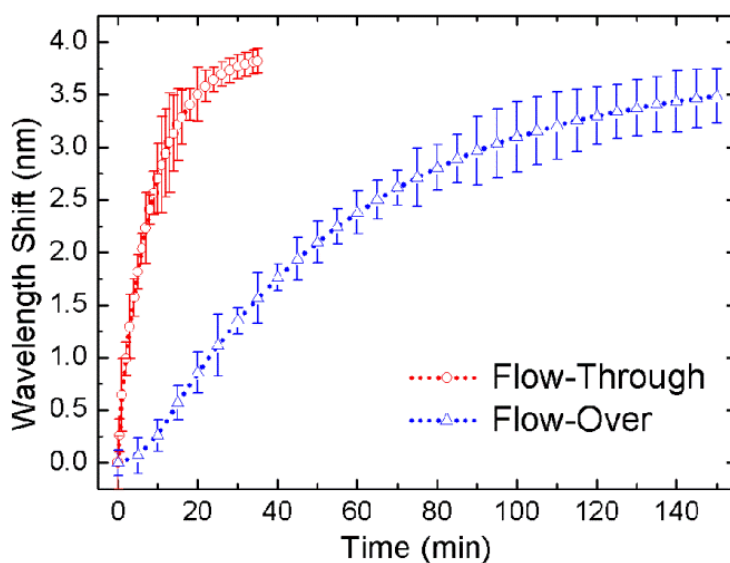


Figure 4.7. Comparison of real-time sensor response to 5 μM STV solution with different flow schemes. Measured PSi microcavity resonance wavelength shifts were plotted as a function of exposure time. Reprinted with permission from Ref. [149]. Copyright 2016 American Chemical Society.

The P*Si* sensors were exposed to different concentrations of STV in order to investigate the repeatability of sensing results across different membrane and on-substrate samples and to assess how the resonance wavelength shifts varied as a function of STV concentration for the membrane and on-substrate microcavities. Figure 4.8 shows the resonance shifts of the P*Si* sensors in both flow schemes after 20 min and 2 h, respectively. The small standard deviation of the wavelength shift for STV detection ($< \pm 0.3$ nm after 20 min exposure) indicates good repeatability and consistency of the sensing results. After 20 min, the resonance shifts from the flow-through P*Si* membranes were clearly larger than the on-substrate P*Si* sensors with closed-ended pores. Additionally, for STV solutions with concentrations of 1 μ M and 500 nM, the flow-through P*Si* membranes showed larger wavelength shifts compared with flow-over sensors at both 20 min and 2 h time points. This difference can be explained by the increased number of molecules transported to the sensor surface in the flow-through scheme. For a 5 μ M STV solution, its concentration of STV was sufficient such that even with slower mass transport, the flow-over sensor exhibited the same resonance shift as the flow-through sensor after 2 h. These results show that the open-ended P*Si* membranes enable effective and efficient analyte delivery and significantly reduce the sensor response time for relatively low concentration STV detection.

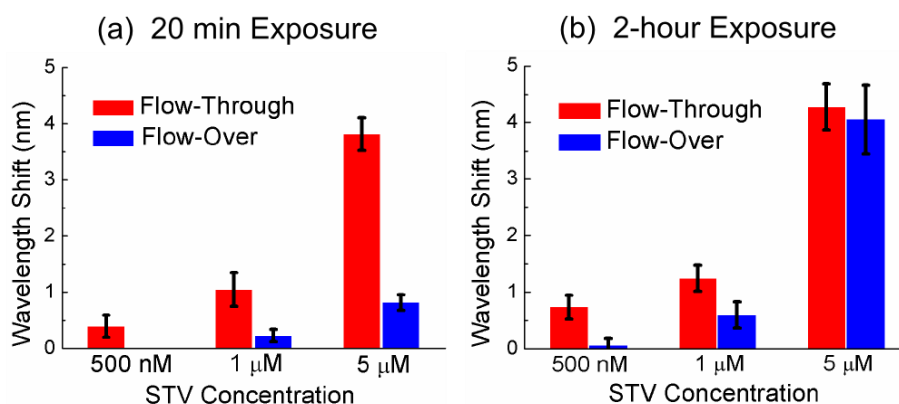


Figure 4.8. P*Si* microcavity wavelength shift measured after (a) 20 min and (b) 2 h exposures to 500 nM, 1 μM, and 5 μM STV solutions under different flow schemes. Reprinted with permission from Ref. [149]. Copyright 2016 American Chemical Society.

4.5 Quantum Dot Based Fluorescence Measurement

The improved analyte transport efficiency within open-ended P*Si* membranes was further confirmed by QD based fluorescence measurements. Here, the oxidized P*Si* microcavities were first functionalized with a 3 wt% Polydiallyldimethylammonium chloride (PDDA) aqueous solution, followed by a DI water rinse to remove excess molecules. PDDA molecules impart a positive charge to the oxidized P*Si* substrates upon attachment, which facilitates the adsorption of negatively charged colloidal QDs [208]. Then a 30 μM solution of negatively charged AgInS₂/ZnS QDs in DI water was injected in the microfluidic channels over 20 min using a flow-through or flow-over geometry. The QDs used in this thesis were synthesized at the Vanderbilt Institute for Nanoscale Science and Engineering (VINSE), following procedures detailed in Ref. [209,210]. The AgInS₂/ZnS QDs (~3 nm diameter) electrostatically attach to the positively charged PDDA coated oxidized P*Si* surface to form a monolayer of QD within the P*Si* matrix. All the solutions were injected in flow cells at 5 μL/min.

The resonance wavelength of the PSi microcavity was aligned with the peak emission of the QDs in order to achieve enhanced photoluminescence (PL) from the QDs immobilized in the microcavity structure [211]. A 488 nm laser (Coherent OBIS) was operated at 10 mW/cm² to excite QD emission from PSi samples. The PDMS flow cells were peeled off from PSi samples for fluorescence measurement and imaging. Visible QD emission between 200 and 1000 nm was recorded at normal incidence using a fiber-coupled Ocean Optics USB400 CCD spectrometer fitted with an Olympus SPlan 10× microscope objective lens. Camera images of QDs in PSi were taken under UV (365 nm) excitation.

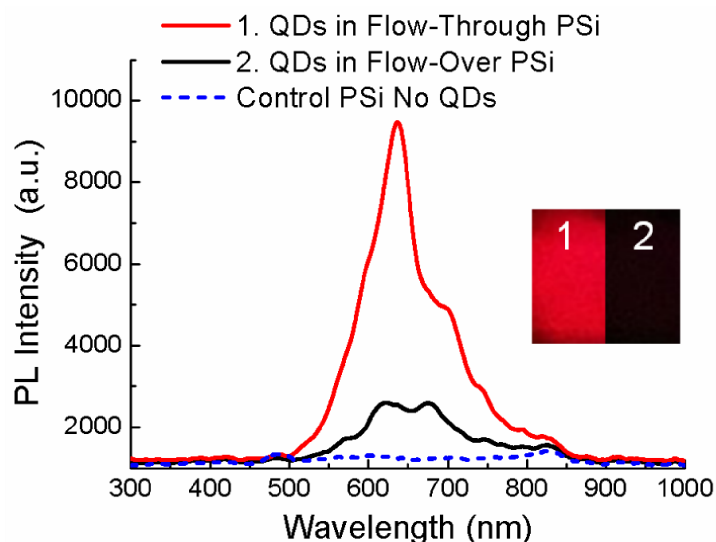


Figure 4.9. Photoluminescence spectra measured under 488 nm laser excitation from QDs adsorbed within flow-through and flow-over PSi microcavities and a control PSi microcavity sample with no QD functionalization. The inset shows camera images of the samples under UV excitation at 365 nm: 1) QDs in an open-ended PSi membrane in the flow-through scheme and 2) QDs in a closed-ended PSi film in the flow-over scheme. Both the PL spectra and camera images were obtained in air from PSi microcavities after their removal from the flow cells. Reprinted with permission from Ref. [149]. Copyright 2016 American Chemical Society.

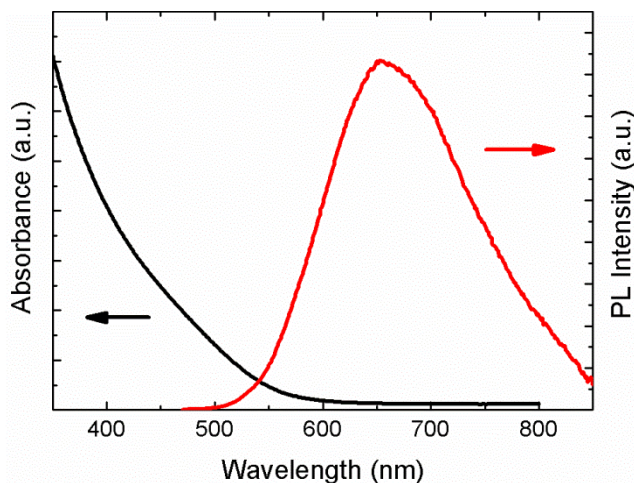


Figure 4.10. Absorbance and photoluminescence spectra for AgInS₂/ZnS quantum dots in a 30 μM aqueous solution.

The measured PL spectra of the immobilized QDs in both PSi samples (Figure 4.9) show good spectral agreement with the PL for these QDs in solution (Figure 4.10). The PL intensities scale with the number of QDs in the sample volume and, in the case of the QDs attached to a PSi microcavity, the wavelengths of QD emission outside the microcavity resonance are suppressed [212,213]. QD fluorescence from the on-substrate closed-ended PSi exhibited low PL intensity and little QD fluorescence was captured in the camera image. With the flow-through scheme, a strong QD emission from the PSi membrane was observed in both the PL spectra and camera image, suggesting enhanced transport of QDs into the porous sensing region. The total QD fluorescence intensity from PSi was quantified by integrating the area under the PL curve and subtracting the baseline PL obtained from PSi samples with no QD functionalization. The flow-through PSi membrane showed 4.4 times stronger QD fluorescence as compared to the closed-ended flow-over PSi film. This enhancement of QD fluorescence by employing the flow-through scheme is less than the enhancement of wavelength shift in STV detection. Considering the

respective sizes of AgInS₂/ ZnS QD (~3 nm diameter) and STV (~5 nm diameter), this difference is in agreement with the numerical simulation results in Chapter 3 that the flow-through scheme is more beneficial for detecting larger analytes.

4.6 Pressure Test

The mechanical stability of PSi membranes is critical in order to avoid membrane fracture during flow-through sensing experiments. A non-contact pressure test setup based on interferometric profilometry was used to characterize the mechanical strength of the PSi membrane, following procedures developed by Nicholl *et al.* [214]. Figure 4.11 shows the experimental setup. The PSi membrane was mechanically clamped to a customized holder, allowing pressure to be applied to one side of the membrane. The deflection of the membrane under applied pressure was determined by interferometric profilometry. In this technique, the height profile of the surface is determined by monitoring the phase shift of light reflected from the sample surface. The resolution of measured vertical deflection is $\pm 1 \mu\text{m}$. Compared with AFM-based nanoindentation, this non-contact technique prevents the membrane morphology from being disturbed with a sharp tip and allows pressure to be applied uniformly.

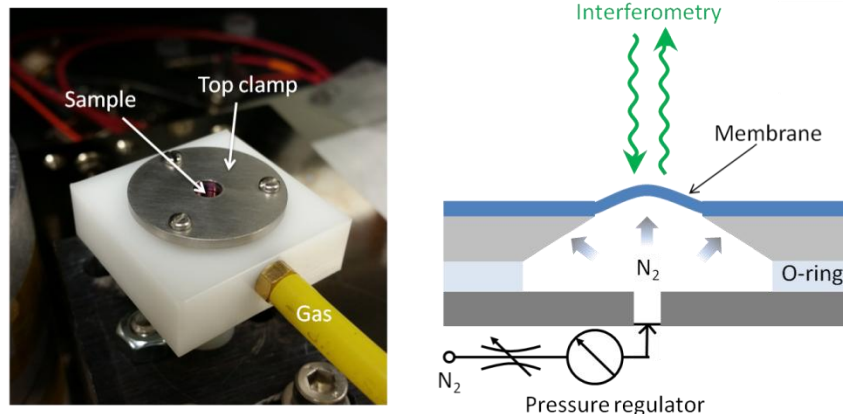


Figure 4.11. Camera image and schematic illustration of the experimental setup for pressure test. Adapted with permission from Ref. [214]. Copyright 2015 Macmillan Publishers Limited.

The PSi membrane under test consisted of a multilayer microcavity structure alternating in regions of high (80%) and low (65%) porosity. Initial bulging of the membrane was observed at 0 psi of applied pressure, as indicated by the non-uniform color distribution across the membrane region in the microscope image (Figure 4.12, bottom). In order to study the cause of this initial bulging, the same measurement was performed on a single layer PSi membrane sample with uniform porosity (80%) and similar thickness ($\sim 12 \mu\text{m}$) as the microcavity membrane sample ($\sim 15 \mu\text{m}$). The vertical deflection of the microcavity membrane at 0 psi was $\sim 30 \mu\text{m}$, while only $\sim 2 \mu\text{m}$ deflection was measured for the single layer membrane. Therefore, initial bulging of the membrane is attributed in large part to the built-in stress within the heterostructure of different porosities.

As shown in Figure 4.12, one PSi microcavity membrane sample maintained its structural integrity under 10 psi of applied pressure; however, fracture of the sample occurred at 11 psi. The same test was performed on five different microcavity membrane samples and the resulting

average maximum pressure that the membrane elastically deforms was determined to be 7 ± 2.9 psi. The large standard deviation can be explained by the variation of membrane thicknesses due to radial etch rate non-uniformity in reactive ion etching. The average maximum loading force, obtained by multiplying the maximum pressure with the area of the membrane (1 mm^2), is calculated to be $49 \pm 20 \text{ mN}$. However, this number should be treated as a lower bound value considering that the maximum pressure is applied in addition to the built-in stress of the sample and finer pressure increment steps can be taken for more precise measurement. We expect the maximum applied pressure and loading force can be further improved by reducing the built-in stress within PSi layers through porosity engineering and morphology optimization.

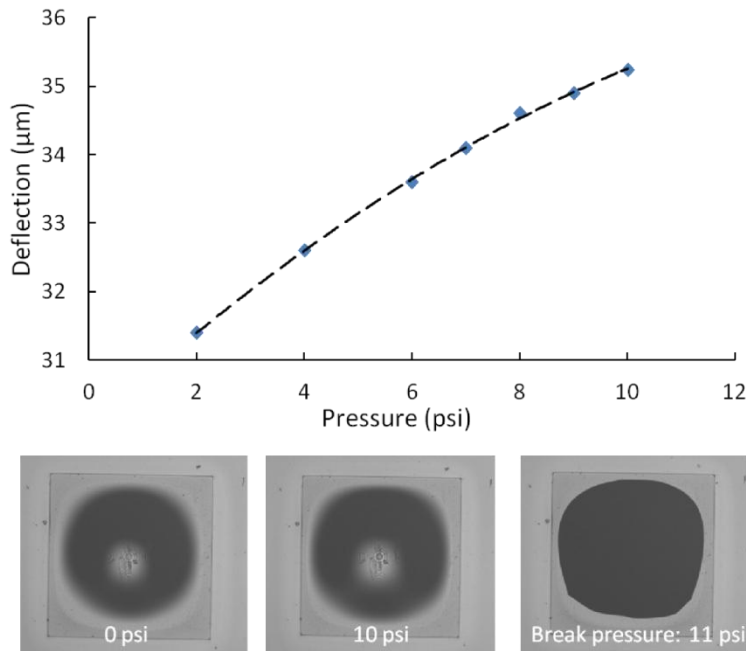


Figure 4.12. Vertical deflection of the PSi membrane at various applied pressures. Height profile was obtained from interferometric profilometry. The dashed line is shown as a guide to the eye. Microscope images of the $1 \text{ mm} \times 1 \text{ mm}$ PSi membrane under different pressure are shown in

bottom panels. At 0 psi of applied pressure, the membrane showed initial bulging due to build-in stress. The membrane maintained its structural integrity at 10 psi. Breakage occurred at 11 psi.

4.7 Summary

A flow-through optical biosensor based on open-ended PSi sensor membranes was designed and characterized. For the first time, the PSi membranes served as nanochannels to greatly enhance transport of analytes to the active sensing regions inside the nanopores. The designed PSi optical microcavity structure served to improve the sensor response by increasing the sensitivity of the cavity region to perturbations in its effective refractive index upon target analyte capture and to the emission of QDs captured within the cavity. In comparison to a conventional flow-over PSi sensor, the open-ended PSi microcavity membrane exhibited a 4-fold faster response when exposed to the large, 247.5 kDa CAT protein, as the flow-through scheme facilitated improved mass transport. For the adsorption of smaller molecules – 3-APTES (221 Da) and HRP (44 kDa) – little to no sensor performance improvement was observed as the closed-ended PSi microcavities did not suffer significant mass transport challenges with these molecules. When detecting streptavidin binding to biotin-functionalized PSi, the flow-through PSi membrane resulted in a 6-fold improvement in response time versus in the flow-over PSi approach. The flow-through PSi also showed larger resonance wavelength shifts after 20 min for all concentrations (0.5-5 μ M) of streptavidin exposed to the membrane and on-substrate PSi sensors. The presented PSi membranes were patterned using photolithographic techniques in a standard CMOS process that would enable parallel low-cost manufacture at wafer-scales. The membranes in this work showed sufficient mechanical stability that could easily withstand

multiple rinsing and drying cycles in flow-through experiments. Importantly, the photolithographically patterned membranes hold great promise for the construction of flow-through PSi microarrays, allowing for the rapid label-free detection of multiple analytes in a single parallel experiment.

CHAPTER 5

CONCLUSIONS

5.1 Summary

This thesis reports on new approaches to improve the surface stabilization and analyte transport efficiency in PSi photonic structures for biosensing applications. The ability to protect PSi against degradation in aqueous solutions improves the reliability, accuracy, and lifetime of the sensor. The design of an open-ended PSi membrane, allowing analyte solutions to pass through the pores, overcomes mass transport limitations facing traditional PSi multilayer structures. These methods enhance the biosensing capabilities of PSi and allow the development of novel optical biosensors that show great promise for future lab-on-chip and sensor array devices.

Chapter 2 investigated the influence of charge density and surface passivation on the corrosion process in the PSi matrix in order to improve PSi biosensor sensitivity, reliability, and reproducibility when exposed to negatively charged molecules. Due to DNA's negatively charged phosphate backbone, both increased DNA probe density and increased target DNA concentration enhance the corrosion process and mask binding events. A modified model based on nucleophilic attack of oxidized PSi surface by water molecules is proposed to explain the DNA-induced corrosion behavior in PSi samples that are well-passivated with a thermal oxide and silane layer. While passivation of the PSi surface is shown to diminish the corrosion rate and lead to a saturation in the corrosion effect after about two hours, complete mitigation can be achieved by replacing the DNA probe molecules with charge neutral PNA probe molecules and introducing Mg^{2+} ions to shield negative charges on the target DNA backbone during

hybridization to the PNA probes. Our results show that this anti-corrosion strategy increases the robustness of PSi DNA sensors without sacrificing sensitivity to DNA hybridization.

Due to the high aspect ratio of PSi nanopores, the performance of closed-ended PSi sensors is limited by infiltration challenges and slow sensor response when detecting molecules whose sizes approach the pore dimensions. **Chapter 3** presented a theoretical model to evaluate the analyte transport and time response of nanoporous sensors under two different flow schemes. In the conventional flow-over scheme, the pores are closed-ended such that solutions enter and exit through the same end of the pores. In the flow-through scheme, pores are open-ended, enabling solutions to enter at one end of the pores and exit through their other end. The simulated adsorption behavior of small analytes onto the inner surface of porous sensors was similar in both flow schemes. However, for large analytes, open-ended membranes in a flow-through scheme showed significant improvement in response times due to convective transport of analytes. The computational analysis further showed how control over the flow velocity of the analyte delivered to porous sensors affects the sensor response time and total volume of analyte consumed. It was found that the flow-through scheme enables more reasonable response times for the detection of dilute analytes and reduces the volume of solution required for analysis. Experimental demonstration of the results was discussed in Chapter 4.

Chapter 4 presented the fabrication and biosensing experiments of an open-ended PSi microcavity membrane that allows analytes to flow through the pores in microfluidic-based assays. Our experimental results agree with finite element method simulations in Chapter 3 and show that flow-through biosensing using the PSi membranes enables a 6-fold improvement in

sensor response time compared to closed-ended, flow-over PSi sensors when detecting high molecular weight analyte (e.g., streptavidin). For small analytes (e.g., 3-APTES), little to no sensor performance improvement is observed as the closed-ended PSi films do not suffer significant mass transport challenges with these molecules. The PSi membrane was fabricated using standard photolithographic techniques, which makes possible high-throughput production and integration in on-chip sensor arrays. The future work of developing PSi microarrays and using PSi photonic structures to resonantly enhance the emission of QDs for colorimetric detection will be discussed in the following sections.

5.2 Future Research Opportunities

5.2.1 PSi Microarrays for Multiplexed Biosensing

In order to obtain higher throughput while maintaining a high detection sensitivity to minute amounts of analyte, one can increase the number of sensor elements per unit area by creating sensor microarrays. A microarray consists of a solid substrate where small volumes of different bioreceptors can be immobilized in defined regions, allowing multiplexed detection and analysis of molecular binding activities [215]. There are several advantages of incorporating the array format in PSi based biosensors. Firstly, due to the inhomogeneous distribution of the electric field during PSi etching, the optical properties of PSi are spatially varied. It is much more accurate to measure the optical response of PSi from precise positions rather than monitoring the average optical response from a large area of PSi. Secondly, the microarray structure allows discrete array elements of PSi to be functionalized differently via robotic spotting techniques, which offers great potential in highly parallel biosensing applications, especially for serum-based

assays. PSi substrates have been used in DNA and protein microarrays for their large surface area that increases the density of bioreceptors immobilized on each array spot [216-218]. Most of the reported PSi microarrays rely on the use of fluorescent markers that require additional processing and labeling cost. The integration of photonic structures in PSi microarrays opens the door to a label-free, low-cost, and multiplexed sensing platform.

Figure 5.1a shows the image of a 4×4 PSi microarray sample with a microcavity structure etched in each array element. The fabrication of the PSi microarray started with deposition of a 400 nm silicon nitride film on a *p*-type silicon wafer by PECVD. A photolithographic process was used to pattern the silicon nitride film to form 4×4 arrays with circular exposed regions of 300 μm in diameter. RIE was used to remove the exposed regions of silicon nitride. The remaining silicon nitride serves as a mask during the subsequent electrochemical etching. The microcavity structure was formed using the same electrochemical etching parameters as described in Section 4.2.1. The blue circle in Figure 5.1a indicates the shape of the O-ring used in the etch cell. The silicon nitride film inside the circle was exposed to HF during PSi formation while the silicon nitride film outside the circle had no exposure to HF. Different colors of the silicon nitride film indicate different film thicknesses. The etch rate of PECVD silicon nitride in 15% HF acid in ethanol was estimated to be 0.23 nm/s based on ellipsometry. The silicon nitride film shows good resistance against HF and effectively protects the silicon underneath it from being etched. Figure 5.1b shows the measured reflectance spectra in one array element. The etching parameters used here were optimized for large-area wafer-scale PSi etching. For etching in microarray substrates with small exposed area, the etching parameters and microcavity configurations need to be further optimized to improve the quality of the microcavity while maintaining sufficiently large pore dimensions for sensing applications. The variance of the

microcavity resonance of each array element is less than ± 1 nm due to their adjacent positions that increase the anodization uniformity. Alternatively, the approach for fabricating open-ended PSi membranes can be easily adapted for integration in microarrays as detailed in Section 4.2.2. Unlike the previously mentioned process in which PSi is formed on pre-patterned silicon substrates, in this case PSi would be firstly formed followed by photolithographic patterning, which ensures the high etching quality of PSi photonic structures. Despite the continuity of PSi film etched on the silicon wafer, the PSi region in each array element is isolated by the silicon nitride mask and thus can be functionalized individually. The experimental realization of microarray based flow-through biosensing has the potential to achieve rapid multiplexed biodetection with a small input of analyte solutions.

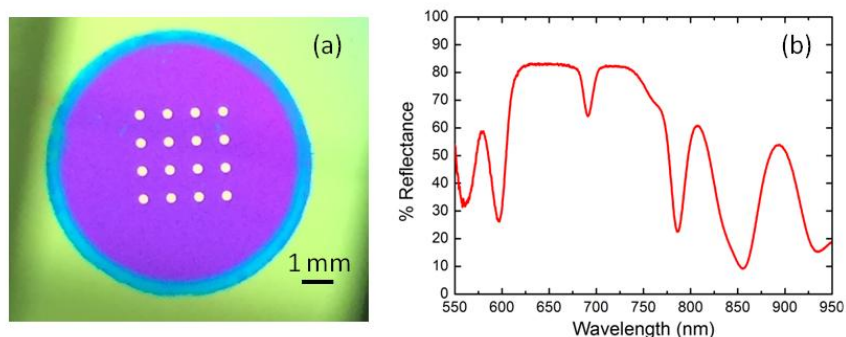


Figure 5.1. (a) Camera image of the PSi microcavity microarray. The diameter of each array element is $300 \mu\text{m}$ and the distance between each element is $700 \mu\text{m}$. (b) Reflectance spectra of a PSi microcavity element in the array.

The common way to simultaneously measure all array elements in a label-free manner is to use a detector array consisting of multiple optical reflection probes. However, the bulky instrumentation and precise alignment required for the detector array make it inappropriate for

compact portable applications. In the following section, a label-free colorimetric detection approach is proposed, which can be easily integrated with PSi microarrays for the construction of a cost-effective, portable, and highly sensitive biosensing platform.

5.2.2 Quantum Dot Coupled PSi for Colorimetric Sensing

As shown in Section 4.5, the PSi microcavity is an excellent host-matrix for QDs since it enables large quantities of QDs to be immobilized throughout the porous matrix, and it amplifies the QD emission through cavity modification. The microcavity resonance strongly influences the original broad emission of the QDs, suppressing the emitted wavelengths outside the resonance and enhancing the on-resonance wavelengths. Further investigation exploring the integration of QDs with resonant PSi photonic structures could lead to a low-cost, portable, and highly sensitive label-free colorimetric sensing platform. As shown in Figure 5.2, binding of molecules to functionalized QDs, or alternatively on functionalized pore walls where QDs are not attached, would lead to a resonance shift of the PSi microcavity and a concurrent color change in the cavity-modified QD emission. Hence, the presence of molecules could be detected in a label-free manner as a simple color-change, requiring an inexpensive laser pointer to excite QD emission and a camera to record fluorescence images. Resonant photonic structures that are capable of achieving stronger light-matter interaction than the one-dimensional microcavity can be used to further enhance the cavity-modified QD emission and improve the detection sensitivity of the colorimetric sensing platform.

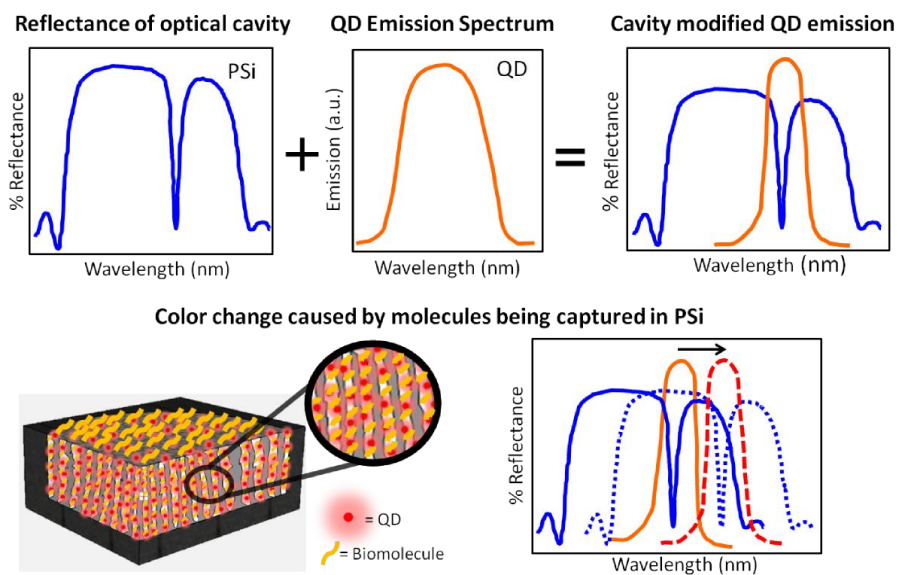


Figure 5.2. Schematic illustration of colorimetric sensing in QD coupled PSi microcavity. QDs are infiltrated into PSi microcavity to achieve cavity modified QD emission. Any changes to the environmental refractive index of the sensor upon target molecule capture will perturb the cavity resonance conditions, causing a shift in the cavity coupled QD emission spectra. This shift in the QD emission profile can be detected as color change using a camera.

REFERENCES

1. Sadana, A., Sadana, N. In Biomarkers and biosensors; Sadana A S, Ed.; Elsevier: Amsterdam, 2015, p 653-680.
2. Luong, J. H. T., Male, K. B., Glennon, J. D.: Biosensor technology: Technology push versus market pull. *Biotechnology Advances*, 2008, **26**, 492-500.
3. Fan, X. D., White, I. M., Shopova, S. I., Zhu, H. Y., Suter, J. D., Sun, Y. Z.: Sensitive optical biosensors for unlabeled targets: A review. *Analytica Chimica Acta*, 2008, **620**, 8-26.
4. Borisov, S. M., Wolfbeis, O. S.: Optical biosensors. *Chemical Reviews*, 2008, **108**, 423-461.
5. Lequin, R. M.: Enzyme immunoassay (EIA)/enzyme-linked immunosorbent assay (ELISA). *Clinical Chemistry*, 2005, **51**, 2415-2418.
6. <http://www.gelifesciences.com/webapp/wcs/stores/servlet/catalog/en/GELifeSciences-us/brands/biacore>
7. Cooper, M. A.: Optical biosensors in drug discovery. *Nature Reviews Drug Discovery*, 2002, **1**, 515-528.
8. Hoa, X. D., Kirk, A. G., Tabrizian, M.: Towards integrated and sensitive surface plasmon resonance biosensors: A review of recent progress. *Biosensors & Bioelectronics*, 2007, **23**, 151-160.
9. Shankaran, D. R., Gobi, K. V. A., Miura, N.: Recent advancements in surface plasmon resonance immunosensors for detection of small molecules of biomedical, food and environmental interest. *Sensors and Actuators B-Chemical*, 2007, **121**, 158-177.
10. Otto, A.: Excitation of nonradiative surface plasma waves in silver by method of frustrated total reflection. *Zeitschrift Fur Physik*, 1968, **216**, 398-410.
11. Homola, J., Koudela, I., Yee, S. S.: Surface plasmon resonance sensors based on diffraction gratings and prism couplers: Sensitivity comparison. *Sensors and Actuators B-Chemical*, 1999, **54**, 16-24.
12. Hecht, B., Bielefeldt, H., Novotny, L., Inouye, Y., Pohl, D. W.: Local excitation, scattering, and interference of surface plasmons. *Physical Review Letters*, 1996, **77**, 1889-1892.

13. Rich, R. L., Myszka, D. G.: Advances in surface plasmon resonance biosensor analysis. *Current Opinion in Biotechnology*, 2000, **11**, 54-61.
14. Homola, J.: Present and future of surface plasmon resonance biosensors. *Analytical and Bioanalytical Chemistry*, 2003, **377**, 528-539.
15. Green, R. J., Frazier, R. A., Shakesheff, K. M., Davies, M. C., Roberts, C. J., Tendler, S. J. B.: Surface plasmon resonance analysis of dynamic biological interactions with biomaterials. *Biomaterials*, 2000, **21**, 1823-1835.
16. Homola, J.: Surface plasmon resonance sensors for detection of chemical and biological species. *Chemical Reviews*, 2008, **108**, 462-493.
17. Daniels, J. S., Pourmand, N.: Label-free impedance biosensors: Opportunities and challenges. *Electroanalysis*, 2007, **19**, 1239-1257.
18. Anker, J. N., Hall, W. P., Lyandres, O., Shah, N. C., Zhao, J., Van Duyne, R. P.: Biosensing with plasmonic nanosensors. *Nature Materials*, 2008, **7**, 442-453.
19. Ligler, F. S.: Perspective on optical biosensors and integrated sensor systems. *Anal Chem*, 2009, **81**, 519-526.
20. Jane, A., Dronov, R., Hodges, A., Voelcker, N. H.: Porous silicon biosensors on the advance. *Trends in Biotechnology*, 2009, **27**, 230-239.
21. Torres-Costa, V., Martin-Palma, R. J.: Application of nanostructured porous silicon in the field of optics. A review. *Journal of Materials Science*, 2010, **45**, 2823-2838.
22. Dai, Z., Ju, H.: Bioanalysis based on nanoporous materials. *TRAC Trends in Analytical Chemistry*, 2012, **39**, 149-162.
23. Striemer, C. C., Gaborski, T. R., McGrath, J. L., Fauchet, P. M.: Charge- and size-based separation of macromolecules using ultrathin silicon membranes. *Nature*, 2007, **445**, 749-753.
24. Leichle, T., Bourrier, D.: Integration of lateral porous silicon membranes into planar microfluidics. *Lab on A Chip*, 2015, **15**, 833-838.
25. Velleman, L., Shearer, C. J., Ellis, A. V., Losic, D., Voelcker, N. H., Shapter, J. G.: Fabrication of self-supporting porous silicon membranes and tuning transport properties by surface functionalization. *Nanoscale*, 2010, **2**, 1756-1761.
26. Alvarez, J., Serrano, C., Hill, D., Martinez-Pastor, J.: Real-time polarimetric optical sensor using macroporous alumina membranes. *Optics Letters*, 2013, **38**, 1058-1060.

27. Alvarez, J., Sola, L., Cretich, M., Swann, M. J., Gylfason, K. B., Volden, T., Chiari, M., Hill, D.: Real time optical immunosensing with flow-through porous alumina membranes. *Sensors and Actuators B-Chemical*, 2014, **202**, 834-839.
28. Lee, W. H., Ngernsutivorakul, T., Mabrouk, O. S., Wong, J. M. T., Dugan, C. E., Pappas, S. S., Yoon, H. J., Kennedy, R. T.: Microfabrication and in vivo performance of a microdialysis probe with embedded membrane. *Analytical Chemistry*, 2016, **88**, 1230-1237.
29. Albu, S. P., Ghicov, A., Macak, J. M., Hahn, R., Schmuki, P.: Self-organized, free-standing TiO₂ nanotube membrane for flow-through photocatalytic applications. *Nano Letters*, 2007, **7**, 1286-1289.
30. Albu, S. P., Ghicov, A., Aldabergenova, S., Drechsel, P., LeClere, D., Thompson, G. E., Macak, J. M., Schmuki, P.: Formation of double-walled TiO₂ nanotubes and robust anatase membranes. *Advanced Materials*, 2008, **20**, 4135-4139.
31. Aran, K., Sasso, L. A., Kamdar, N., Zahn, J. D.: Irreversible, direct bonding of nanoporous polymer membranes to PDMS or glass microdevices. *Lab on A Chip*, 2010, **10**, 548-552.
32. Yang, H. C., Liao, K. J., Huang, H., Wu, Q. Y., Wan, L. S., Xu, Z. K.: Mussel-inspired modification of a polymer membrane for ultra-high water permeability and oil-in-water emulsion separation. *Journal of Materials Chemistry A*, 2014, **2**, 10225-10230.
33. Dhanekar, S., Jain, S.: Porous silicon biosensor: Current status. *Biosensors & Bioelectronics*, 2013, **41**, 54-64.
34. Gupta, B., Zhu, Y., Guan, B., Reece, P. J., Gooding, J. J.: Functionalised porous silicon as a biosensor: Emphasis on monitoring cells in vivo and in vitro. *Analyst*, 2013, **138**, 3593-3615.
35. Harraz, F. A.: Porous silicon chemical sensors and biosensors: A review. *Sens Actuators B-Chem*, 2014, **202**.
36. <http://www.siliconkinetics.com/technology>
37. <http://www.alere.com/en/home/products-services/other/womens-health/pregnancy.html>
38. Goluch, E. D., Nam, J. M., Georganopoulou, D. G., Chiesl, T. N., Shaikh, K. A., Ryu, K. S., Barron, A. E., Mirkin, C. A., Liu, C.: A bio-barcode assay for on-chip attomolar-sensitivity protein detection. *Lab on A Chip*, 2006, **6**, 1293-1299.
39. Oh, B. K., Nam, J. M., Lee, S. W., Mirkin, C. A.: A fluorophore-based bio-barcode amplification assay for proteins. *Small*, 2006, **2**, 103-108.

40. Nam, J. M., Jang, K. J., Groves, J. T.: Detection of proteins using a colorimetric bio-barcode assay. *Nature Protocols*, 2007, **2**, 1438-1444.
41. [Http://www.genalyte.com/about-us/our-technology](http://www.genalyte.com/about-us/our-technology)
42. Washburn, A. L., Luchansky, M. S., Bowman, A. L., Bailey, R. C.: Quantitative, label-free detection of five protein biomarkers using multiplexed arrays of silicon photonic microring resonators. *Analytical Chemistry*, 2010, **82**, 69-72.
43. Guo, Y., Ye, J. Y., Divin, C., Huang, B., Thomas, T. P., Baker, J. R., Jr., Norris, T. B.: Real-time biomolecular binding detection using a sensitive photonic crystal biosensor. *Analytical Chemistry*, 2010, **82**, 5211-5218.
44. Hu, S., Zhao, Y., Qin, K., Retterer, S. T., Kravchenko, I. I., Weiss, S. M.: Enhancing the sensitivity of label-free silicon photonic biosensors through increased probe molecule density. *ACS Photonics*, 2014, **1**, 590-597.
45. Qin, K., Hu, S. R., Retterer, S. T., Kravchenko, I. I., Weiss, S. M.: Slow light mach-zehnder interferometer as label-free biosensor with scalable sensitivity. *Optics Letters*, 2016, **41**, 753-756.
46. Wee, K. W., Kang, G. Y., Park, J., Kang, J. Y., Yoon, D. S., Park, J. H., Kim, T. S.: Novel electrical detection of label-free disease marker proteins using piezoresistive self-sensing micro-cantilevers. *Biosensors & Bioelectronics*, 2005, **20**, 1932-1938.
47. Hwang, K. S., Lee, J. H., Park, J., Yoon, D. S., Park, J. H., Kim, T. S.: In-situ quantitative analysis of a prostate-specific antigen (PSA) using a nanomechanical pzt cantilever. *Lab on A Chip*, 2004, **4**, 547-552.
48. Waggoner, P. S., Varshney, M., Craighead, H. G.: Detection of prostate specific antigen with nanomechanical resonators. *Lab on A Chip*, 2009, **9**, 3095-3099.
49. Weizmann, Y., Patolsky, F., Willner, I.: Amplified detection of DNA and analysis of single-base mismatches by the catalyzed deposition of gold on Au-nanoparticles. *Analyst*, 2001, **126**, 1502-1504.
50. Zheng, G., Gao, X. P., Lieber, C. M.: Frequency domain detection of biomolecules using silicon nanowire biosensors. *Nano Letters*, 2010, **10**, 3179-3183.
51. Bunimovich, Y. L., Shin, Y. S., Yeo, W. S., Amori, M., Kwong, G., Heath, J. R.: Quantitative real-time measurements of DNA hybridization with alkylated nonoxidized silicon nanowires in electrolyte solution. *Journal of the American Chemical Society*, 2006, **128**, 16323-16331.

52. Stern, E., Vacic, A., Rajan, N. K., Criscione, J. M., Park, J., Ilic, B. R., Mooney, D. J., Reed, M. A., Fahmy, T. M.: Label-free biomarker detection from whole blood. *Nature Nanotechnology*, 2010, **5**, 138-142.
53. Wang, J.: Electrochemical glucose biosensors. *Chemical Reviews*, 2008, **108**, 814-825.
54. Vedrine, C., Fabiano, S., Tran-Minh, C.: Amperometric tyrosinase based biosensor using an electrogenerated polythiophene film as an entrapment support. *Talanta*, 2003, **59**, 535-544.
55. Ronkainen, N. J., Halsall, H. B., Heineman, W. R.: Electrochemical biosensors. *Chemical Society Reviews*, 2010, **39**, 1747-1763.
56. Yun, Y., Bange, A., Heineman, W. R., Halsall, H. B., Shanov, V. N., Dong, Z., Pixley, S., Behbehani, M., Jazieh, A., Tu, Y., Wong, D. K. Y., Bhattacharya, A., Schulz, M. J.: A nanotube array immunosensor for direct electrochemical detection of antigen–antibody binding. *Sensors and Actuators B: Chemical*, 2007, **123**, 177-182.
57. Sailor, M. J. In *Porous silicon in practice*; Wiley-VCH, Weinheim 2012, p 1-42.
58. Stewart, M. P., Buriak, J. M.: Chemical and biological applications of porous silicon technology. *Advanced Materials*, 2000, **12**, 859-869.
59. Sailor, M. J.: Color me sensitive: Amplification and discrimination in photonic silicon nanostructures. *ACS Nano*, 2007, **1**, 248-252.
60. Lin, V. S. Y., Motesharei, K., Dancil, K. P. S., Sailor, M. J., Ghadiri, M. R.: A porous silicon-based optical interferometric biosensor. *Science*, 1997, **278**, 840-843.
61. Janshoff, A., Dancil, K.-P. S., Steinem, C., Greiner, D. P., Lin, V. S. Y., Gurtner, C., Motesharei, K., Sailor, M. J., Ghadiri, M. R.: Macroporous p-type silicon fabry–perot layers. Fabrication, characterization, and applications in biosensing. *Journal of the American Chemical Society*, 1998, **120**, 12108-12116.
62. Gruning, U., Lehmann, V., Engelhardt, C. M.: Two-dimensional infrared photonic band gap structure based on porous silicon. *Applied Physics Letters*, 1995, **66**, 3254-3256.
63. Gruning, U., Lehmann, V., Ottow, S., Busch, K.: Macroporous silicon with a complete two-dimensional photonic band gap centered at 5 μm . *Applied Physics Letters*, 1996, **68**, 747-749.
64. Birner, A., Wehrspohn, R. B., Gosele, U. M., Busch, K.: Silicon-based photonic crystals. *Advanced Materials*, 2001, **13**, 377-388.

65. Wolkin, M. V., Jorne, J., Fauchet, P. M., Allan, G., Delerue, C.: Electronic states and luminescence in porous silicon quantum dots: The role of oxygen. *Physical Review Letters*, 1999, **82**, 197-200.
66. Aravamudhan, S., Rahman, A. R. A., Bhansali, S.: Porous silicon based orientation independent, self-priming micro direct ethanol fuel cell. *Sensors and Actuators A: Physical*, 2005, **123-124**, 497-504.
67. Shin, H.-C., Corno, J. A., Gole, J. L., Liu, M.: Porous silicon negative electrodes for rechargeable lithium batteries. *Journal of Power Sources*, 2005, **139**, 314-320.
68. Kemell, M., Ritala, M., Leskelä M., Ossei-Wusu, E., Carstensen, J., Föll, H.: Si/Al₂O₃/ZnO:Al capacitor arrays formed in electrochemically etched porous si by atomic layer deposition. *Microelectronic Engineering*, 2007, **84**, 313-318.
69. DimovaMalinovska, D., SendovaVassileva, M., Tzenov, N., Kamenova, M.: Preparation of thin porous silicon layers by stain etching. *Thin Solid Films*, 1997, **297**, 9-12.
70. Li, X., Bohn, P. W.: Metal-assisted chemical etching in HF/H₂O₂ produces porous silicon. *Applied Physics Letters*, 2000, **77**, 2572-2574.
71. Geyer, N., Fuhrmann, B., Leipner, H. S., Werner, P.: Ag-mediated charge transport during metal-assisted chemical etching of silicon nanowires. *ACS Applied Materials & Interfaces*, 2013, **5**, 4302-4308.
72. Hu, Y., Peng, K. Q., Qiao, Z., Huang, X., Zhang, F. Q., Sun, R. N., Meng, X. M., Lee, S. T.: Metal-catalyzed electroless etching of silicon in aerated HF/H₂O vapor for facile fabrication of silicon nanostructures. *Nano Letters*, 2014, **14**, 4212-4219.
73. Smith, R. L., Collins, S. D.: Porous silicon formation mechanisms. *Journal of Applied Physics*, 1992, **71**, R1-R22.
74. Lehmann, V., Gosele, U.: Porous silicon formation - a quantum wire effect. *Applied Physics Letters*, 1991, **58**, 856-858.
75. Zhang, X. G., Collins, S. D., Smith, R. L.: Porous silicon formation and electropolishing of silicon by anodic polarization in hf solution. *Journal of the Electrochemical Society*, 1989, **136**, 1561-1565.
76. Takai, H., Itoh, T.: Porous silicon layers and its oxide for the silicon-on-insulator structure. *Journal of Applied Physics*, 1986, **60**, 222-225.
77. Theiß, W., Henkel, S., Arntzen, M.: Connecting microscopic and macroscopic properties of porous media: Choosing appropriate effective medium concepts. *Thin Solid Films*, 1995, **255**, 177-180.

78. Pap, A. E., Kordas, K., Vahakangas, J., Uusimaki, A., Leppavuori, S., Pilon, L., Szatmari, S.: Optical properties of porous silicon. Part III: Comparison of experimental and theoretical results. *Optical Materials*, 2006, **28**, 506-513.
79. Khardani, M., Bouařha, M., Bessa ř, B.: Bruggeman effective medium approach for modelling optical properties of porous silicon: Comparison with experiment. *physica status solidi (c)*, 2007, **4**, 1986-1990.
80. De Stefano, L., Rotiroti, L., Rendina, I., Moretti, L., Scognamiglio, V., Rossi, M., D'Auria, S.: Porous silicon-based optical microsensor for the detection of L-glutamine. *Biosensors & Bioelectronics*, 2006, **21**, 1664-1667.
81. Cunin, F., Schmedake, T. A., Link, J. R., Li, Y. Y., Koh, J., Bhatia, S. N., Sailor, M. J.: Biomolecular screening with encoded porous-silicon photonic crystals. *Nature Materials*, 2002, **1**, 39-41.
82. Cullis, A. G., Canham, L. T., Calcott, P. D. J.: The structural and luminescence properties of porous silicon. *Journal of Applied Physics*, 1997, **82**, 909-965.
83. Pacholski, C.: Photonic crystal sensors based on porous silicon. *Sensors*, 2013, **13**, 4694-4713.
84. Starodub, N. F., Fedorenko, L. L., Starodub, V. M., Dikij, S. P., Svechnikov, S. V.: Use of the silicon crystals photoluminescence to control immunocomplex formation. *Sensors and Actuators B-Chemical*, 1996, **35**, 44-47.
85. Di Francia, G., La Ferrara, V., Manzo, S., Chiavarini, S.: Towards a label-free optical porous silicon DNA sensor. *Biosensors & Bioelectronics*, 2005, **21**, 661-665.
86. Chan, S., Li, Y., Rothberg, L. J., Miller, B. L., Fauchet, P. M.: Nanoscale silicon microcavities for biosensing. *Materials Science & Engineering C-Biomimetic and Supramolecular Systems*, 2001, **15**, 277-282.
87. Chaudhari, P. S., Gokarna, A., Kulkarni, M., Karve, M. S., Bhoraskar, S.: Porous silicon as an entrapping matrix for the immobilization of urease. *Sensors and Actuators B-Chemical*, 2005, **107**, 258-263.
88. Sailor, M. J., Wu, E. C.: Photoluminescence-based sensing with porous silicon films, microparticles, and nanoparticles. *Advanced Functional Materials*, 2009, **19**, 3195-3208.
89. Pacholski, C., Sartor, M., Sailor, M. J., Cunin, F., Miskelly, G. M.: Biosensing using porous silicon double-layer interferometers: Reflective interferometric fourier transform spectroscopy. *Journal of the American Chemical Society*, 2005, **127**, 11636-11645.

90. Snow, P. A., Squire, E. K., Russell, P. S. J., Canham, L. T.: Vapor sensing using the optical properties of porous silicon bragg mirrors. *Journal of Applied Physics*, 1999, **86**, 1781-1784.
91. Jalkanen, T., Torres-Costa, V., Salonen, J., Bjorkqvist, M., Makila, E., Martinez-Duart, J. M., Lehto, V. P.: Optical gas sensing properties of thermally hydrocarbonized porous silicon bragg reflectors. *Optics Express*, 2009, **17**, 5446-5456.
92. Ilyas, S., Bocking, T., Kilian, K., Reece, P. J., Gooding, J., Gaus, K., Gal, M.: Porous silicon based narrow line-width rugate filters. *Optical Materials*, 2007, **29**, 619-622.
93. Salem, M. S., Sailor, M. J., Fukami, K., Sakka, T., Ogata, Y. H.: Sensitivity of porous silicon rugate filters for chemical vapor detection. *Journal of Applied Physics*, 2008, **103**, 083516.
94. Ouyang, H., Christophersen, M., Viard, R., Miller, B. L., Fauchet, P. M.: Macroporous silicon microcavities for macromolecule detection. *Advanced Functional Materials*, 2005, **15**, 1851-1859.
95. Jenie, S. N. A., Pace, S., Sciacca, B., Brooks, R. D., Plush, S. E., Voelcker, N. H.: Lanthanide luminescence enhancements in porous silicon resonant microcavities. *ACS Applied Materials & Interfaces*, 2014, **6**, 12012-12021.
96. Jiao, Y., Weiss, S. M.: Design parameters and sensitivity analysis of polymer-cladded porous silicon waveguides for small molecule detection. *Biosensors & Bioelectronics*, 2010, **25**, 1535-1538.
97. Rong, G., Najmaie, A., Sipe, J. E., Weiss, S. M.: Nanoscale porous silicon waveguide for label-free DNA sensing. *Biosensors & Bioelectronics*, 2008, **23**, 1572-1576.
98. White, I. M., Fan, X. D.: On the performance quantification of resonant refractive index sensors. *Optics Express*, 2008, **16**, 1020-1028.
99. Sirbuly, D. J., Tao, A., Law, M., Fan, R., Yang, P. D.: Multifunctional nanowire evanescent wave optical sensors. *Advanced Materials*, 2007, **19**, 61-66.
100. Dancil, K.-P. S., Greiner, D. P., Sailor, M. J.: A porous silicon optical biosensor: Detection of reversible binding of Igg to a protein A-modified surface. *Journal of the American Chemical Society*, 1999, **121**, 7925-7930.
101. Shtenberg, G., Massad-Ivanir, N., Engin, S., Sharon, M., Fruk, L., Segal, E.: DNA-directed immobilization of horseradish peroxidase onto porous SiO₂ optical transducers. *Nanoscale Research Letters*, 2012, **7**, 443.

102. Massad-Ivanir, N., Shtenberg, G., Zeidman, T., Segal, E.: Construction and characterization of porous SiO₂/hydrogel hybrids as optical biosensors for rapid detection of bacteria. *Advanced Functional Materials*, 2010, **20**, 2269-2277.
103. Massad-Ivanir, N., Shtenberg, G., Tzur, A., Krepker, M. A., Segal, E.: Engineering nanostructured porous SiO₂ surfaces for bacteria detection via "direct cell capture". *Analytical Chemistry*, 2011, **83**, 3282-3289.
104. Massad-Ivanir, N., Shtenberg, G., Raz, N., Gazenbeek, C., Budding, D., Bos, M. P., Segal, E.: Porous silicon-based biosensors: Towards real-time optical detection of target bacteria in the food industry. *Scientific Reports*, 2016, **6**, 38099.
105. Gaur, G., Koktysh, D. S., Weiss, S. M.: Immobilization of quantum dots in nanostructured porous silicon films: Characterizations and signal amplification for dual-mode optical biosensing. *Advanced Functional Materials*, 2013, **23**, 3604-3614.
106. Zhao, Y., Rodriguez, G. A., Graham, Y. M., Cao, T., Gaur, G., Weiss, S. M. Resonant photonic structures in porous silicon for biosensing. *Proc SPIE, Frontiers in Biological Detection: From Nanosensors to Systems IX*, 2017, **10081**, 100810D-1.
107. Wei, X., Kang, C., Liscidini, M., Rong, G., Retterer, S. T., Patrini, M., Sipe, J. E., Weiss, S. M.: Grating couplers on porous silicon planar waveguides for sensing applications. *Journal of Applied Physics*, 2008, **104**, 123113.
108. Wei, X., Weiss, S. M.: Guided mode biosensor based on grating coupled porous silicon waveguide. *Optics Express*, 2011, **19**, 11330-11339.
109. Rong, G., Ryckman, J. D., Mernaugh, R. L., Weiss, S. M.: Label-free porous silicon membrane waveguide for DNA sensing. *Applied Physics Letters*, 2008, **93**, 161109.
110. Saarrinen, J. J., Weiss, S. M., Fauchet, P. M., Sipe, J. E.: Optical sensor based on resonant porous silicon structures. *Optics Express*, 2005, **13**, 3754-3764.
111. Hiraoui, M., Haji, L., Guendouz, M., Lorrain, N., Moadhen, A., Oueslati, M.: Towards a biosensor based on anti resonant reflecting optical waveguide fabricated from porous silicon. *Biosensors & Bioelectronics*, 2012, **36**, 212-216.
112. Lawrie, J. L., Yang, J., Weiss, S. M.: Size-dependent infiltration and optical detection of nucleic acids in nanoscale pores. *IEEE Transactions on Nanotechnology*, 2010, **9**, 596-602.
113. Ouyang, H., Striemer, C. C., Fauchet, P. M.: Quantitative analysis of the sensitivity of porous silicon optical biosensors. *Applied Physics Letters*, 2006, **88**, 163108.

114. Anglin, E. J., Cheng, L. Y., Freeman, W. R., Sailor, M. J.: Porous silicon in drug delivery devices and materials. *Advanced Drug Delivery Reviews*, 2008, **60**, 1266-1277.
115. Steinem, C., Janshoff, A., Lin, V. S. Y., Völcker, N. H., Reza Ghadiri, M.: DNA hybridization-enhanced porous silicon corrosion: Mechanistic investigations and prospect for optical interferometric biosensing. *Tetrahedron*, 2004, **60**, 11259-11267.
116. Riikonen, J., Salomäki, M., van Wonderen, J., Kemell, M., Xu, W., Korhonen, O., Ritala, M., MacMillan, F., Salonen, J., Lehto, V.-P.: Surface chemistry, reactivity, and pore structure of porous silicon oxidized by various methods. *Langmuir*, 2012, **28**, 10573-10583.
117. Caras, C. A., Reynard, J. M., Bright, F. V.: An in-depth study linking the infrared spectroscopy and photoluminescence of porous silicon during ambient hydrogen peroxide oxidation. *Applied Spectroscopy*, 2013, **67**, 570-577.
118. Sailor, M. J. In Porous silicon in practice; Wiley-VCH Verlag GmbH & Co. KGaA: 2011, p 189-227.
119. Kolasinski, K. W.: Silicon nanostructures from electroless electrochemical etching. *Current Opinion in Solid State and Materials Science*, 2005, **9**, 73-83.
120. Kilian, K. A., Böcking, T., Gooding, J. J.: The importance of surface chemistry in mesoporous materials: Lessons from porous silicon biosensors. *Chemical Communications*, 2009, **6**, 630-640.
121. Böcking, T., Kilian, K. A., Gaus, K., Gooding, J. J.: Modifying porous silicon with self-assembled monolayers for biomedical applications: The influence of surface coverage on stability and biomolecule coupling. *Advanced Functional Materials*, 2008, **18**, 3827-3833.
122. Zhao, Y. L., Lawrie, J. L., Beavers, K. R., Laibinis, P. E., Weiss, S. M.: Effect of DNA-induced corrosion on passivated porous silicon biosensors. *ACS Applied Materials & Interfaces*, 2014, **6**, 13510-13519.
123. Canham, L. T., Reeves, C. L., Newey, J. P., Houlton, M. R., Cox, T. I., Buriak, J. M., Stewart, M. P.: Derivatized mesoporous silicon with dramatically improved stability in simulated human blood plasma. *Advanced Materials*, 1999, **11**, 1505-1507.
124. Linford, M. R., Chidsey, C. E. D.: Alkyl monolayers covalently bonded to silicon surfaces. *Journal of the American Chemical Society*, 1993, **115**, 12631-12632.
125. Linford, M. R., Fenter, P., Eisenberger, P. M., Chidsey, C. E. D.: Alkyl monolayers on silicon prepared from 1-alkenes and hydrogen-terminated silicon. *Journal of the American Chemical Society*, 1995, **117**, 3145-3155.

126. Buriak, J. M., Allen, M. J.: Lewis acid mediated functionalization of porous silicon with substituted alkenes and alkynes. *Journal of the American Chemical Society*, 1998, **120**, 1339-1340.
127. Boukherroub, R., Petit, A., Loupy, A., Chazalviel, J. N., Ozanam, F.: Microwave-assisted chemical functionalization of hydrogen-terminated porous silicon surfaces. *Journal of Physical Chemistry B*, 2003, **107**, 13459-13462.
128. Wu, E. C., Andrew, J. S., Buyanin, A., Kinsella, J. M., Sailor, M. J.: Suitability of porous silicon microparticles for the long-term delivery of redox-active therapeutics. *Chemical Communications*, 2011, **47**, 5699.
129. Salonen, J., Laine, E., Niinisto, L.: Thermal carbonization of porous silicon surface by acetylene. *Journal of Applied Physics*, 2002, **91**, 456-461.
130. Salonen, J., Bjorkqvist, M., Laine, E., Niinisto, L.: Stabilization of porous silicon surface by thermal decomposition of acetylene. *Applied Surface Science*, 2004, **225**, 389-394.
131. Bjorkqvist, M., Paski, J., Salonen, J., Lehto, V. P.: Temperature dependence of thermally-carbonized porous silicon humidity sensor. *Physica Status Solidi a-Applications and Materials Science*, 2005, **202**, 1653-1657.
132. Ruminski, A. M., King, B. H., Salonen, J., Snyder, J. L., Sailor, M. J.: Porous silicon-based optical microsensors for volatile organic analytes: Effect of surface chemistry on stability and specificity. *Advanced Functional Materials*, 2010, **20**, 2874-2883.
133. Tsang, C. K., Kelly, T. L., Sailor, M. J., Li, Y. Y.: Highly stable porous silicon-carbon composites as label-free optical biosensors. *ACS Nano*, 2012, **6**, 10546-10554.
134. Kelly, T. L., Gao, T., Sailor, M. J.: Carbon and carbon/silicon composites templated in rugate filters for the adsorption and detection of organic vapors. *Advanced Materials*, 2011, **23**, 1776-1781.
135. De Stefano, L., Rea, I., Rendina, I., Rotiroti, L., Rossi, M., D'Auria, S.: Resonant cavity enhanced optical microsensor for molecular interactions based on porous silicon. *Physica Status Solidi a-Applications and Materials Science*, 2006, **203**, 886-891.
136. Rodriguez, G. A., Ryckman, J. D., Jiao, Y., Weiss, S. M.: A size selective porous silicon grating-coupled bloch surface and sub-surface wave biosensor. *Biosensors & Bioelectronics*, 2014, **53**, 486-493.
137. Bonanno, L. M., DeLouise, L. A.: Steric crowding effects on target detection in an affinity biosensor. *Langmuir*, 2007, **23**, 5817-5823.

138. Orosco, M. M., Pacholski, C., Sailor, M. J.: Real-time monitoring of enzyme activity in a mesoporous silicon double layer. *Nature Nanotechnology*, 2009, **4**, 255-258.
139. De Stefano, L., Malecki, K., Rossi, A. M., Rotiroti, L., Corte, F. G. D., Moretti, L., Rendina, I.: Integrated silicon-glass opto-chemical sensors for lab-on-chip applications. *Sensors and Actuators B: Chemical*, 2006, **114**, 625-630.
140. Rea, I., Orabona, E., Lamberti, A., Rendina, I., De Stefano, L.: A microfluidics assisted porous silicon array for optical label-free biochemical sensing. *Biomicrofluidics*, 2011, **5**, 034120.
141. Wei, X., Mares, J. W., Gao, Y. D., Li, D., Weiss, S. M.: Biomolecule kinetics measurements in flow cell integrated porous silicon waveguides. *Biomedical Optics Express*, 2012, **3**, 1993-2003.
142. De Stefano, L., Orabona, E., Lamberti, A., Rea, I., Rendina, I.: Microfluidics assisted biosensors for label-free optical monitoring of molecular interactions. *Sensors and Actuators B: Chemical*, 2013, **179**, 157-162.
143. de la Escosura-Muniz, A., Merkoci, A.: Nanochannels preparation and application in biosensing. *ACS Nano*, 2012, **6**, 7556-7583.
144. Lazzara, T. D., Mey, I., Steinem, C., Janshoff, A.: Benefits and limitations of porous substrates as biosensors for protein adsorption. *Analytical Chemistry*, 2011, **83**, 5624-5630.
145. Kant, K., Yu, J. X., Priest, C., Shapter, J. G., Losic, D.: Impedance nanopore biosensor: Influence of pore dimensions on biosensing performance. *Analyst*, 2014, **139**, 1134-1140.
146. Schuck, P., Millar, D. B., Kortt, A. A.: Determination of binding constants by equilibrium titration with circulating sample in a surface plasmon resonance biosensor. *Analytical Biochemistry*, 1998, **265**, 79-91.
147. Abrantes, M., Magone, M. T., Boyd, L. F., Schuck, P.: Adaptation of a surface plasmon resonance biosensor with microfluidics for use with small sample volumes and long contact times. *Analytical Chemistry*, 2001, **73**, 2828-2835.
148. Vilensky, R., Bercovici, M., Segal, E.: Oxidized porous silicon nanostructures enabling electrokinetic transport for enhanced DNA detection. *Advanced Functional Materials*, 2015, **25**, 6725-6732.
149. Zhao, Y. L., Gaur, G., Retterer, S. T., Laibinis, P. E., Weiss, S. M.: Flow-through porous silicon membranes for real-time label-free biosensing. *Analytical Chemistry*, 2016, **88**, 10940-10948.

150. Zhao, Y., Gaur, G., Mernaugh, R. L., Laibinis, P. E., Weiss, S. M.: Comparative kinetic analysis of closed-ended and open-ended porous sensors. *Nanoscale Research Letters*, 2016, **11**, 395.
151. Sinton, D., Gordon, R., Brolo, A. G.: Nanohole arrays in metal films as optofluidic elements: Progress and potential. *Microfluidics and Nanofluidics*, 2008, **4**, 107-116.
152. Eftekhari, F., Escobedo, C., Ferreira, J., Duan, X. B., Girotto, E. M., Brolo, A. G., Gordon, R., Sinton, D.: Nanoholes as nanochannels: Flow-through plasmonic sensing. *Analytical Chemistry*, 2009, **81**, 4308-4311.
153. Huang, M., Galarreta, B. C., Cetin, A. E., Altug, H.: Actively transporting virus like analytes with optofluidics for rapid and ultrasensitive biodetection. *Lab on A Chip*, 2013, **13**, 4841-4847.
154. Escobedo, C.: On-chip nanohole array based sensing: A review. *Lab on A Chip*, 2013, **13**, 2445-2463.
155. Masson, J. F., Murray-Methot, M. P., Live, L. S.: Nanohole arrays in chemical analysis: Manufacturing methods and applications. *Analyst*, 2010, **135**, 1483-1489.
156. Najiminaini, M., Vasefi, F., Kaminska, B., Carson, J. J. L.: Optical resonance transmission properties of nano-hole arrays in a gold film: Effect of adhesion layer. *Optics Express*, 2011, **19**, 26186-26197.
157. Kee, J. S., Lim, S. Y., Perera, A. P., Zhang, Y., Park, M. K.: Plasmonic nanohole arrays for monitoring growth of bacteria and antibiotic susceptibility test. *Sensors and Actuators B-Chemical*, 2013, **182**, 576-583.
158. Gowda, S. R., Pushparaj, V., Herle, S., Girishkumar, G., Gordon, J. G., Gullapalli, H., Zhan, X., Ajayan, P. M., Reddy, A. L. M.: Three-dimensionally engineered porous silicon electrodes for Li ion batteries. *Nano Letters*, 2012, **12**, 6060-6065.
159. Oakes, L., Westover, A., Mares, J. W., Chatterjee, S., Erwin, W. R., Bardhan, R., Weiss, S. M., Pint, C. L.: Surface engineered porous silicon for stable, high performance electrochemical supercapacitors. *Scientific Reports*, 2013, **3**, 3020.
160. Lawrie, J. L., Xu, Z., Rong, G., Laibinis, P. E., Weiss, S. M.: Synthesis of DNA oligonucleotides in mesoporous silicon. *physica status solidi (a)*, 2009, **206**, 1339-1342.
161. Beavers, K. R., Mares, J. W., Swartz, C. M., Zhao, Y. L., Weiss, S. M., Duvall, C. L.: In situ synthesis of peptide nucleic acids in porous silicon for drug delivery and biosensing. *Bioconjugate Chemistry*, 2014, **25**, 1192-1197.

162. Lawrie, J. L., Weiss, S. M.: Stabilization of hydroxyl-terminated silanes in porous silicon for in-situ DNA synthesis. *physica status solidi (c)*, 2011, **8**, 1851-1855.
163. Yeh, P.: Optical waves in layered media; Wiley: New York, 1988.
164. Lugo, J. E., Lopez, H. A., Chan, S., Fauchet, P. M.: Porous silicon multilayer structures: A photonic band gap analysis. *Journal of Applied Physics*, 2002, **91**, 4966-4972.
165. Rodriguez, G. A., Lawrie, J. L., Weiss, S. M. In Porous silicon for biomedical applications; 1st ed.; Santos H A, Ed.; Woodhead Publishing Ltd.: Sawston, Cambridge, 2014, p 324-326.
166. Zhao, Y., Lawrie, J. L., Laibinis, P. E., Weiss, S. M. Understanding and mitigating DNA induced corrosion in porous silicon based biosensors. *Proceedings of SPIE*, 2014, **8933**, 893302-893309.
167. Voelcker, N. H., Alfonso, I., Ghadiri, M. R.: Catalyzed oxidative corrosion of porous silicon used as an optical transducer for ligand-receptor interactions. *ChemBioChem*, 2008, **9**, 1776-1786.
168. Nielsen, P. E., Egholm, M.: An introduction to peptide nucleic acid. *Current Issues In Molecular Biology*, 1999, **1**, 89-104.
169. Ratilainen, T., Holm n, A., Nord n, B.: Thermodynamics of PNA interactions 2nd ed.; Horizon Bioscience: Wymondham, U.K., 2004.
170. Menchise, V., De Simone, G., Tedeschi, T., Corradini, R., Sforza, S., Marchelli, R., Capasso, D., Saviano, M., Pedone, C. Insights into peptide nucleic acid (PNA) structural features: The crystal structure of a d-lysine-based chiral PNA-DNA duplex. *Proceedings of the National Academy of Sciences of the United States of America*, 2003, **100**, 12021-12026.
171. Rasmussen, H., Sandholm, J.: Crystal structure of a peptide nucleic acid (PNA) duplex at 1.7 angstrom resolution. *Nature Structural Biology*, 1997, **4**, 98-101.
172. Todd, B. A., Rau, D. C.: Interplay of ion binding and attraction in DNA condensed by multivalent cations. *Nucleic Acids Research*, 2007, **36**, 501-510.
173. Keyser, U. F., Koeleman, B. N., van Dorp, S., Krapf, D., Smeets, R. M. M., Lemay, S. G., Dekker, N. H., Dekker, C.: Direct force measurements on DNA in a solid-state nanopore. *Nature Physics*, 2006, **2**, 473-477.
174. Jorgensen, P. J.: Effect of an electric field on silicon oxidation. *The Journal of Chemical Physics*, 1962, **37**, 874-877.

175. Lauw, Y., Horne, M. D., Rodopoulos, T., Nelson, A., Leermakers, F. A. M.: Electrical double-layer capacitance in room temperature ionic liquids: Ion-size and specific adsorption effects. *Journal of Physical Chemistry B*, 2010, **114**, 11149-11154.
176. Liu, H., Steigerwald, M. L., Nuckolls, C.: Electrical double layer catalyzed wet-etching of silicon dioxide. *Journal of the American Chemical Society*, 2009, **131**, 17034-17035.
177. Zhang, X. G., In *Electrochemistry of Silicon and Its Oxide*; Kluwer Academic/Plenum Publishers: New York, 2001; Chapter 5, pp 199.
178. Bruce, P. G., Scrosati, B., Tarascon, J. M.: Nanomaterials for rechargeable lithium batteries. *Angewandte Chemie-International Edition*, 2008, **47**, 2930-2946.
179. Mehta, V., Cooper, J. S.: Review and analysis of PEM fuel cell design and manufacturing. *Journal of Power Sources*, 2003, **114**, 32-53.
180. Vallet-Regi, M., Balas, F., Arcos, D.: Mesoporous materials for drug delivery. *Angewandte Chemie-International Edition*, 2007, **46**, 7548-7558.
181. Anglin, E. J., Cheng, L. Y., Freeman, W. R., Sailor, M. J.: Porous silicon in drug delivery devices and materials. *Advanced Drug Delivery Reviews*, 2008, **60**, 1266-1277.
182. Myers, F. B., Lee, L. P.: Innovations in optical microfluidic technologies for point-of-care diagnostics. *Lab on A Chip*, 2008, **8**, 2015-2031.
183. Ahmed, M. U., Saaem, I., Wu, P. C., Brown, A. S.: Personalized diagnostics and biosensors: A review of the biology and technology needed for personalized medicine. *Critical Reviews in Biotechnology*, 2014, **34**, 180-196.
184. Cindrella, L., Kannan, A. M., Lin, J. F., Saminathan, K., Ho, Y., Lin, C. W., Wertz, J.: Gas diffusion layer for proton exchange membrane fuel cells-a review. *Journal of Power Sources*, 2009, **194**, 146-160.
185. Peighambardoust, S. J., Rowshanzamir, S., Amjadi, M.: Review of the proton exchange membranes for fuel cell applications. *International Journal of Hydrogen Energy*, 2010, **35**, 9349-9384.
186. Sun, H., Liu, H. T., Guo, L. J.: PEM fuel cell performance and its two-phase mass transport. *Journal of Power Sources*, 2005, **143**, 125-135.
187. Chen, L., Luan, H. B., He, Y. L., Tao, W. Q.: Pore-scale flow and mass transport in gas diffusion layer of proton exchange membrane fuel cell with interdigitated flow fields. *International Journal of Thermal Sciences*, 2012, **51**, 132-144.

188. Sant, S., Nadeau, W., Hildgen, P.: Effect of porosity on the release kinetics of propafenone-loaded PEG-g-PLA nanoparticles. *Journal of Controlled Release*, 2005, **107**, 203-214.
189. Arruebo, M.: Drug delivery from structured porous inorganic materials. *Wiley Interdisciplinary Reviews: Nanomedicine and Nanobiotechnology*, 2012, **4**, 16-30.
190. Kumeria, T., Losic, D.: Controlling interferometric properties of nanoporous anodic aluminium oxide. *Nanoscale Research Letters*, 2012, **7**, 1.
191. Ali, M. A., Srivastava, S., Solanki, P. R., Agrawal, V. V., John, R., Malhotra, B. D.: Nanostructured anatase-titanium dioxide based platform for application to microfluidics cholesterol biosensor. *Applied Physics Letters*, 2012, **101**, 084105.
192. de Jong, J., Lammertink, R. G. H., Wessling, M.: Membranes and microfluidics: A review. *Lab on a Chip*, 2006, **6**, 1125-1139.
193. Kumar, N., Froner, E., Guider, R., Scarpa, M., Bettotti, P.: Investigation of non-specific signals in nanoporous flow-through and flow-over based sensors. *Analyst*, 2014, **139**, 1345-1349.
194. Escobedo, C., Brolo, A. G., Gordon, R., Sinton, D.: Flow-through vs flow-over: Analysis of transport and binding in nanohole array plasmonic biosensors. *Analytical Chemistry*, 2010, **82**, 10015-10020.
195. Squires, T. M., Messinger, R. J., Manalis, S. R.: Making it stick: Convection, reaction and diffusion in surface-based biosensors. *Nature Biotechnology*, 2008, **26**, 417-426.
196. Zhang, W., Stone, H. A., Sherwood, J. D.: Mass transfer at a microelectrode in channel flow. *Journal of Physical Chemistry*, 1996, **100**, 9462-9464.
197. Meechai, N., Jamieson, A. M., Blackwell, J.: Translational diffusion coefficients of bovine serum albumin in aqueous solution at high ionic strength. *Journal of Colloid and Interface Science*, 1999, **218**, 167-175.
198. Horton, M. R., Hofling, F., Radler, J. O., Franosch, T.: Development of anomalous diffusion among crowding proteins. *Soft Matter*, 2010, **6**, 2648-2656.
199. Sato, H., Yui, M., Yoshikawa, H.: Ionic diffusion coefficient of Cs⁺, Pb²⁺, Sm³⁺, Ni²⁺, SeO₄²⁻ and TcO₄⁴⁻ in free water determined from conductivity measurements. *Journal of Nuclear Science and Technology*, 1996, **33**, 950-955.
200. Mu, D., Liu, Z. S., Huang, C., Djilali, N.: Determination of the effective diffusion coefficient in porous media including knudsen effects. *Microfluidics and Nanofluidics*, 2008, **4**, 257-260.

201. Mares, J. W., Weiss, S. M.: Diffusion dynamics of small molecules from mesoporous silicon films by real-time optical interferometry. *Applied Optics*, 2011, **50**, 5329-5337.
202. Gao, Y., Wolf, L. K., Georgiadis, R. M.: Secondary structure effects on DNA hybridization kinetics: A solution versus surface comparison. *Nucleic Acids Research*, 2006, **34**, 3370-3377.
203. Grigoras, K., Franssila, S., Sikanen, T., Kotiaho, T., Kostianen, R.: Fabrication of porous membrane filter from p-type silicon. *Physica Status Solidi a-Applications and Materials Science*, 2005, **202**, 1624-1628.
204. Cruz, S., Honig-dOrville, A., Muller, J.: Fabrication and optimization of porous silicon substrates for diffusion membrane applications. *Journal of the Electrochemical Society*, 2005, **152**, C418-C424.
205. Gold, S., Chu, K. L., Lu, C., Shannon, M. A., Masel, R. I.: Acid loaded porous silicon as a proton exchange membrane for micro-fuel cells. *Journal of Power Sources*, 2004, **135**, 198-203.
206. Pichonat, T., Gauthier-Manuel, B.: Realization of porous silicon based miniature fuel cells. *Journal of Power Sources*, 2006, **154**, 198-201.
207. Mark, D., Haerberle, S., Roth, G., von Stetten, F., Zengerle, R.: Microfluidic lab-on-a-chip platforms: Requirements, characteristics and applications. *Chemical Society Reviews*, 2010, **39**, 1153-1182.
208. Gaur, G., Koktysh, D. S., Fleetwood, D. M., Weller, R. A., Reed, R. A., Weiss, S. M.: Influence of interfacial oxide on the optical properties of single layer CdTe/CdS quantum dots in porous silicon scaffolds. *Applied Physics Letters*, 2015, **107**, 063106.
209. Torimoto, T., Adachi, T., Okazaki, K., Sakuraoka, M., Shibayama, T., Ohtani, B., Kudo, A., Kuwabata, S.: Facile synthesis of ZnS-AgInS₂ solid solution nanoparticles for a color-adjustable luminophore. *Journal of the American Chemical Society*, 2007, **129**, 12388-12389.
210. Torimoto, T., Ogawa, S., Adachi, T., Kameyama, T., Okazaki, K. I., Shibayama, T., Kudo, A., Kuwabata, S.: Remarkable photoluminescence enhancement of ZnS-AgInS₂ solid solution nanoparticles by post-synthesis treatment. *Chemical Communications*, 2010, **46**, 2082-2084.
211. Krismastuti, F. S. H., Pace, S., Voelcker, N. H.: Porous silicon resonant microcavity biosensor for matrix metalloproteinase detection. *Advanced Functional Materials*, 2014, **24**, 3639-3650.

212. Qiao, H., Guan, B., Bocking, T., Gal, M., Gooding, J. J., Reece, P. J.: Optical properties of II-VI colloidal quantum dot doped porous silicon microcavities. *Applied Physics Letters*, 2010, **96**, 161106.
213. Ning, H., Krueger, N. A., Sheng, X., Keurn, H., Zhang, C., Choquette, K. D., Li, X. L., Kim, S., Rogers, J. A., Braun, P. V.: Transfer-printing of tunable porous silicon microcavities with embedded emitters. *ACS Photonics*, 2014, **1**, 1144-1150.
214. Nicholl, R. J. T., Conley, H. J., Lavrik, N. V., Vlassiuk, I., Puzyrev, Y. S., Sreenivas, V. P., Pantelides, S. T., Bolotin, K. I.: The effect of intrinsic crumpling on the mechanics of free-standing graphene. *Nature Communications*, 2015, **6**, 8789.
215. Fernandes, T. G., Diogo, M. M., Clark, D. S., Dordick, J. S., Cabral, J. M.: High-throughput cellular microarray platforms: Applications in drug discovery, toxicology and stem cell research. *Trends Biotechnol.*, 2009, **27**, 342-349.
216. Ressine, A., Marko-Varga, G., Laurell, T.: Porous silicon protein microarray technology and ultra-/superhydrophobic states for improved bioanalytical readout. *Biotechnology Annual Review*, 2007, **13**, 149-200.
217. Yamaguchi, R., Miyamoto, K., Ishibashi, K., Hirano, A., Said, S. M., Kimura, Y., Niwano, M.: DNA hybridization detection by porous silicon-based DNA microarray in conjugation with infrared microspectroscopy. *Journal of Applied Physics*, 2007, **102**, 014303.
218. Rea, I., Lamberti, A., Rendina, I., Coppola, G., Gioffre, M., Iodice, M., Casalino, M., De Tommasi, E., De Stefano, L.: Fabrication and characterization of a porous silicon based microarray for label-free optical monitoring of biomolecular interactions. *Journal of Applied Physics*, 2010, **107**, 014513.